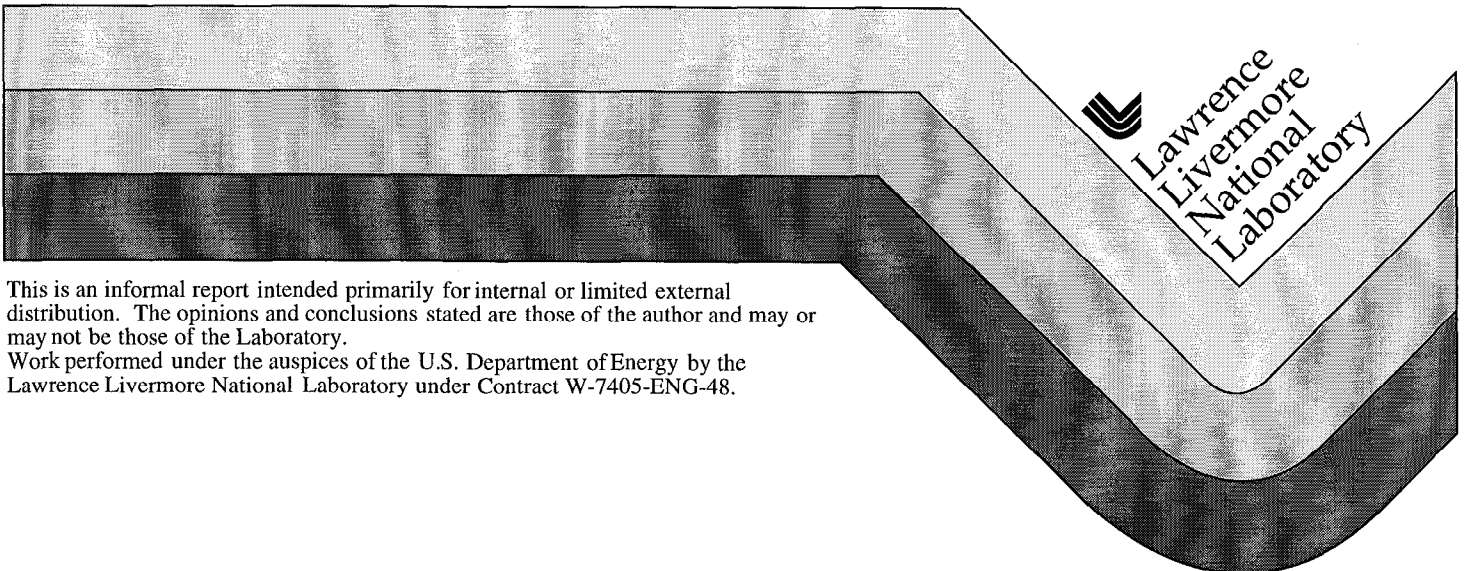


Aging and Phase Stability of Waste Package Outer Barrier

T. Summers
P. Turchi

July 1, 1999



DISCLAIMER

This document was prepared as an account of work sponsored by an agency of the United States Government. Neither the United States Government nor the University of California nor any of their employees, makes any warranty, express or implied, or assumes any legal liability or responsibility for the accuracy, completeness, or usefulness of any information, apparatus, product, or process disclosed, or represents that its use would not infringe privately owned rights. Reference herein to any specific commercial product, process, or service by trade name, trademark, manufacturer, or otherwise, does not necessarily constitute or imply its endorsement, recommendation, or favoring by the United States Government or the University of California. The views and opinions of authors expressed herein do not necessarily state or reflect those of the United States Government or the University of California, and shall not be used for advertising or product endorsement purposes.

This report has been reproduced
directly from the best available copy.

Available to DOE and DOE contractors from the
Office of Scientific and Technical Information
P.O. Box 62, Oak Ridge, TN 37831
Prices available from (423) 576-8401

Available to the public from the
National Technical Information Service
U.S. Department of Commerce
5285 Port Royal Rd.,
Springfield, VA 22161

CHECK COPY

Aging and Phase Stability of Waste Package Outer Barrier

ANL-EBS-MD-000002, Rev. 00A

by

Tammy Summers and Patrice Turchi

July 1999

**Lawrence Livermore National Laboratory
Livermore, California**

OFFICE OF CIVILIAN RADIOACTIVE WASTE MANAGEMENT
ANALYSIS/MODEL COVER SHEET

1. QA: Q

Page: 1 of 1

Complete Only Applicable Items

2. <input type="checkbox"/> Analysis <input type="checkbox"/> Engineering <input type="checkbox"/> Performance Assessment <input type="checkbox"/> Scientific	3. <input type="checkbox"/> Model <input type="checkbox"/> Conceptual Model Documentation <input type="checkbox"/> Model Documentation <input type="checkbox"/> Model Validation Documentation
---	--

4. Title:
Aging and Phase Stability of Waste Package Outer Barrier

5. Document Identifier (including Rev. No. and Change No., if applicable):
ANL-EBS-MD-000002, Rev. 00A

6. Total Attachments: 0	7. Attachment Numbers —No. of Pages in Each:
----------------------------	--

	Printed Name	Signature	Date
8. Originator Tammy Summers	TAMMY EDGEcombe SUMMERS	W. L. Clarke for Tammy Summers	7/14/99
9. Checker			
10. Lead/Supervisor	Willis CLARKE	W. L. Clarke	7/14/99
11. Responsible manager	DAVID STAHL		

12. Remarks

OFFICE OF CIVILIAN RADIOACTIVE WASTE MANAGEMENT
ANALYSIS/MODEL REVISION RECORD

1. Page: 1 of 1

Complete Only Applicable Items

2. Analysis or Model Title:

Aging and Phase Stability of Waste Package Outer Barrier

3. Document Identifier (including Rev. No. and Change No., if applicable):

ANL-EBS-MD-000002, Rev. 00A

4. Revision/Change No.

5. Description of Revision/Change

CONTENTS

	Page
ANALYSIS/MODEL COVER SHEET.....	i
ANALYSIS/MODEL REVISION RECORD	iii
FIGURES.....	viii
TABLES.....	xii
ABBREVIATIONS AND ACRONYMS	xiii
1. PURPOSE	1-1
2. QUALITY ASSURANCE.....	2-1
3. COMPUTER SOFTWARE AND MODEL USAGE.....	3-1
3.1 SOFTWARE REQUIRING APPROVAL FOR QA WORK.....	3-1
3.2 SOFTWARE ROUTINES	3-1
4. INPUTS	4-1
4.1 DATA AND PARAMETERS.....	4-1
4.1.1 Transmission Electron Microscopy Micrographs Used in Preliminary Intermetallic and Carbide Phase Identification.....	4-1
4.1.2 TEM Micrographs Used for Identification of Phases Forming in Alloy 22 as a Function of Aging Time and Temperature	4-38
4.1.3 X-Ray Diffraction Data Used for Quantification and Identification of Phases Forming in Alloy 22 as a Function of Aging Time and Temperature.....	4-38
4.1.4 Micrographs Showing Precipitation in Alloy 22 Beginning On and Covering Grain Boundaries, Beginning on Twin Boundaries, and Beginning Within the Grains	4-38
4.1.5 Fraction Intermetallic and Carbide Precipitation in Alloy 22 as a Function of Aging Time and Temperature.....	4-62
4.1.6 Micrographs Showing Intermetallic Particles in Alloy 22 Welds	4-62
4.1.7 Volume Fraction of Intermetallic and Carbide Precipitation in Alloy 22 Weld HAZ as a Function of Aging Time, Temperature, and Weld Type.....	4-74
4.1.8 Volume Fraction and Particle Size of Intermetallics and Carbides in Alloy 22 Welds as a Function of Aging Time, Temperature, and Weld Type.....	4-74

CONTENTS (continued)

	Page
4.1.9 TEM Micrographs Showing When LRO Has Been Observed	4-74
4.1.10 TEM Micrographs Used to Determine Volume Fraction of Ordered Domains Present in Alloy 22 as a Function of Aging Time, Temperature, and Starting Material (Base Metal or Weld))	4-86
4.2 CRITERIA	4-86
4.3 CODES AND STANDARDS	4-86
5. ASSUMPTIONS	5-1
5.1 RELEVANT WPOB MATERIAL TEMPERATURES LESS THAN 350°C	5-1
5.2 KINETICS SAME FOR THE INTERMETALLIC AND CARBIDE PHASES IN ALLOY 22	5-1
5.3 TRANSFORMATION MECHANISMS OPERATING AT THE HIGHER TEMPERATURES INVESTIGATED ALSO OPERATE AT THE LOWER EXPECTED REPOSITORY TEMPERATURES	5-1
5.4 MINOR CHEMISTRY CHANGES WITHIN ASTM SPECIFICATION B575 (HEAT-TO-HEAT VARIABILITY) DO NOT SIGNIFICANTLY AFFECT THE PHASE STABILITY OF ALLOY 22	5-2
6. ANALYSIS/MODEL	6-2
6.1 PHASE IDENTIFICATION IN ALLOY 22	6-2
6.2 KINETICS OF INTERMETALLIC PRECIPITATION IN ALLOY 22	6-2
6.3 EXTRAPOLATION OF EMPIRICAL INTERMETALLIC AND CARBIDE PRECIPITATION KINETICS DATA	6-5
6.4 EFFECT OF INTERMETALLIC AND CARBIDE PRECIPITATION ON MECHANICAL PROPERTIES OF ALLOY 22 BASE METAL	6-5
6.5 KINETICS OF INTERMETALLIC PRECIPITATION IN ALLOY 22 WELD HAZ	6-5
6.6 STABILITY OF INTERMETALLIC AND CARBIDE PRECIPITATES IN ALLOY 22 WELDS	6-6
6.7 KINETICS OF LRO REACTIONS IN ALLOY 22	6-6
6.8 THEORETICAL CALCULATION OF ALLOY PHASE DIAGRAM AT REPOSITORY-RELEVANT TEMPERATURES	6-6
6.9 THEORETICAL CALCULATION OF ALLOY 22 TTT DIAGRAM AND EXTRAPOLATION TO LOWER TEMPERATURES	6-7
6.10 KINETICS OF LRO REACTIONS IN ALLOY 22	6-7
6.11 SOLIDIFICATION PATH OF THE ALLOY 22	6-8

CHECK COPY

CONTENTS (continued)

	Page
7. CONCLUSIONS.....	7-1
8. REFERENCES.....	8-1
9. ATTACHMENTS	9-1

FIGURES

	Page
Figure 4-1. Grain Boundary Precipitation in Alloy 22 Aged for 16,000 hr at 593°C	4-2
Figure 4-2. Dark-Field Image Corresponding to Figure 4-1.....	4-3
Figure 4-3. SAD Pattern from the Grain Boundary Precipitate Shown in Figures 4-1 and 4-2.....	4-4
Figure 4-4. Grain Boundary Precipitation in Alloy 22 Aged for 16,000 hr at 593°C	4-5
Figure 4-5. SAD Pattern from the Grain Boundary Precipitate Labeled Carbide in Figure 4-4.....	4-6
Figure 4-6. Grain Boundary Precipitation in Alloy 22 Aged for 16,000 hr at 649°C	4-7
Figure 4-7. Dark-Field Image Corresponding to Figure 4-6.....	4-8
Figure 4-8. SAD Pattern from the Grain Boundary Precipitate Shown in Figures 4-6 and 4-7.....	4-9
Figure 4-9. Grain Boundary Precipitation in Alloy 22 Aged for 16,000 hr at 649°C	4-10
Figure 4-10. Dark-Field Image Corresponding to Figure 4-9.....	4-11
Figure 4-11. SAD Pattern from the Grain Boundary Precipitate Shown in Figures 4-9 and 4-10	4-12
Figure 4-12. Precipitation in Alloy 22 Aged for 16,000 hr at 704°C	4-13
Figure 4-13. Dark-Field Image Corresponding to Figure 4-12	4-14
Figure 4-14. SAD Pattern from the Precipitate Shown in Figures 4-12 and 4-13.....	4-15
Figure 4-15. Grain Boundary Precipitation in Alloy 22 Aged for 16,000 hr at 704°C	4-16
Figure 4-16. Dark-Field Image Corresponding to Figure 4-15	4-17
Figure 4-17. SAD Pattern from the Grain Boundary Carbide Shown in Figures 4-15 and 4-16.....	4-18
Figure 4-18. Dark-Field Image Corresponding to Figure 4-15	4-19
Figure 4-19. SAD Pattern from the Grain Boundary μ Phase Precipitates Shown in Figures 4-15 and 4-18.....	4-20
Figure 4-20. Grain Boundary Precipitation in Alloy 22 Aged for 16,000 hr at 704°C	4-21
Figure 4-21. SAD Pattern from the Grain Boundary Precipitate Labeled Carbide in Figure 4-20	4-22
Figure 4-22. Grain Boundary Precipitation in Alloy 22 Aged for 16,000 hr at 704°C	4-23
Figure 4-23. SAD Pattern from Sigma Phase in Figure 4-22	4-24
Figure 4-24. SAD Pattern from the Small, Dark Particles in Figure 4-22.....	4-25
Figure 4-25. Precipitate in Alloy 22 Aged for 16,000 hr at 760°C	4-26
Figure 4-26. Dark-Field Image Corresponding to Figure 4-25	4-27
Figure 4-27. SAD Pattern from the P Phase Precipitate Shown in Figures 4-25 and 4-26.....	4-28

FIGURES (continued)

	Page
Figure 4-28. Grain Boundary Precipitation in Alloy 22 Aged for 16,000 hr at 760°C	4-29
Figure 4-29. SAD Pattern from the Sigma Phase Precipitate Shown in Figure 4-28	4-30
Figure 4-30. SAD Pattern from the Sigma Phase Precipitate Shown in Figure 4-28	4-31
Figure 4-31. SAD Pattern from the Sigma Phase Precipitate Shown in Figure 4-28	4-32
Figure 4-32. Precipitation in Alloy 22 Aged for 16,000 hr at 760°C	4-33
Figure 4-33. SAD Pattern from the μ Phase Precipitate Shown in Figure 4-28	4-34
Figure 4-34. Grain Boundary Precipitation in Alloy 22 Aged for 16,000 hr at 760°C	4-35
Figure 4-35. SAD Pattern from the μ Phase Precipitate Shown in Figure 4-34	4-36
Figure 4-36. SAD Pattern from the μ Phase Precipitate in Figure 4-34	4-37
Figure 4-37. SEM Micrograph Showing Precipitation Just Beginning on Grain Boundaries After Aging Alloy 22 for 10 hr at 593°C	4-39
Figure 4-38. SEM Micrograph Showing Precipitation on Grain Boundaries After Aging Alloy 22 for 100 hr at 593°C	4-40
Figure 4-39. Optical Micrograph Showing No Precipitation on Grain Boundaries After Aging Alloy 22 for 1 hr at 649°C	4-41
Figure 4-40. SEM Micrograph Showing Little or No Precipitation on Grain Boundaries After Aging Alloy 22 for 1 hr at 649°C	4-42
Figure 4-41. SEM Micrograph Showing Precipitation on Grain Boundaries After Aging Alloy 22 for 10 hr at 649°C	4-43
Figure 4-42. SEM Micrograph Showing Precipitation on Grain Boundaries After Aging Alloy 22 for 100 hr at 649°C	4-44
Figure 4-43. SEM Micrograph Showing Precipitation on Grain Boundaries After Aging Alloy 22 for 1000 hr at 649°C	4-45
Figure 4-44. SEM Micrograph Showing Precipitation on Grain and on Twin Boundaries After Aging Alloy 22 for 1000 hr at 649°C	4-46
Figure 4-45. SEM Micrograph Showing Precipitation on Grain Boundaries and Within the Grains After Aging Alloy 22 for 16,000 hr at 649°C	4-47
Figure 4-46. SEM Micrograph Showing Precipitation that Occurs at a Limited Number of Sites on Grain Boundaries in Alloy 22 After Aging for 1 hr at 704°C	4-48
Figure 4-47. SEM Micrograph Showing Precipitation on Grain Boundaries After Aging Alloy 22 for 10 hr at 704°C	4-49
Figure 4-48. SEM Micrograph Showing Significant Grain Boundary Precipitation After Aging Alloy 22 for 100 hr at 704°C	4-50
Figure 4-49. SEM Micrograph Showing Precipitation Just Beginning on Twin Boundaries After Aging Alloy 22 for 100 us at 704°C	4-51

FIGURES (continued)

	Page
Figure 4-50. SEM Micrograph Showing Complete Grain Boundary Coverage by Precipitation and Precipitation on Twin Boundaries After Aging Alloy 22 for 1000 hr at 704°C	4-52
Figure 4-51. SEM Micrograph Showing Precipitation Beginning Within the Grains After Aging Alloy 22 for 1000 hr at 704°C.....	4-53
Figure 4-52. SEM Micrograph Showing that Grain Boundary Precipitation Has Begun After Aging Alloy 22 for 1 hr at 760°C	4-54
Figure 4-53. SEM Micrograph Showing that Grain Boundary Precipitation Has Begun After Aging Alloy 22 for 1 hr at 760°C	4-55
Figure 4-54. SEM Micrograph Showing Significant Grain Boundary Precipitation After Aging Alloy 22 for 10 hr at 760°C.....	4-56
Figure 4-55. SEM Micrograph Showing Significant Grain Boundary Precipitation and Precipitation on Twin Boundaries After Aging Alloy 22 for 119 hr at 760°C	4-57
Figure 4-56. SEM Micrograph Showing Precipitation on Grain Boundaries, on Twin Boundaries, and Within the Grains After Aging Alloy 22 for 119 hr at 760°C	4-58
Figure 4-57. SEM Micrograph Showing Significant Precipitation Within the Grains of Alloy 22 After Aging for 1000 hr at 760°C.....	4-59
Figure 4-58. SEM Micrograph Showing Grain Boundary Precipitation in Alloy 22 After Aging for 1 hr at 800°C.....	4-60
Figure 4-59. SEM Micrograph Showing Significant Grain Boundary Precipitation in Alloy 22 After Aging for 10 hr at 800°C.....	4-61
Figure 4-60. SEM Micrograph Showing Precipitation on Grain Boundaries, on Twin Boundaries, and Within the Grains After Aging Alloy 22 for 100 hr at 800°C	4-62
Figure 4-61. Low-Magnification Optical Micrograph of an Alloy 22 Multipass, Double-V Gas-Tungsten-Arc-Welding (GTAW) Weld with Matching Filler Metal.....	4-63
Figure 4-62. SEM Micrograph of the Alloy 22 Weld Shown in Figure 4-58 Showing the Dendritic Structure Typical of Welds.....	4-64
Figure 4-63. SEM Micrograph of the Alloy 22 Weld Shown in Figure 4-58 Showing the Dendritic Structure Typical of Welds.....	4-65
Figure 4-64. Low-Magnification Optical Micrograph of an Alloy 22 Weld Similar to that Shown in Figure 4-58, But Aged for 40,000 hr at 427°C	4-66
Figure 4-65. SEM Micrograph of the Alloy 22 Weld Shown in Figure 4-61 at the Junction of Two Weld Passes.....	4-67
Figure 4-66. SEM Micrograph of the Alloy 22 Weld Shown in Figure 4-61 Showing the Dendritic Structure Typical of Welds.....	4-68

FIGURES (continued)

	Page
Figure 4-67. Optical Micrograph at the Fusion Line of the Alloy 22 Weld Shown in Figure 4-61	4-69
Figure 4-68. One of Few Precipitates Seen in the Alloy 22 Weld of Figure 4-61 Aged for 40,000 hr at 427°C	4-70
Figure 4-69. SAD Pattern from the Precipitate Shown in Figure 4-65	4-71
Figure 4-70. SAD Pattern from the Precipitate Shown in Figure 4-65	4-72
Figure 4-71. TEM Micrograph Showing One of Few Precipitates Seen in the HAZ of the Aged Alloy 22 Weld of Figure 4-61	4-73
Figure 4-72. TEM Micrograph Showing LRO Domains in an Alloy 22 Base Metal Sample Aged for 16,000 hr at 593°C	4-74
Figure 4-73. Dark-Field Image Corresponding to Figure 4-69	4-75
Figure 4-74. SAD Pattern from the Area Shown in Figure 4-69	4-76
Figure 4-75. TEM Micrograph from the Base Metal of an Alloy 22 Weld Sample Aged for 40,000 hr at 427°C	4-77
Figure 4-76. Dark-Field Image Corresponding to Figure 4-72	4-78
Figure 4-77. SAD Pattern from the Area Shown in Figure 4-74	4-79
Figure 4-78. TEM Micrograph from the Weld Metal of an Alloy 22 Multipass, Double-V GTAW Weld with Matching Filler Metal Aged for 40,000 hr at 427°C	4-80
Figure 4-79. Dark-Field Image Corresponding to Figure 4-75	4-81
Figure 4-80. SAD Pattern from the Area Shown in Figure 4-75	4-82
Figure 4-81. TEM Micrograph from the HAZ of the Alloy 22 Multipass, Double-V GTAW Weld with Matching Filler Metal (Figure 4-75) Aged for 40,000 hr at 427°C	4-83
Figure 4-82. Dark-Field Image Corresponding to Figure 4-78	4-84
Figure 4-83. SAD Pattern from the Area Shown in Figure 4-78	4-85
Figure 6-1. Isothermal TTT Diagram for Alloy 2 (TBV)	6-3
Figure 6-2. Time to Reach Various Stages of Precipitation in Aged Alloy 22 Plotted on a Log Scale as a Function of Reciprocal Temperature	6-4

TABLES

	Page
Table 6-1. Phases Observed in Alloy 22 in TEM (TBV)	6-2
Table 6-2. Time for Intermetallic and Carbide Precipitation in Alloy 22 to Begin On and Cover Grain Boundaries, Begin on Twin Boundaries, and Begin Within the Grains as a Function of Temperature.....	6-2

ABBREVIATIONS AND ACRONYMS

DS	drip shield
fcc	face-centered cubic
GTAW	gas-tungsten-arc welding
HAZ	heat-affected zone
LMTO	linear muffin-tin orbital
LRO	long-range order
MGR	monitored geologic repository
QA	quality assurance
SAD	selected area diffraction
SCC	stress corrosion cracking
SEM	scanning electron microscopy
SNF	spent nuclear fuel
TBD	to be determined
TBV	to be verified
TEM	transmission electron microscopy
TTT	time-temperature-transformation
WP	waste package
WPOB	waste package outer barrier

1. PURPOSE

These analyses will provide information on the phase stability of Alloy 22 (UNS #N06022), a waste-package-outer-barrier (WPOB) material. These phase stability studies are divided into four general areas:

- Intermetallic and carbide precipitation in the base metal
- Intermetallic and carbide precipitation in welded samples
- Long-range order (LRO) reactions
- Theoretical calculations of the thermodynamics and kinetics of the preceding transformations

Intermetallic and carbide precipitates that form in Alloy 22 are generally rich in chromium (Cr) and/or molybdenum (Mo). Because these elements are responsible for the good corrosion resistance of Alloy 22, precipitation of intermetallics and carbides, especially at grain boundaries, can lead to an increased susceptibility to localized corrosion in the alloy. These phases are brittle and also tend to embrittle the alloy. They are known to form in Alloy 22 at temperatures greater than approximately 600°C. Whether they also form at the lower temperatures expected in the potential repository in times up to approximately 10,000 yr must be determined. The kinetics of this precipitation will be determined for both the base metal and the weld heat-affected zone (HAZ). In these analyses, it is assumed that the precipitation kinetics of the various intermetallics and carbides that form can be described by a single equation. A procedure is currently being developed for identifying and measuring the relative amounts of each phase that form after a given aging treatment. If the preceding assumption proves invalid, the analyses can be modified to account for the precipitation of more than one phase.

The intermetallic phases P, μ , and σ are present in the weld metal in the as-welded condition. It may be possible to eliminate these phases through heat treatment, but that may not be possible for the closure weld because the spent-nuclear-fuel cladding cannot be heated to more than 350°C. These analyses will determine if the precipitation that occurs during the welding process has a significant effect on weld properties. If the weld properties are found to be adequate, it will be determined whether aging of Alloy 22 welds causes the precipitates to change in such a way that the properties are affected.

LRO occurs in nickel (Ni)-Cr-Mo alloys such as Alloy 22 at temperatures less than approximately 600°C. This ordering has been linked to an increased susceptibility of Ni-Cr-Mo alloys to stress corrosion cracking (SCC) and hydrogen embrittlement. These analyses will provide information on the rate at which LRO will occur in Alloy 22 under repository conditions.

Determination of the kinetics of transformations through experimental techniques requires that the transformations being investigated be accelerated, at least in this case, in which service life is expected to be thousands of human lifetimes long. Phase transformations are typically accelerated through an increase in temperature. The rate of transformation is determined at the higher temperature and is extrapolated to the lower temperatures of interest. In performing this extrapolation, two assumptions must be made. First, it must be assumed that the phases forming

CHECK COPY

at the higher temperatures are stable, and therefore also form, at the lower temperatures. Second, it must be assumed that the transformation mechanism operating at the higher temperatures also operates at the lower temperatures. The theoretical analyses will be used to determine the stability of the phases that form in Alloy 22 at repository-relevant temperatures and will provide more accurate extrapolation of the kinetic data obtained at high temperatures to the lower temperatures of interest allowing for the investigation of other known possible transformation mechanisms.

2. QUALITY ASSURANCE

The quality assurance (QA) program applies to the development of this report. The data provided in this report will be used for evaluating the postclosure performance of the monitored-geologic-repository (MGR) waste package (WP) and engineered barrier segment. The QAP-2.3 (*Classification of Permanent Items*) evaluation entitled *Classification of the Preliminary MGDS Repository Design* (CRWMS M&O 1998, p. IV-11) has identified the WP as an MGR (formerly MGDS [Mined Geologic Disposal System]) item important to safety and waste isolation. The WP responsible manager has evaluated the technical-document-development activity in accordance with QAP-2.0, *Conduct of Activities*. The QAP-2.0 activity evaluation, *Commercial SNF WP Reference Designs* (CRWMS M&O 1998), has determined that the preparation and review of this technical document are subject to *Quality Assurance Requirements and Description* (DOE 1998) requirements. In accordance with AP-3.10Q, a work plan was developed, issued, and used in preparing this document (CRWMS M&O 1999a).

3. COMPUTER SOFTWARE AND MODEL USAGE

3.1 SOFTWARE REQUIRING APPROVAL FOR QA WORK

THERMOCALC, commercially available software, has been acquired and will be used to calculate phase diagrams and other thermodynamic properties of the phases that form in Alloy 22. DICTRA, also commercially available, has been acquired and will be used to calculate the rate at which the relevant phase transformations occur. Both of these programs will need to go through a qualification process.

3.2 SOFTWARE ROUTINES

KaleidaGraph v3.08d (Synergy Software), loaded on a PowerMac 8600/250 with Macintosh operating system 8.0, was used for graphing and curve fitting data.

4. INPUTS

4.1 DATA AND PARAMETERS

4.1.1 Transmission Electron Microscopy Micrographs Used in Preliminary Intermetallic and Carbide Phase Identification (to be verified [TBV-1255])

This section contains transmission electron microscopy (TEM) images and electron-selected area diffraction (SAD) patterns used to identify the phases that form in Alloy 22 base metal after aging in the temperature range of 600 to 760°C (Figures 4-1 through 4-33). Because of the structural similarity of the μ and P phases, some diffraction patterns could be indexed as either phase. For this reason, the phases forming in some cases are only tentatively identified. Several carbides form in Alloy 22, but they all have very similar structures. Although they are significantly different chemically, it is not possible to distinguish them in the work reported subsequently. They are therefore simply called carbide.



Figure 4-1. Grain Boundary Precipitation in Alloy 22 Aged for 16,000 hr at 593°C

This phase was identified as P phase. (TS369-003a, Image S0125, 3/9/99, SN #434 p.41)

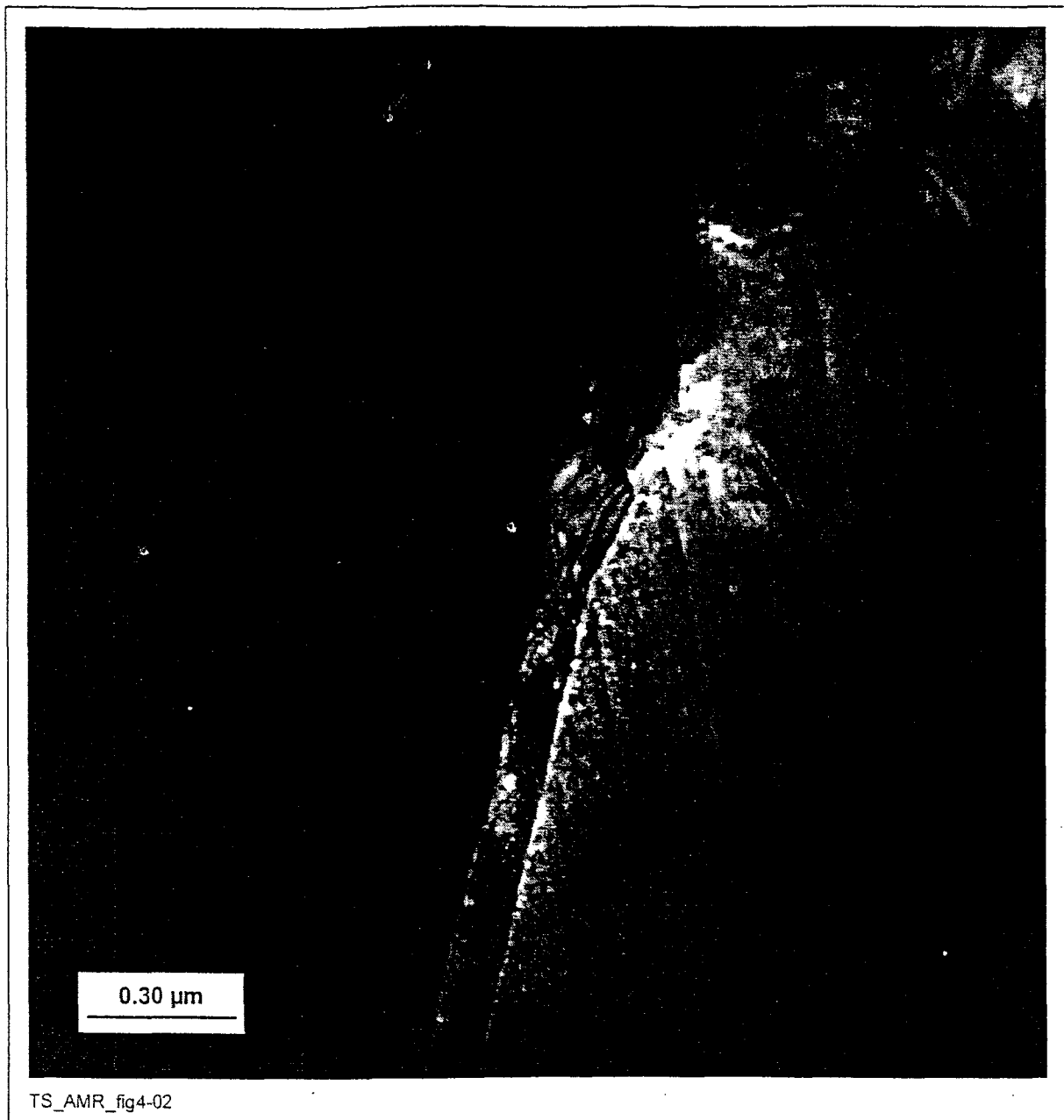
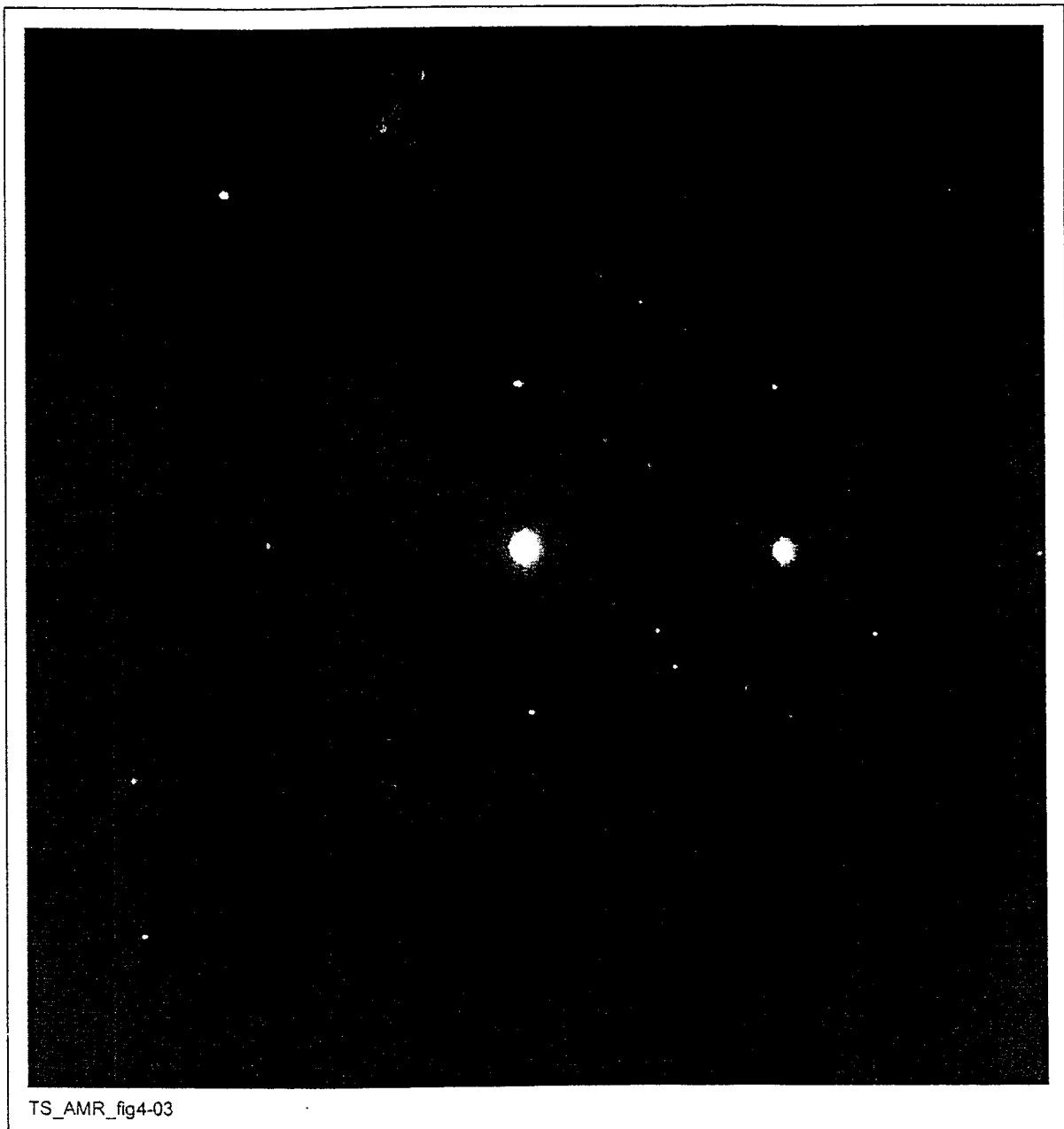


Figure 4-2. Dark-Field Image Corresponding to Figure 4-1

The grain boundary precipitate identified as P appears light. (TS369-003a, Image S0126, 3/9/99, SN #434 p.42)



TS_AMR_fig4-03

Figure 4-3. SAD Pattern from the Grain Boundary Precipitate Shown in Figures 4-1 and 4-2

(TS369-003a, Image S0124, 3/9/99, SN #434 p.43)

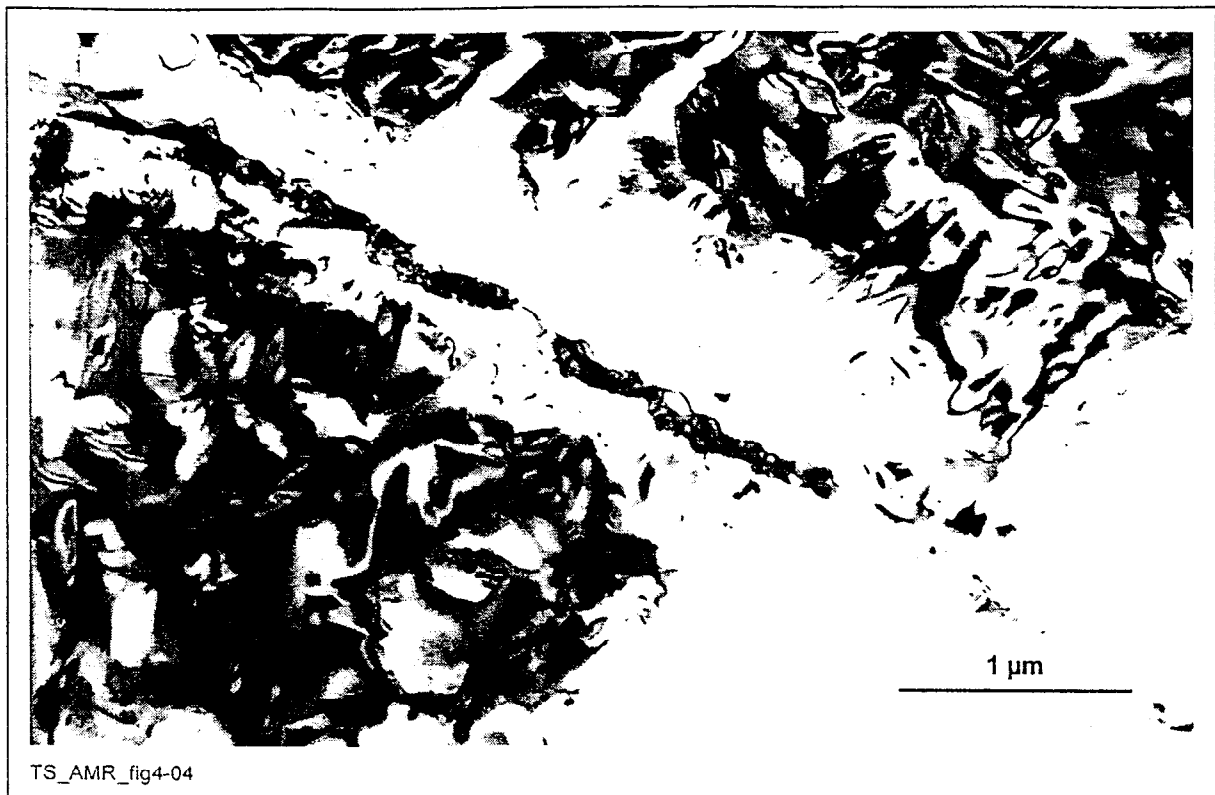


Figure 4-4. Grain Boundary Precipitation in Alloy 22 Aged for 16,000 hr at 593°C

This phase was identified as carbide. (TS369-003a, Image 1490, 12/16/98, SN #393 p.66)

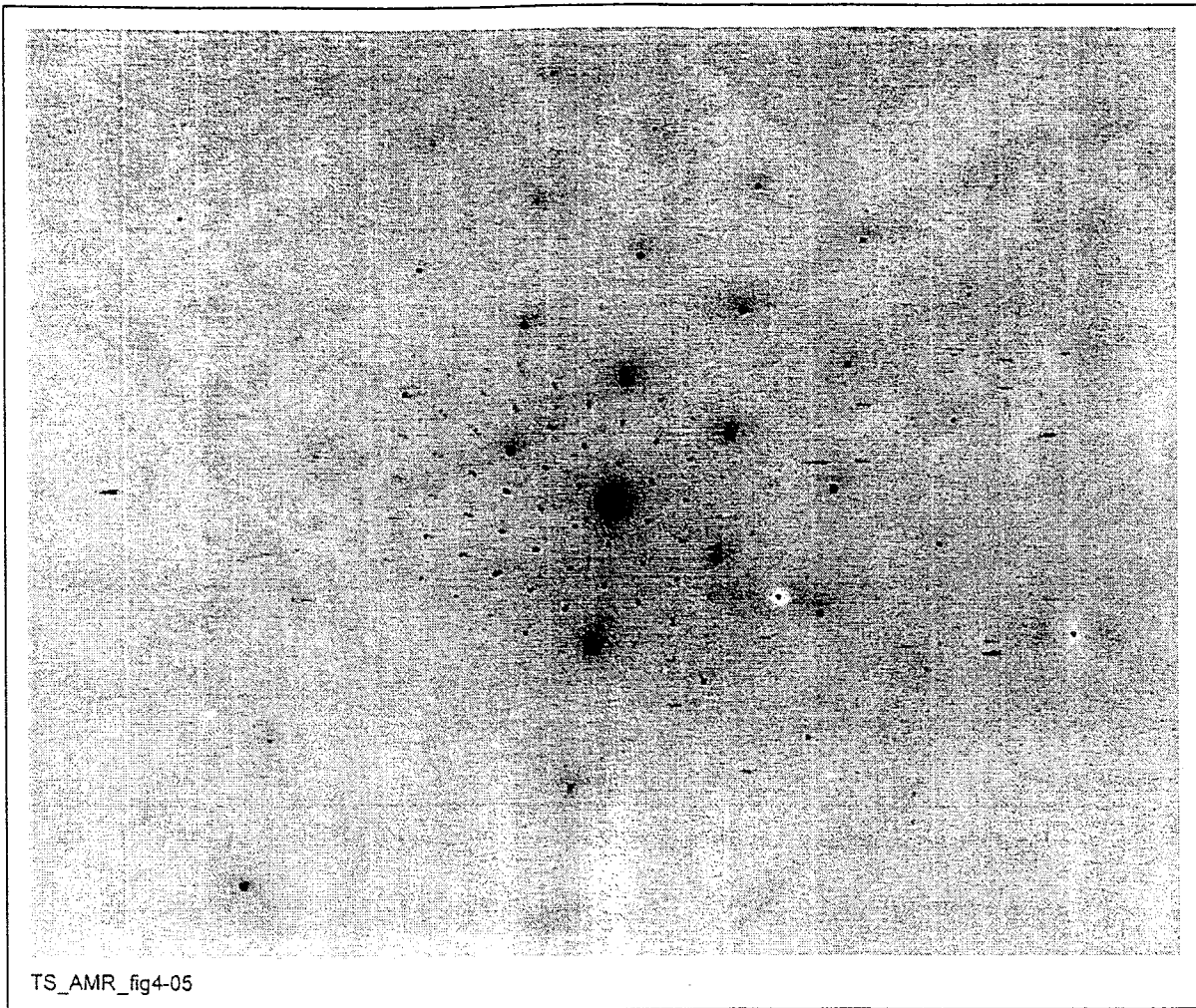


Figure 4-5. SAD Pattern from the Grain Boundary Precipitate Labeled Carbide in Figure 4-4

This pattern was indexed as carbide. (TS369-003a, Image 1489, 12/16/98, SN #393 p. 66)

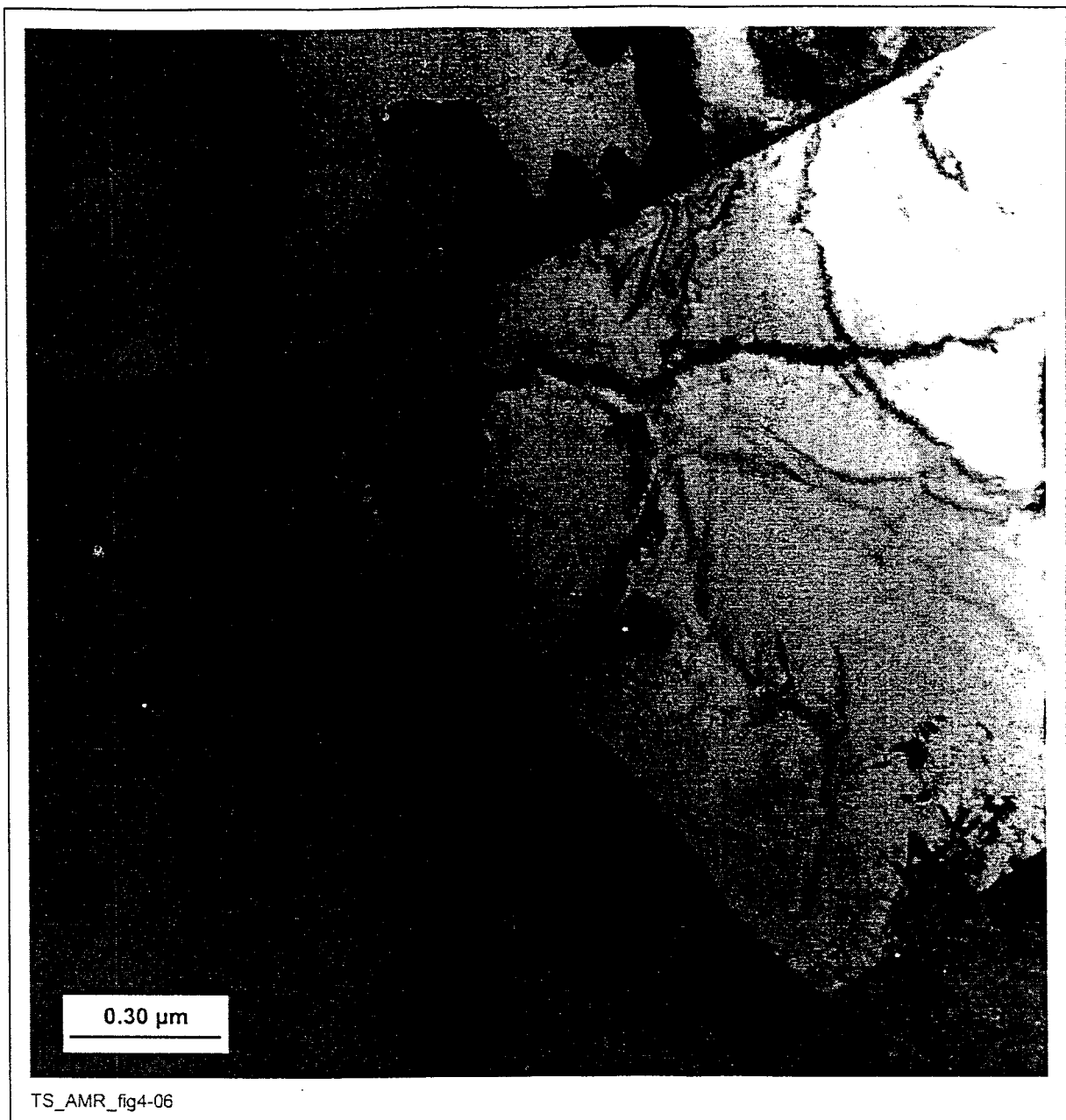


Figure 4-6. Grain Boundary Precipitation in Alloy 22 Aged for 16,000 hr at 649°C

This phase was identified as P phase. (TS369-008a, Image S0152, 3/17/99, SN #434, p.46)

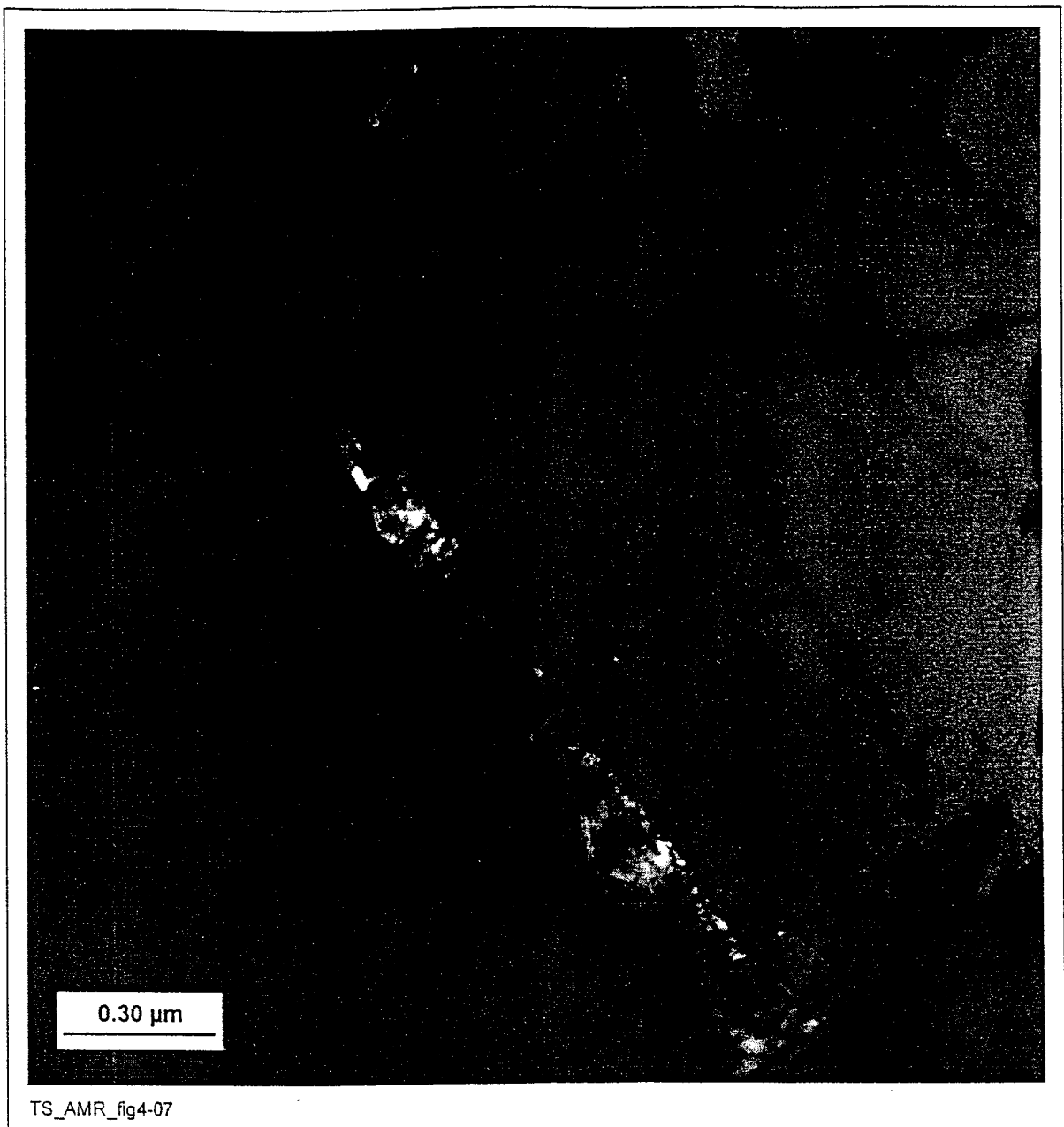


Figure 4-7. Dark-Field Image Corresponding to Figure 4-6

The grain boundary precipitate identified as P appears light. (TS369-008a, Image S0153, 3/17/99, SN #434, p.46)

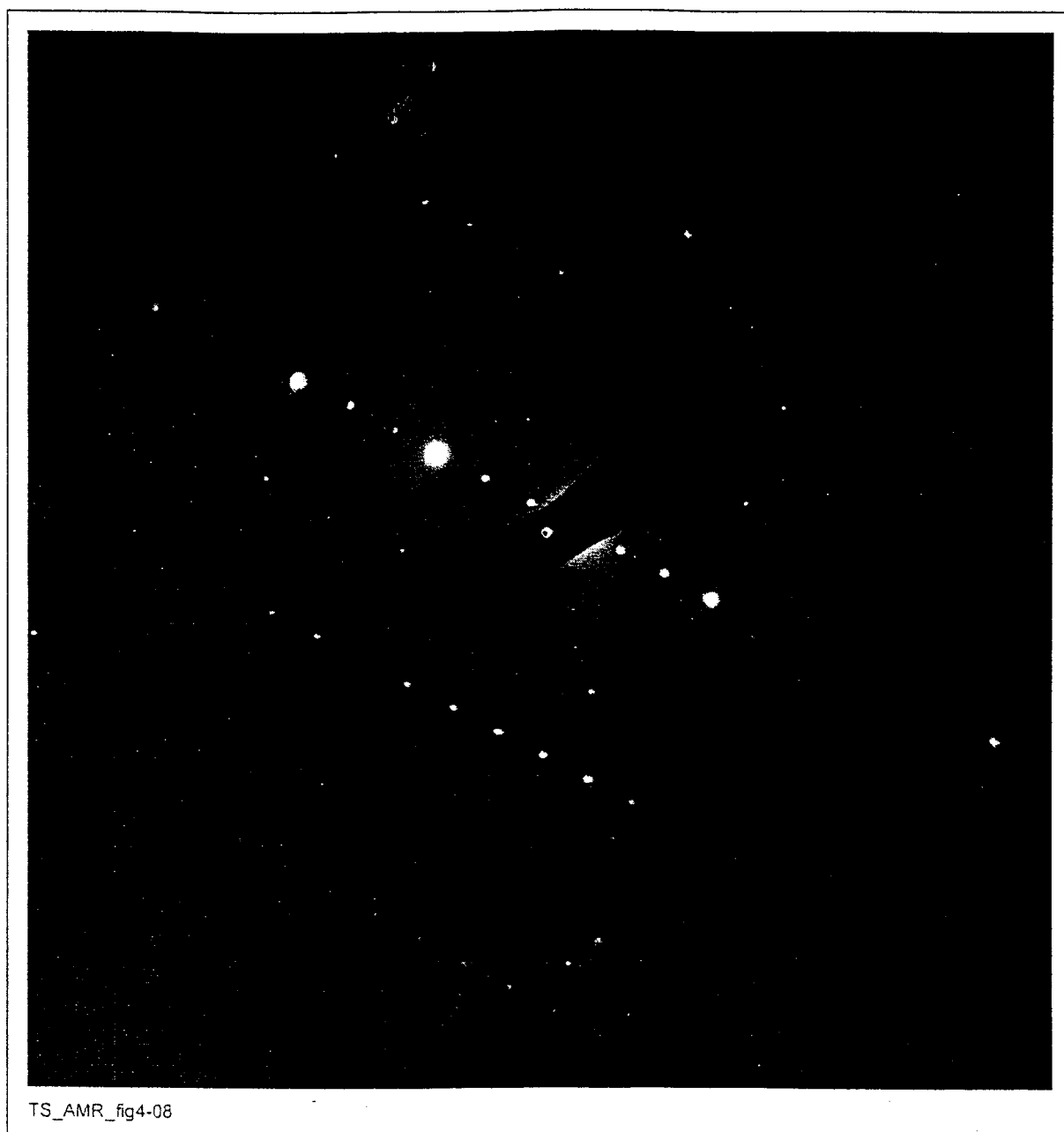


Figure 4-8. SAD Pattern from the Grain Boundary Precipitate Shown in Figures 4-6 and 4-7
(TS369-008a, Image S0151, 3/17/99, SN #434, p.47)



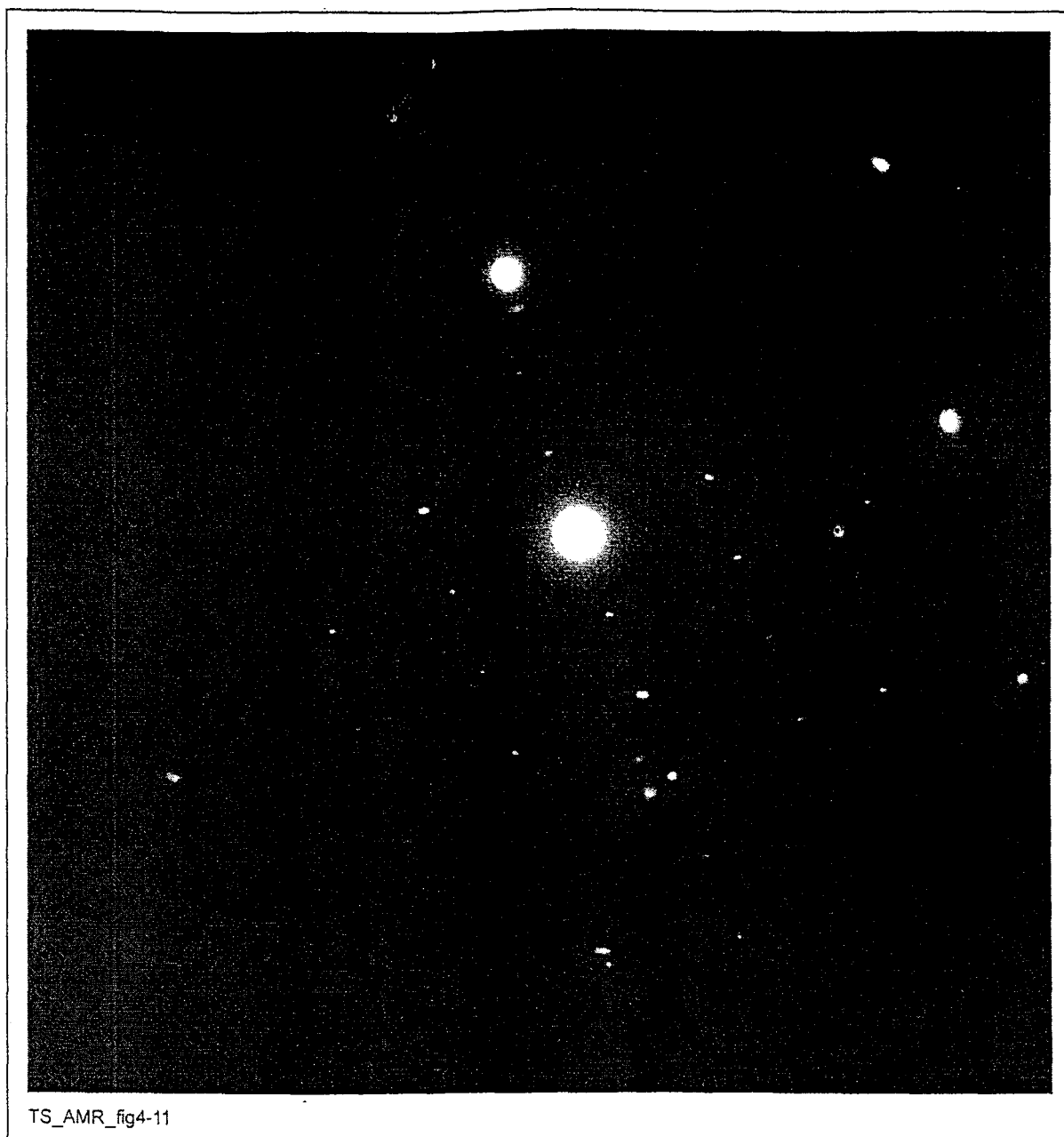
Figure 4-9. Grain Boundary Precipitation in Alloy 22 Aged for 16,000 hr at 649°C

The phase at the grain boundary triple point appears to be μ phase. (TS369-008a, Image S0156, 3/17/99, SN #434, p.49)



Figure 4-10. Dark-Field Image Corresponding to Figure 4-9

The grain boundary precipitate tentatively identified as μ appears light. (TS369-008a, Image S0157, 3/17/99, SN #434, p.49)



TS_AMR_fig4-11

Figure 4-11. SAD Pattern from the Grain Boundary Precipitate Shown in Figures 4-9 and 4-10

(TS369-008a, Image S0155, 3/17/99, SN #434, p.50)

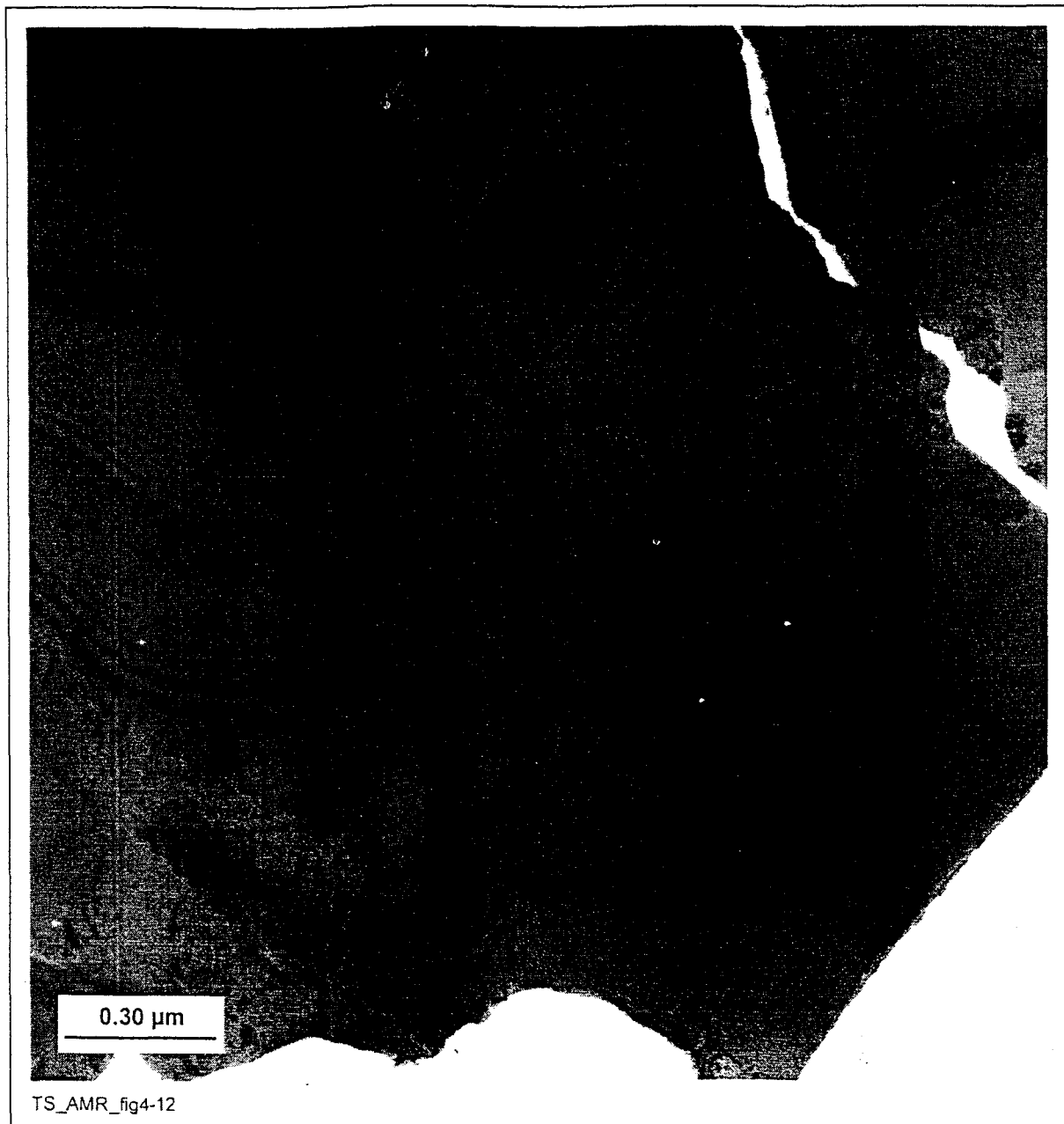


Figure 4-12. Precipitation in Alloy 22 Aged for 16,000 hr at 704°C

This phase was identified as P phase. (TS369-009a, Image S0062, 2/19/99, SN #434, p.60)

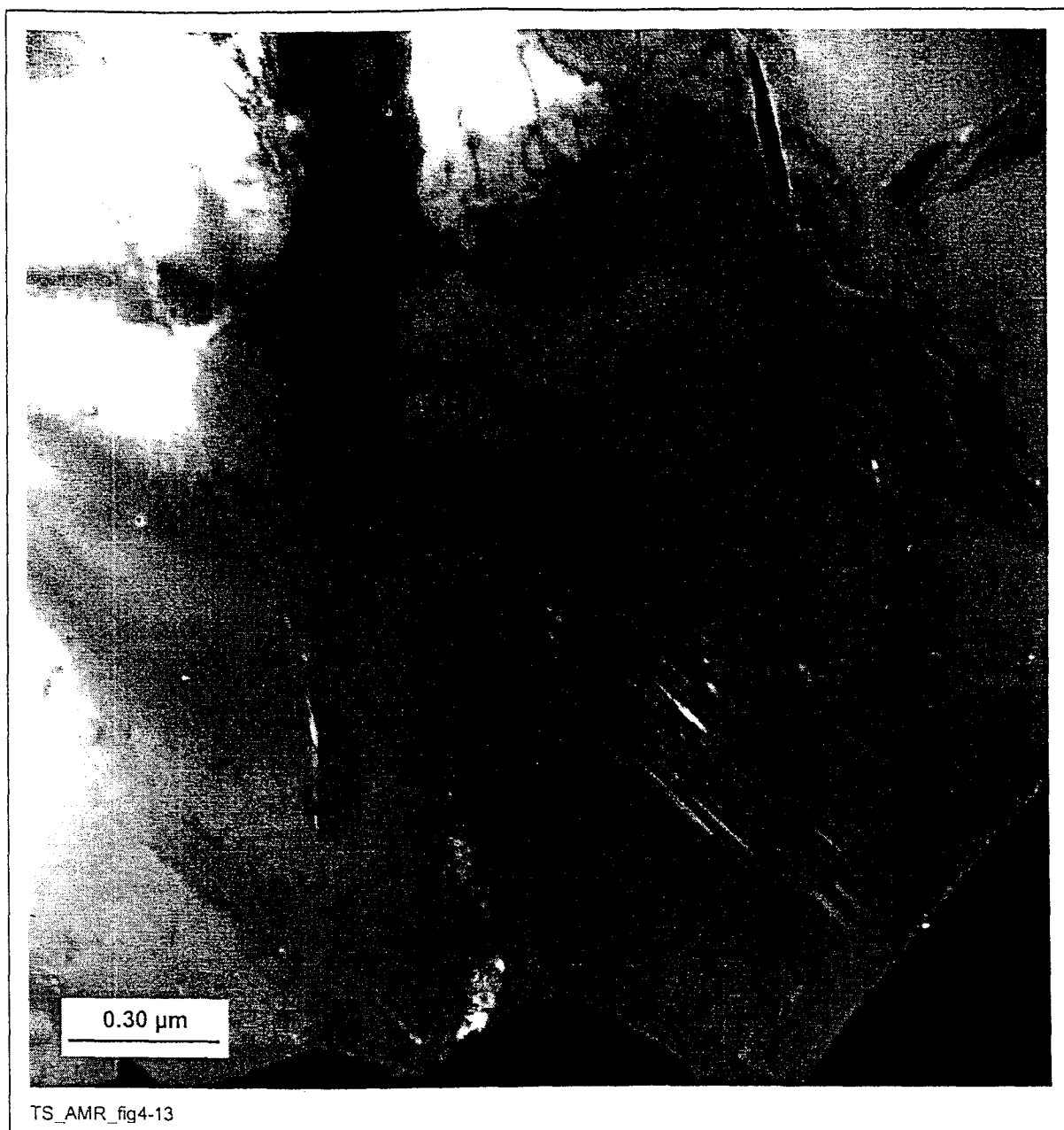
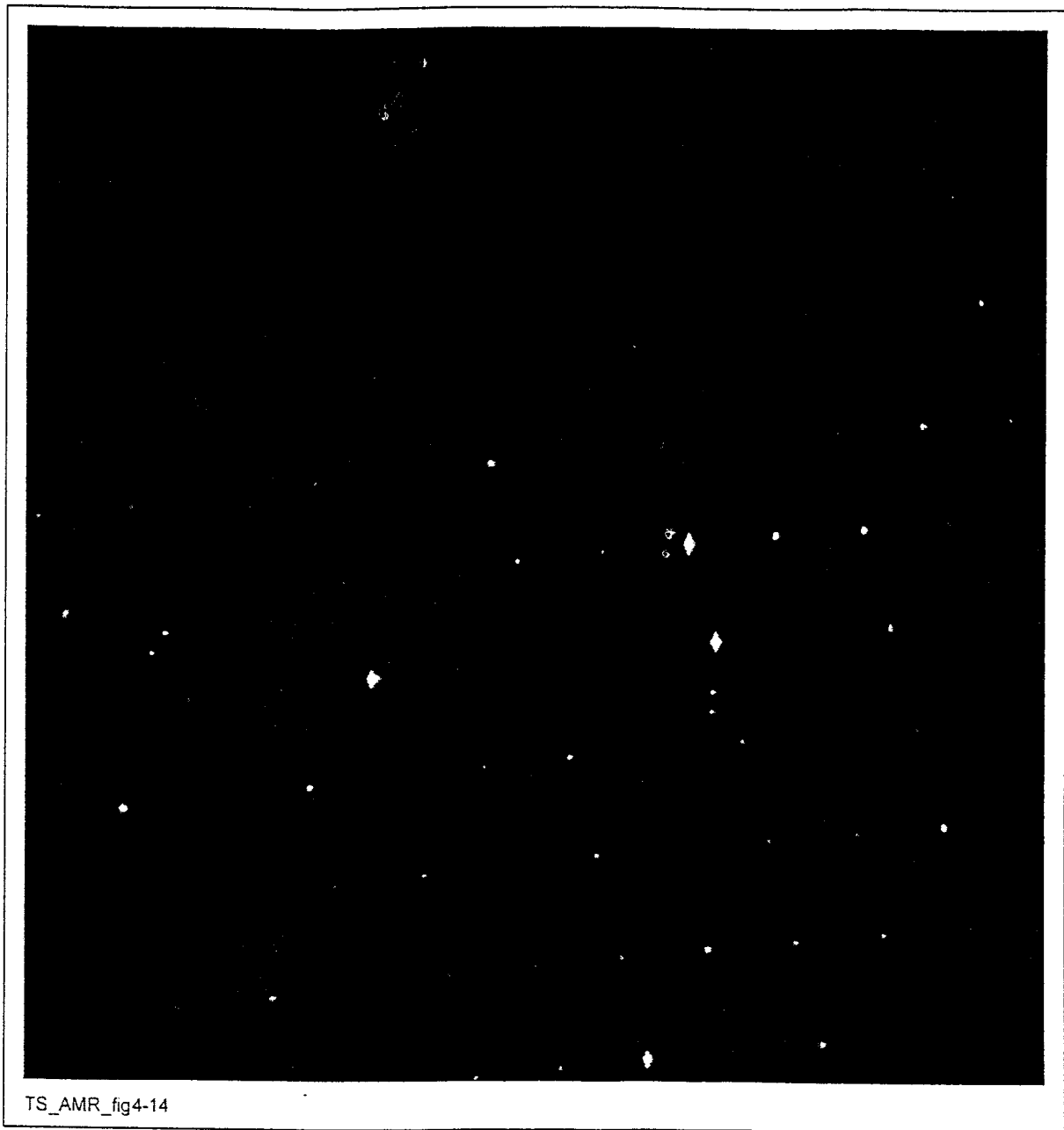


Figure 4-13. Dark-Field Image Corresponding to Figure 4-12

The precipitate identified as P phase appears light. (TS369-009a, Image S0063, 2/19/99, SN #434, p.60)



TS_AMR_fig4-14

Figure 4-14. SAD Pattern from the Precipitate Shown in Figures 4-12 and 4-13

This pattern was indexed as P phase. (TS369-009a, Image S0061, 2/19/99, SN #434, p.61)

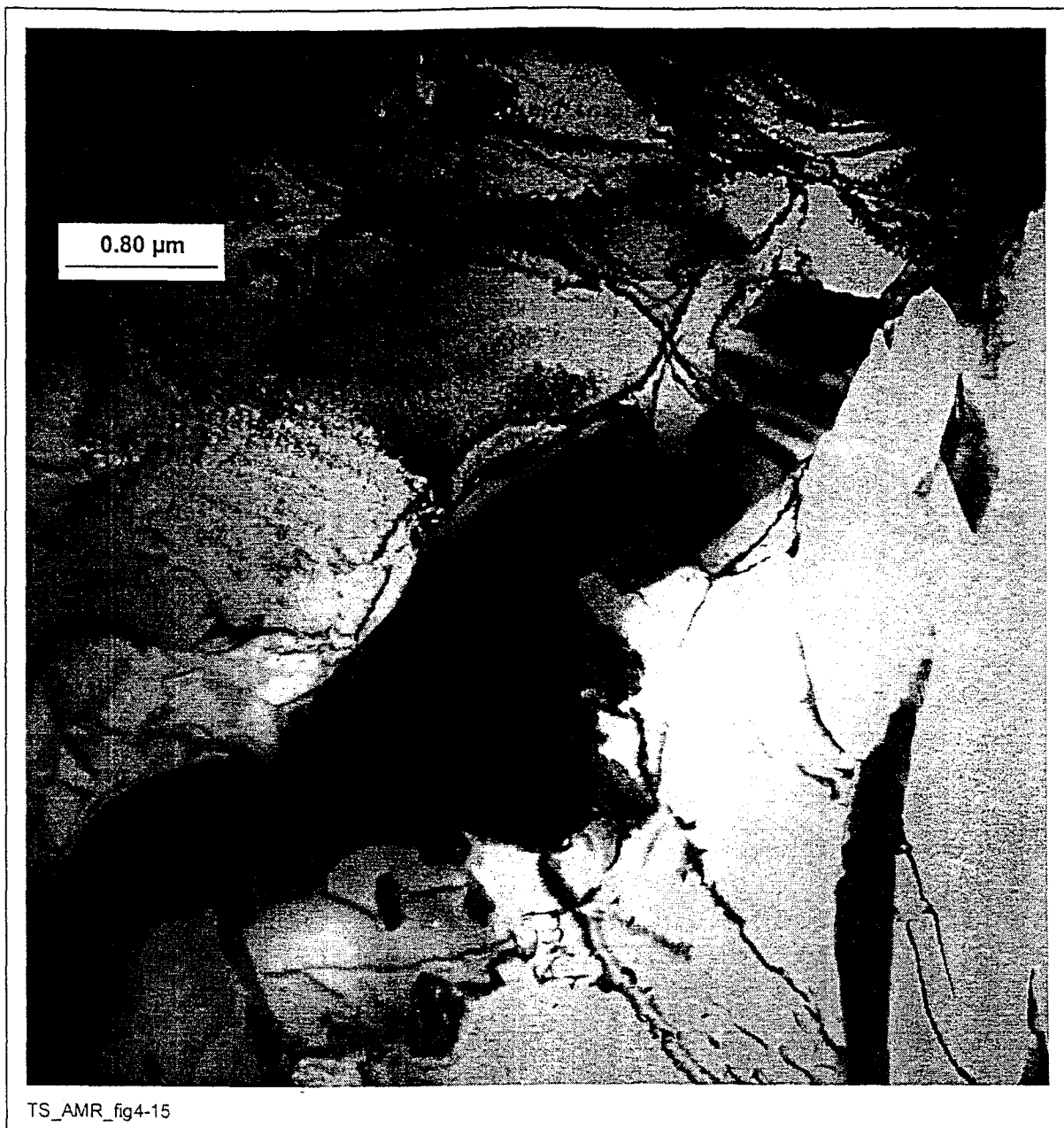


Figure 4-15. Grain Boundary Precipitation in Alloy 22 Aged for 16,000 hr at 704°C

Both carbide and μ phase were identified in this area of the sample. (TS369-009a, Image S0178, 3/17/99, SN #434, p.54)

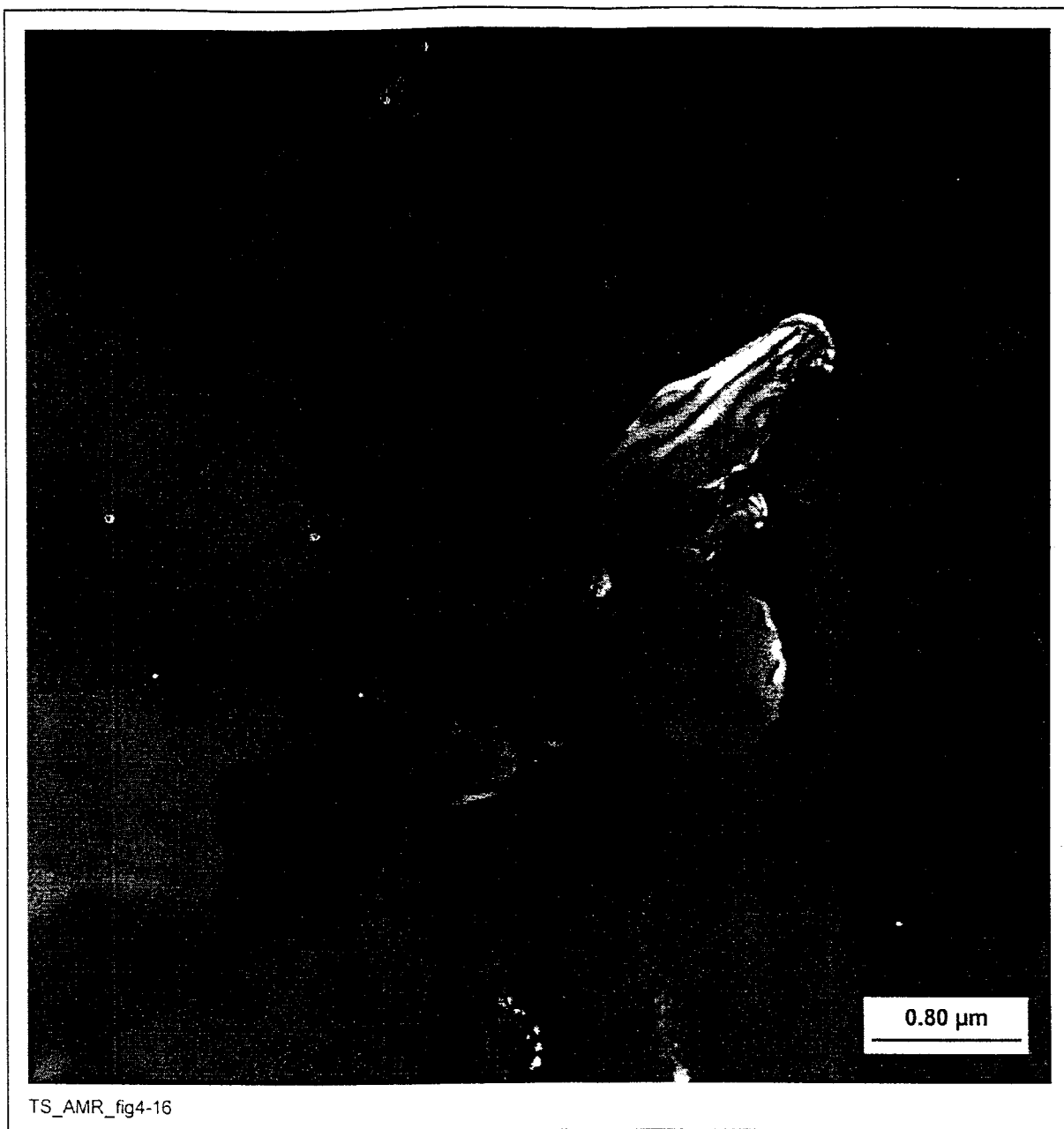
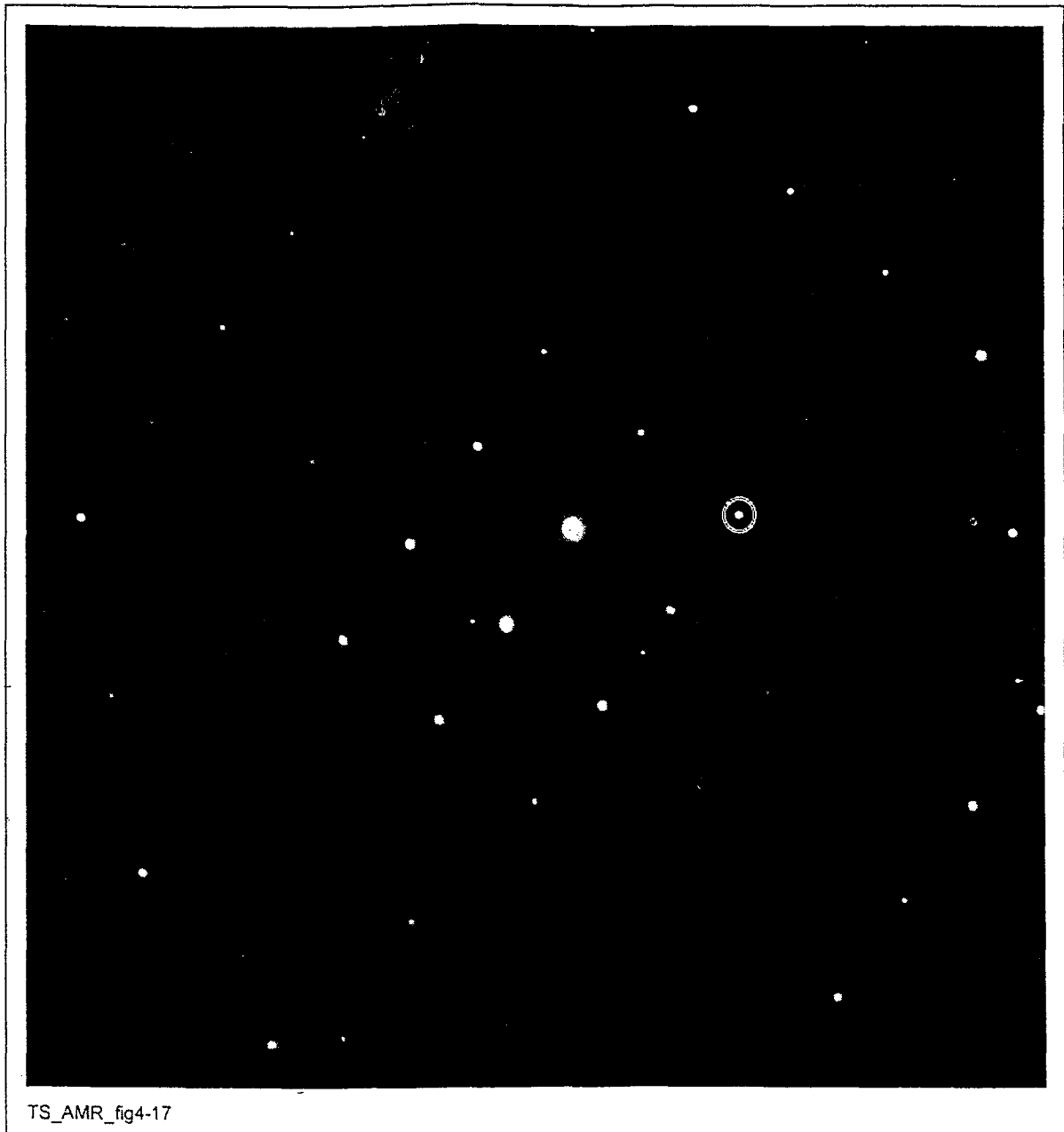


Figure 4-16. Dark-Field Image Corresponding to Figure 4-15

The grain-boundary precipitate identified as carbide appears light. (TS369-009a, Image S0174, 3/17/99, SN #434, p.54)



TS_AMR_fig4-17

Figure 4-17. SAD Pattern from the Grain Boundary Carbide Shown in Figures 4-15 and 4-16

(TS369-009a, Image S0175, 3/17/99, SN #434, p.55)

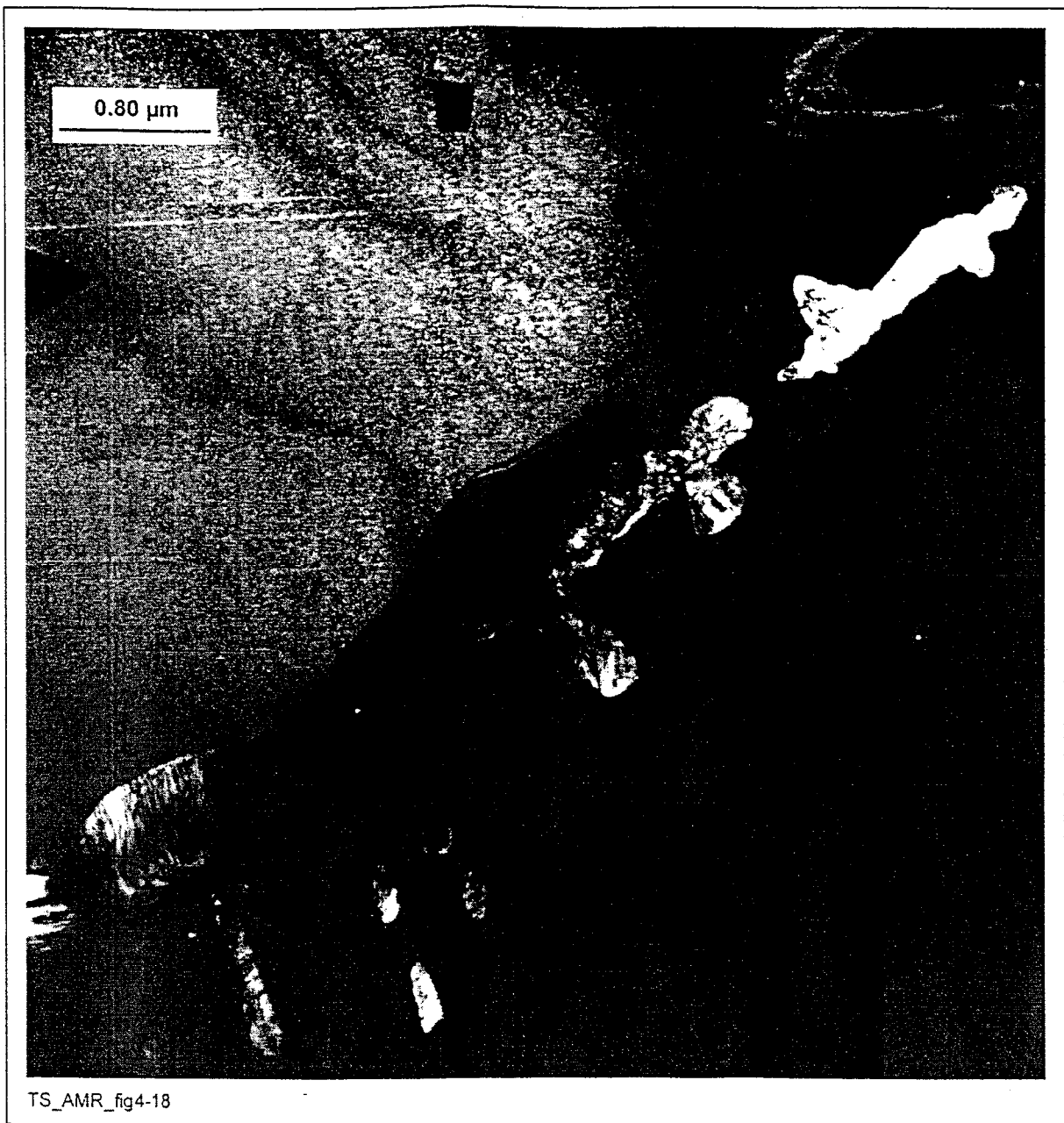
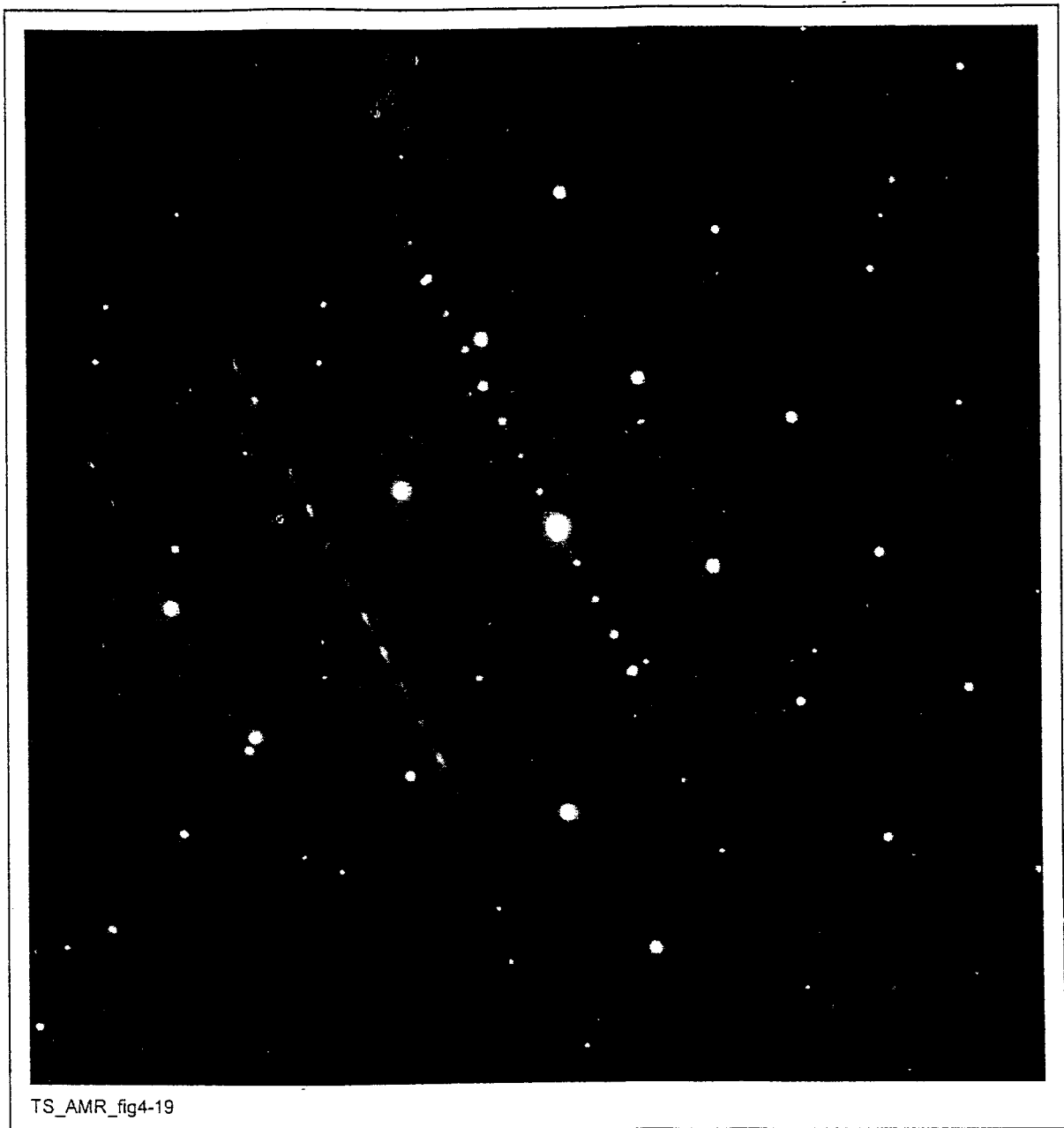


Figure 4-18. Dark-Field Image Corresponding to Figure 4-15

The grain boundary precipitate identified as μ phase appears light. (TS369-009a, Image S0179, 3/17/99, SN #434, p.57)



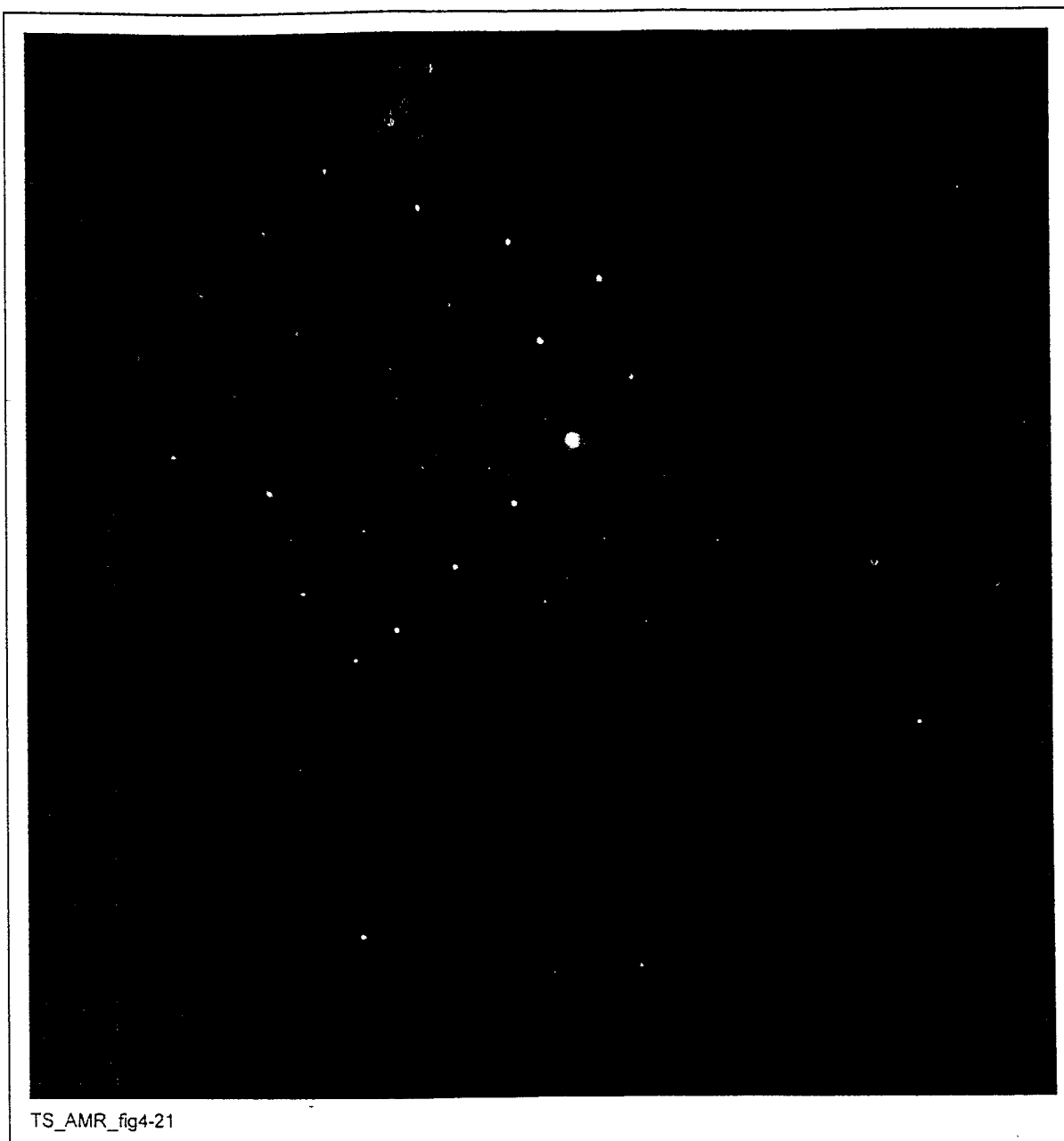
TS_AMR_fig4-19

Figure 4-19. SAD Pattern from the Grain Boundary μ Phase Precipitates Shown in Figures 4-15 and 4-18
(TS369-009a, Image S0180, 3/17/99, SN #434, p.58)



Figure 4-20. Grain Boundary Precipitation in Alloy 22 Aged for 16,000 hr at 704°C

This phase was identified as the carbide phase. (TS369-009a, Image 1883, 10/12/98, SN #393 p.92)



TS_AMR_fig4-21

Figure 4-21. SAD Pattern from the Grain Boundary Precipitate Labeled Carbide in Figure 4-20

This pattern was indexed as carbide. (TS369-009a, Image 1884, 10/12/98, SN #393 p.93)

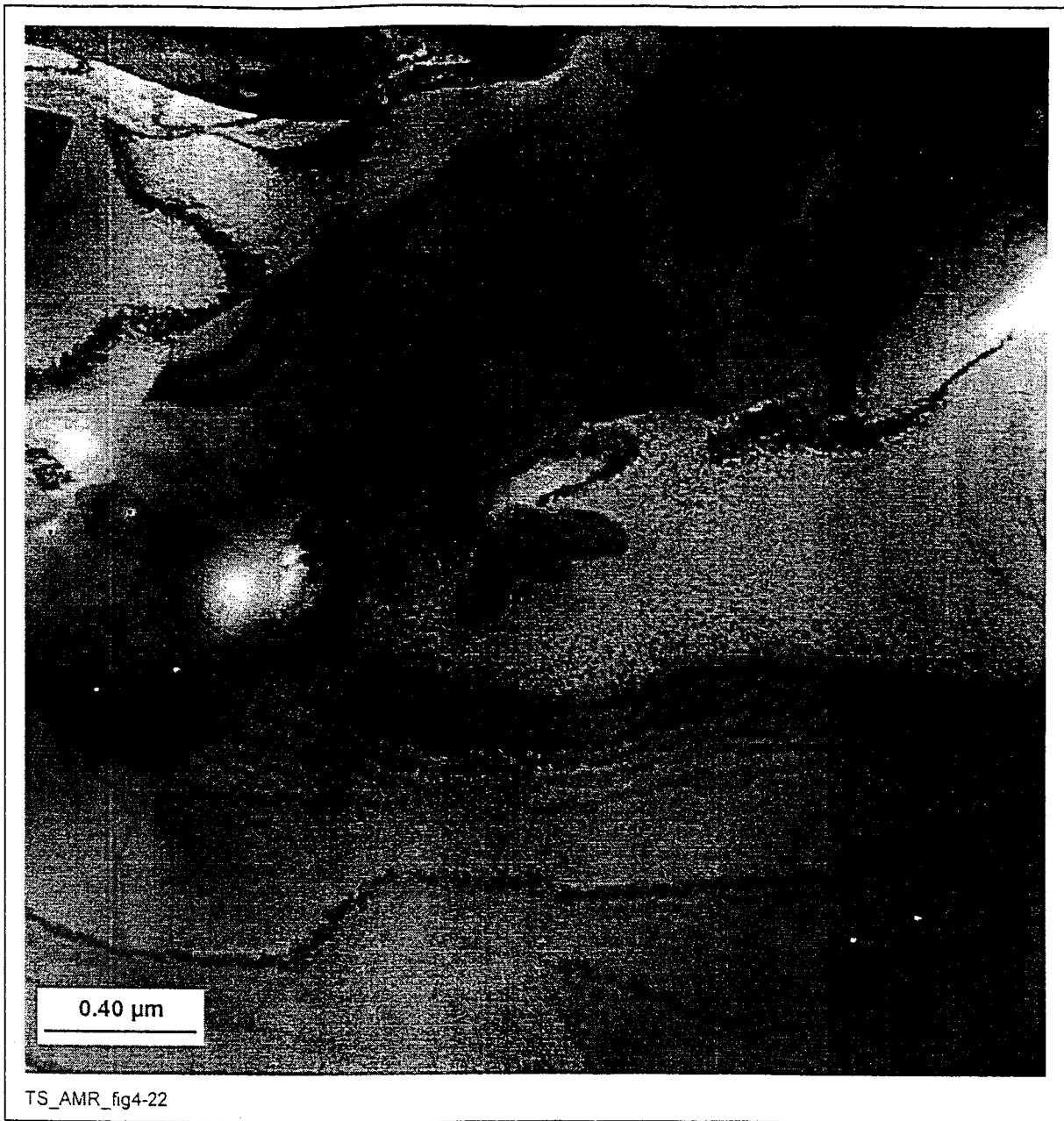


Figure 4-22. Grain Boundary Precipitation in Alloy 22 Aged for 16,000 hr at 704°C

The larger, brighter phase was tentatively identified as sigma phase. The smaller, darker particles appear to be μ phase. (TS369-009a, Image 1880, 10/12/98, SN #393 p.86)

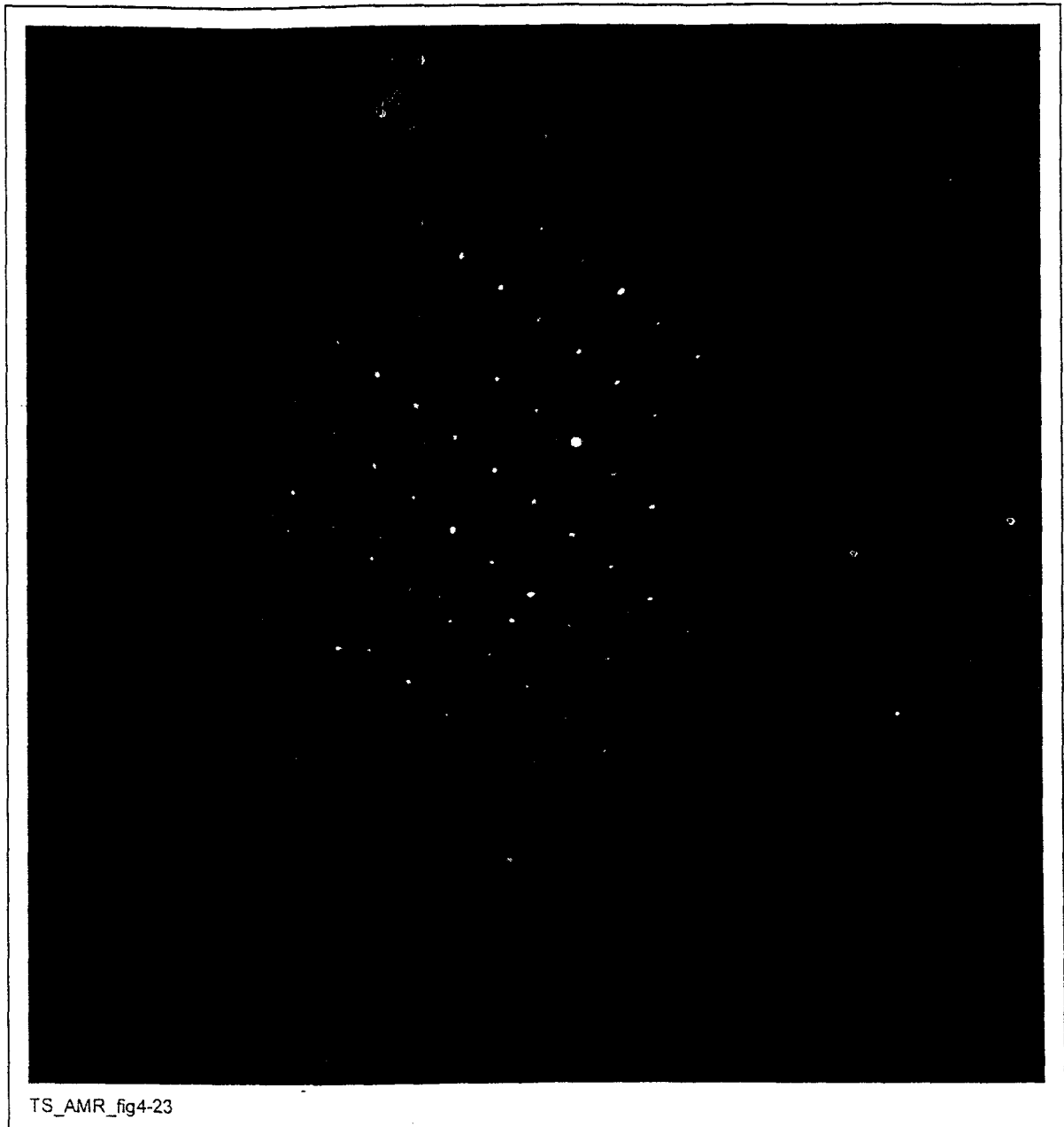
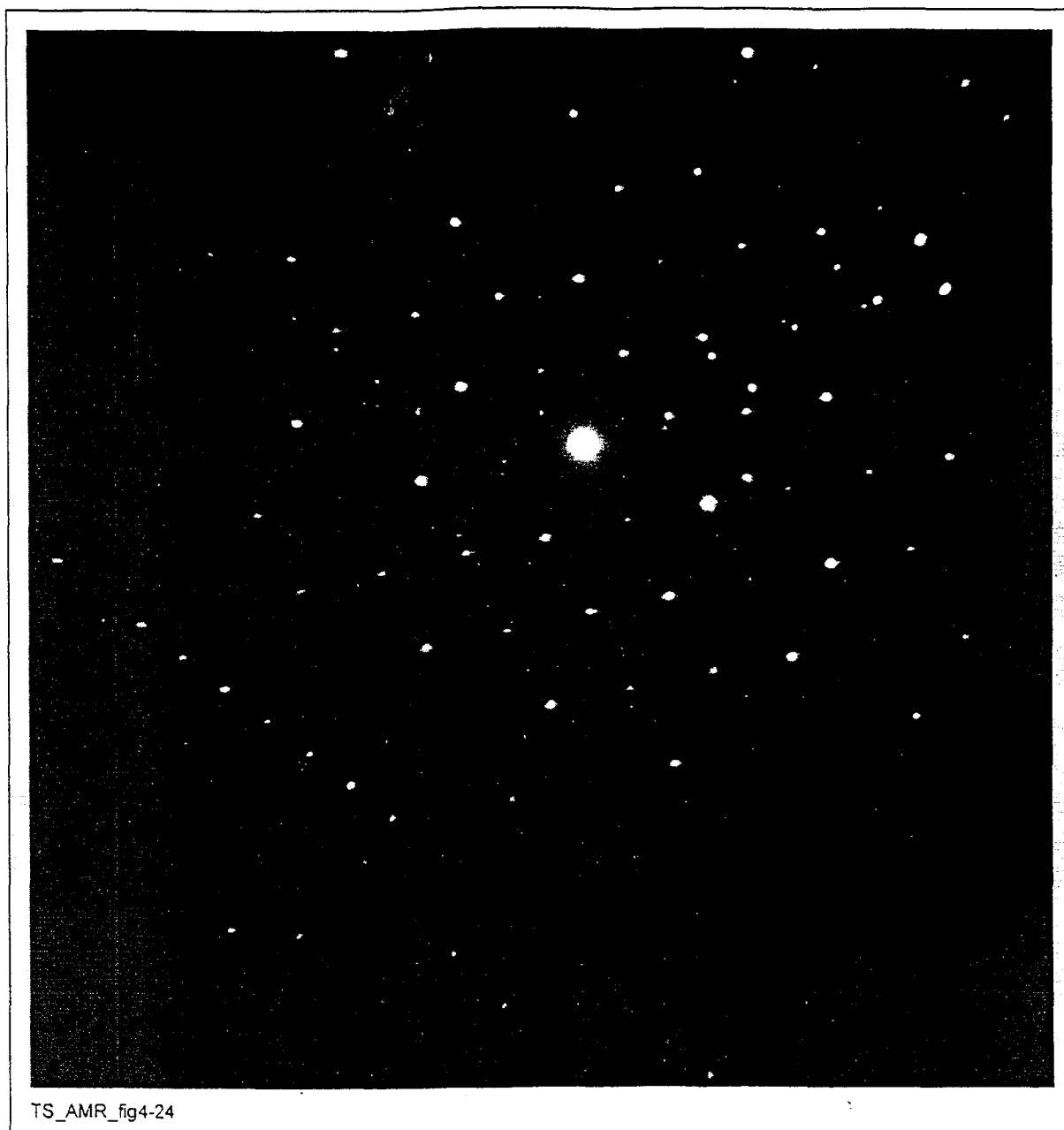


Figure 4-23. SAD Pattern from Sigma Phase in Figure 4-22

(TS369-009a, Image 1881, 10/12/98, SN #393 p.87)



TS_AMR_fig4-24

Figure 4-24. SAD Pattern from the Small, Dark Particles in Figure 4-22

These precipitates were tentatively identified as μ phase. (TS369-009a, Image 1882, 10/12/98, SN #393 p.89)

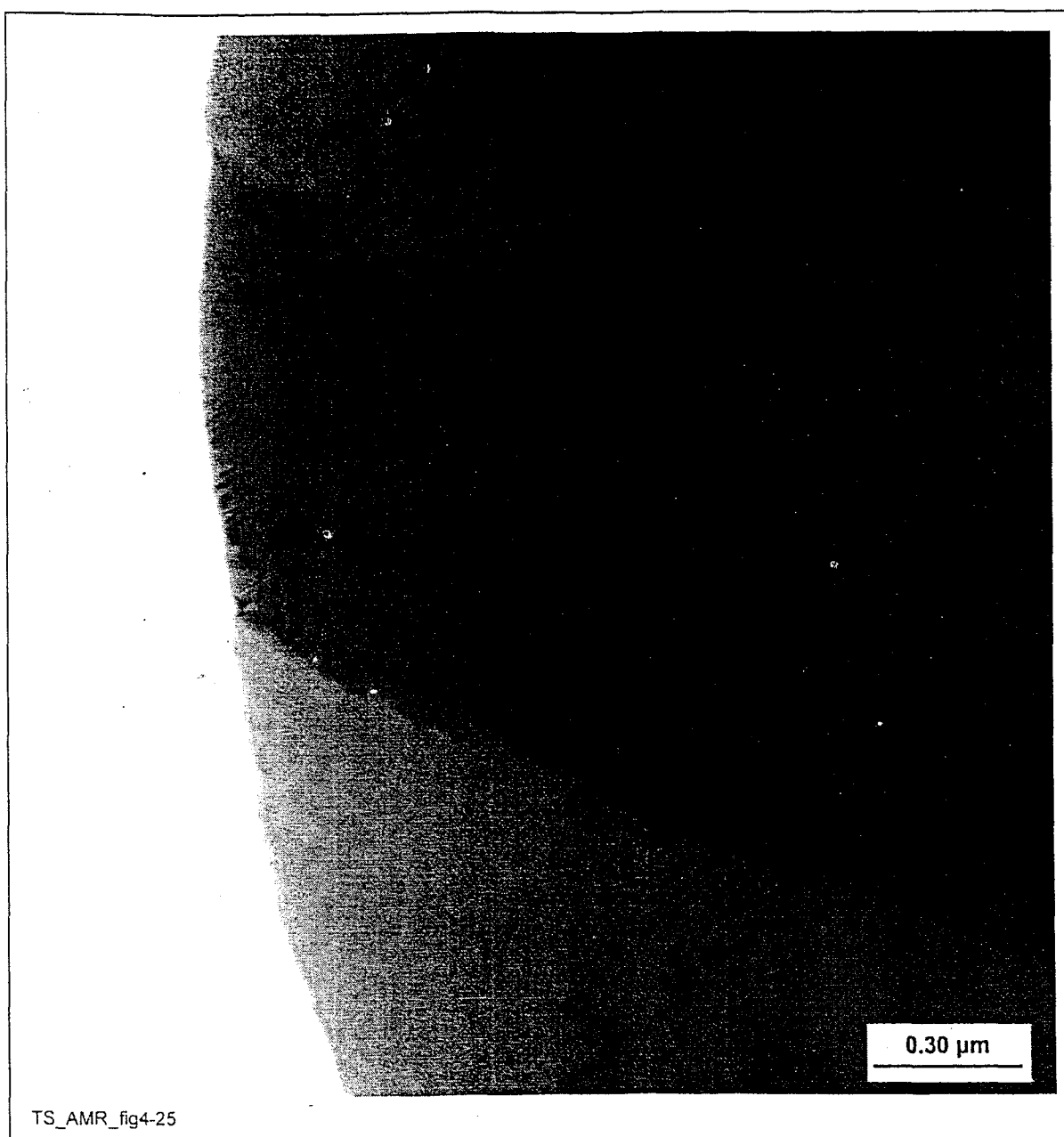


Figure 4-25. Precipitate in Alloy 22 Aged for 16,000 hr at 760°C

This phase was identified as P phase. (TS369-004a, Image S0037, 2/16/99, SN #434 p.63)

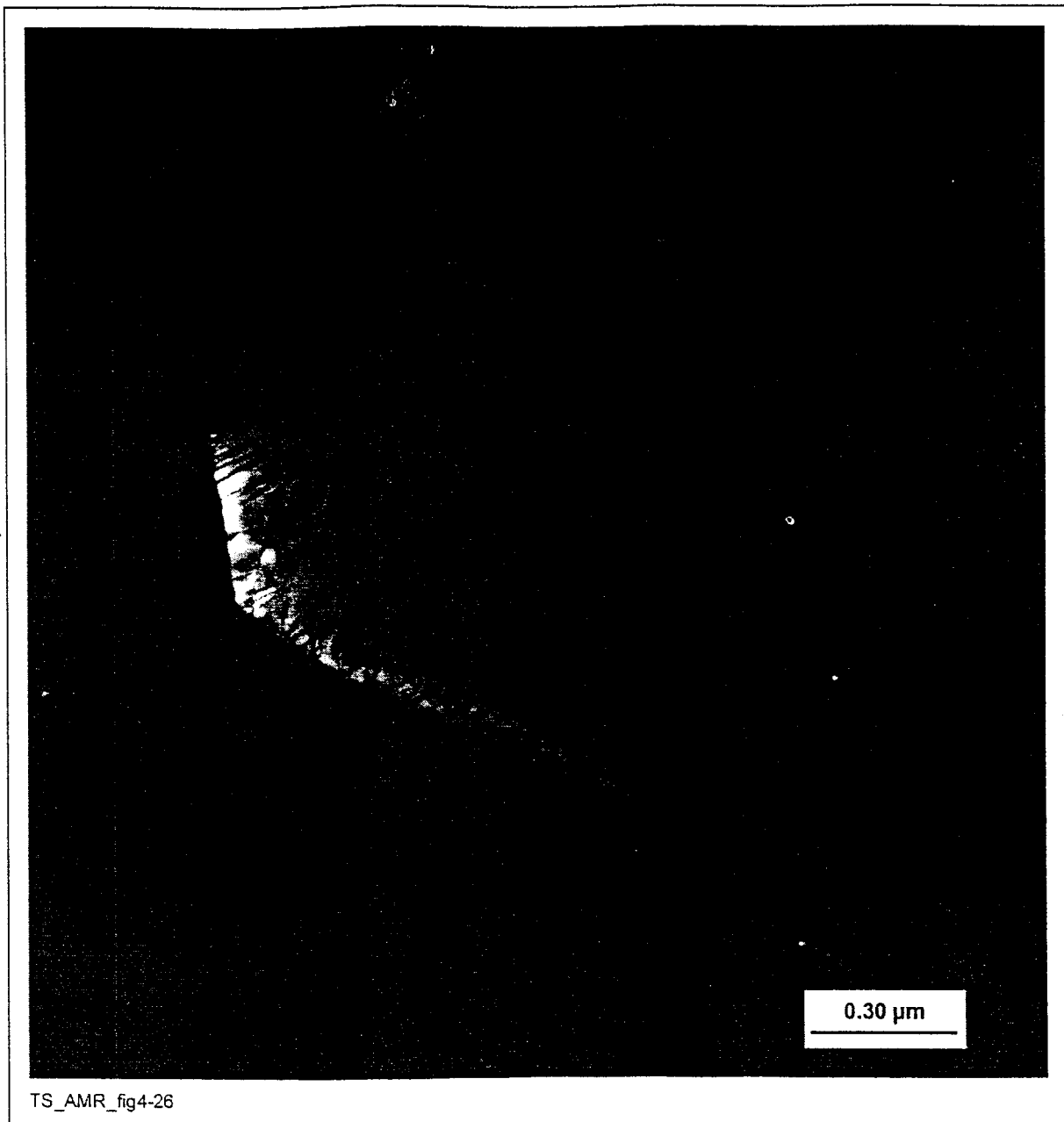
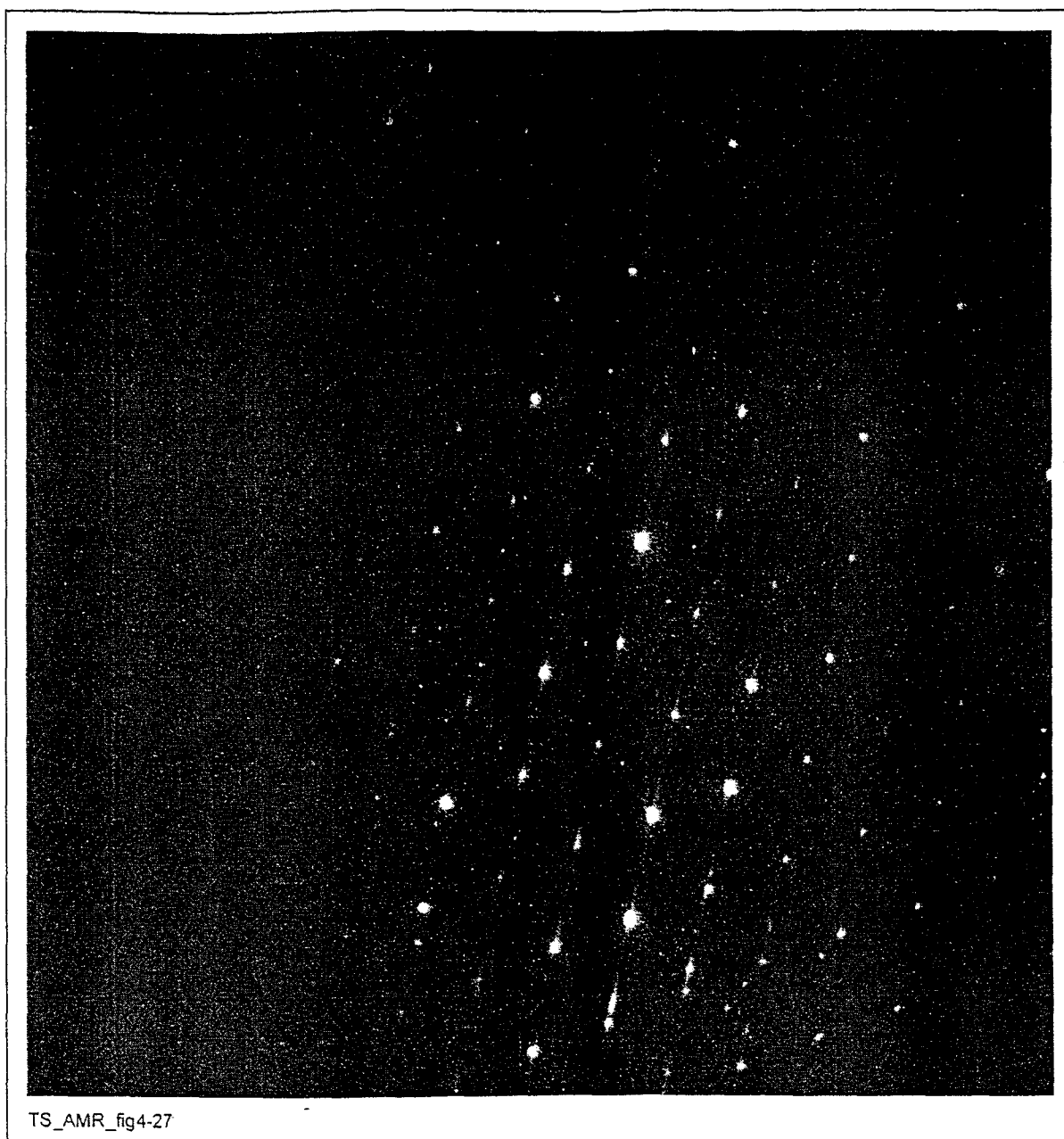


Figure 4-26. Dark-Field Image Corresponding to Figure 4-25

The precipitate identified as P phase appears light. (TS369-004a, Image S0038, 2/16/99, SN #434 p.63)



TS_AMR_fig4-27

Figure 4-27. SAD Pattern from the P Phase Precipitate Shown in Figures 4-25 and 4-26

(TS369-004a, Image S0036, 2/16/99, SN #434 p.64)



Figure 4-28. Grain Boundary Precipitation in Alloy 22 Aged for 16,000 hr at 760°C

The larger, brighter phase was identified as sigma. The smaller precipitates are either μ or P phase.
(TS369-004a, Image 1300, 3/14/98, SN #369, p.66)

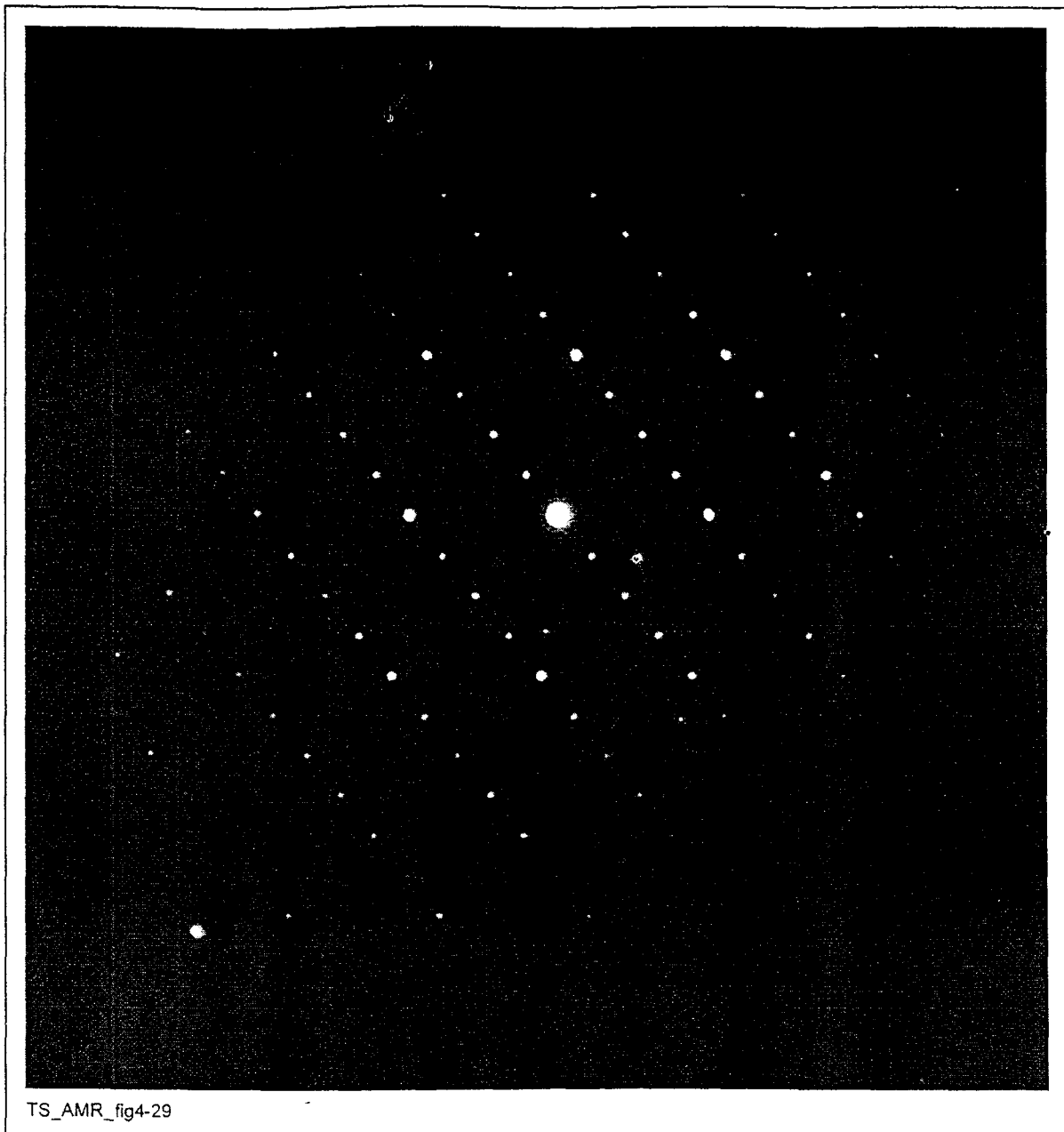
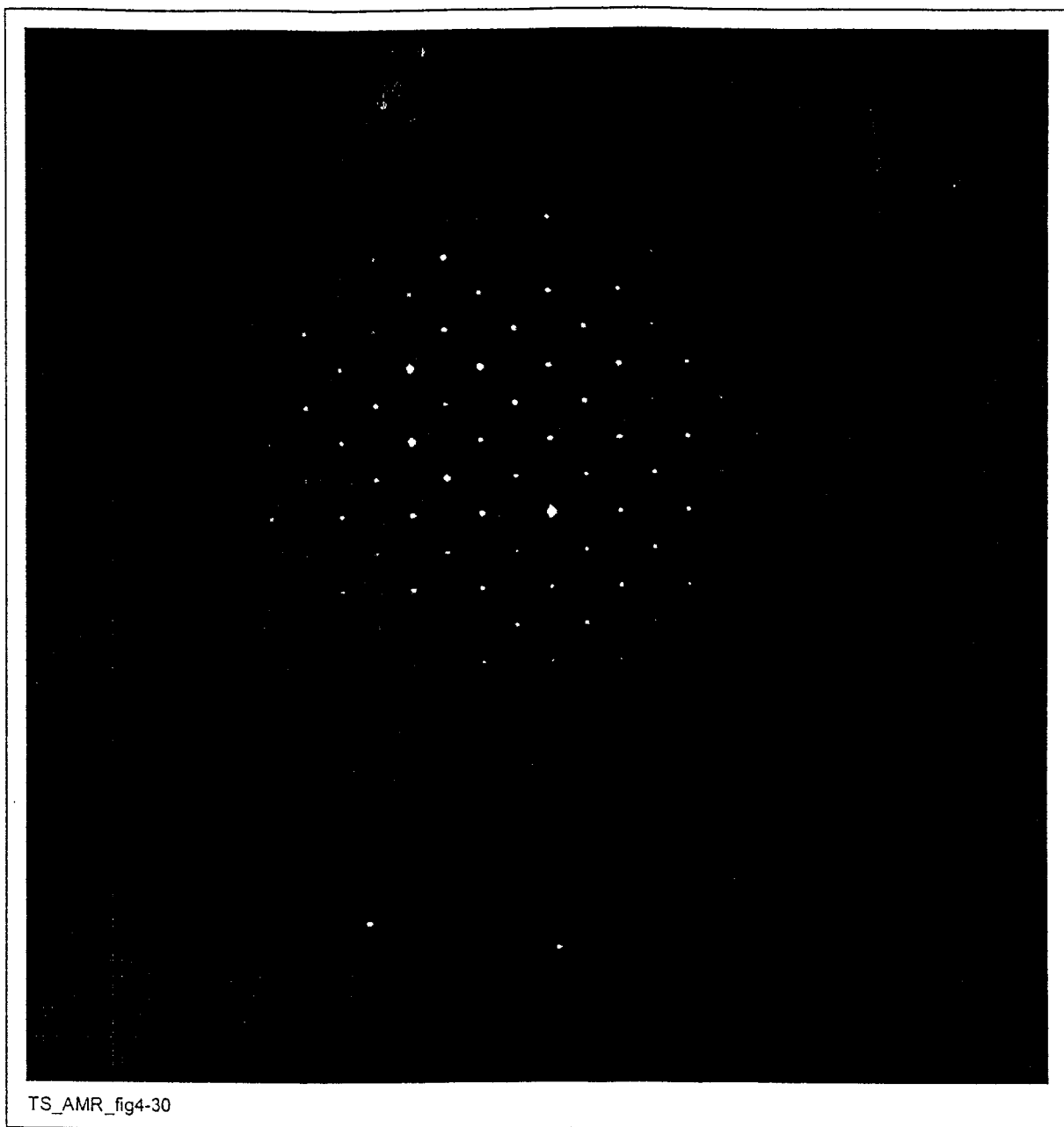


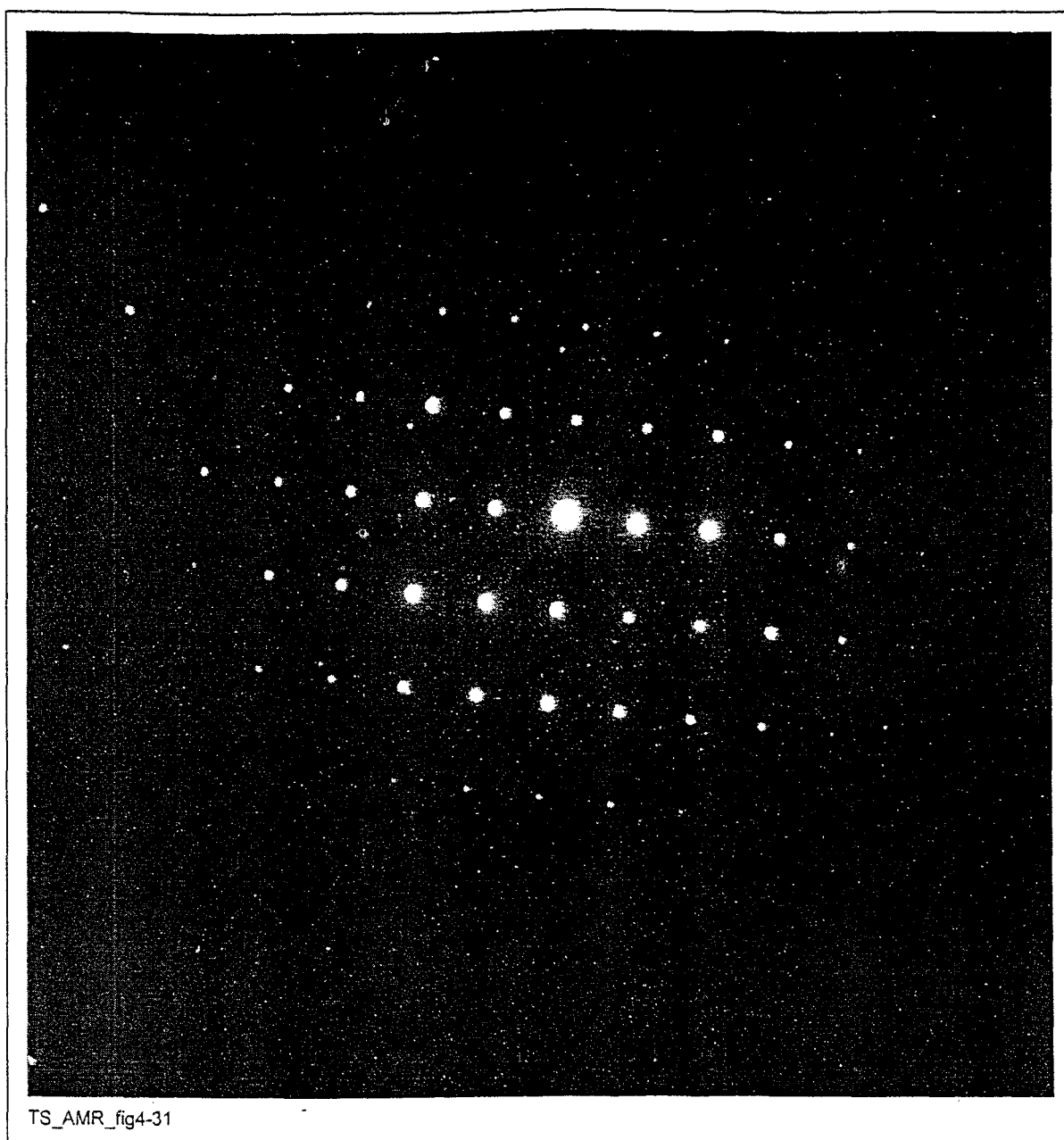
Figure 4-29. SAD Pattern from the Sigma Phase Precipitate Shown in Figure 4-28
(TS369-004a, Image 1306, tilted $(-11, -9)$ from image 1300, 3/14/98, SN #369, p.98)



TS_AMR_fig4-30

Figure 4-30. SAD Pattern from the Sigma Phase Precipitate Shown in Figure 4-28

(TS369-004a, Image 1307, tilted $(-10,+18)$ from image 1300, 3/14/98, SN #369, p.106)



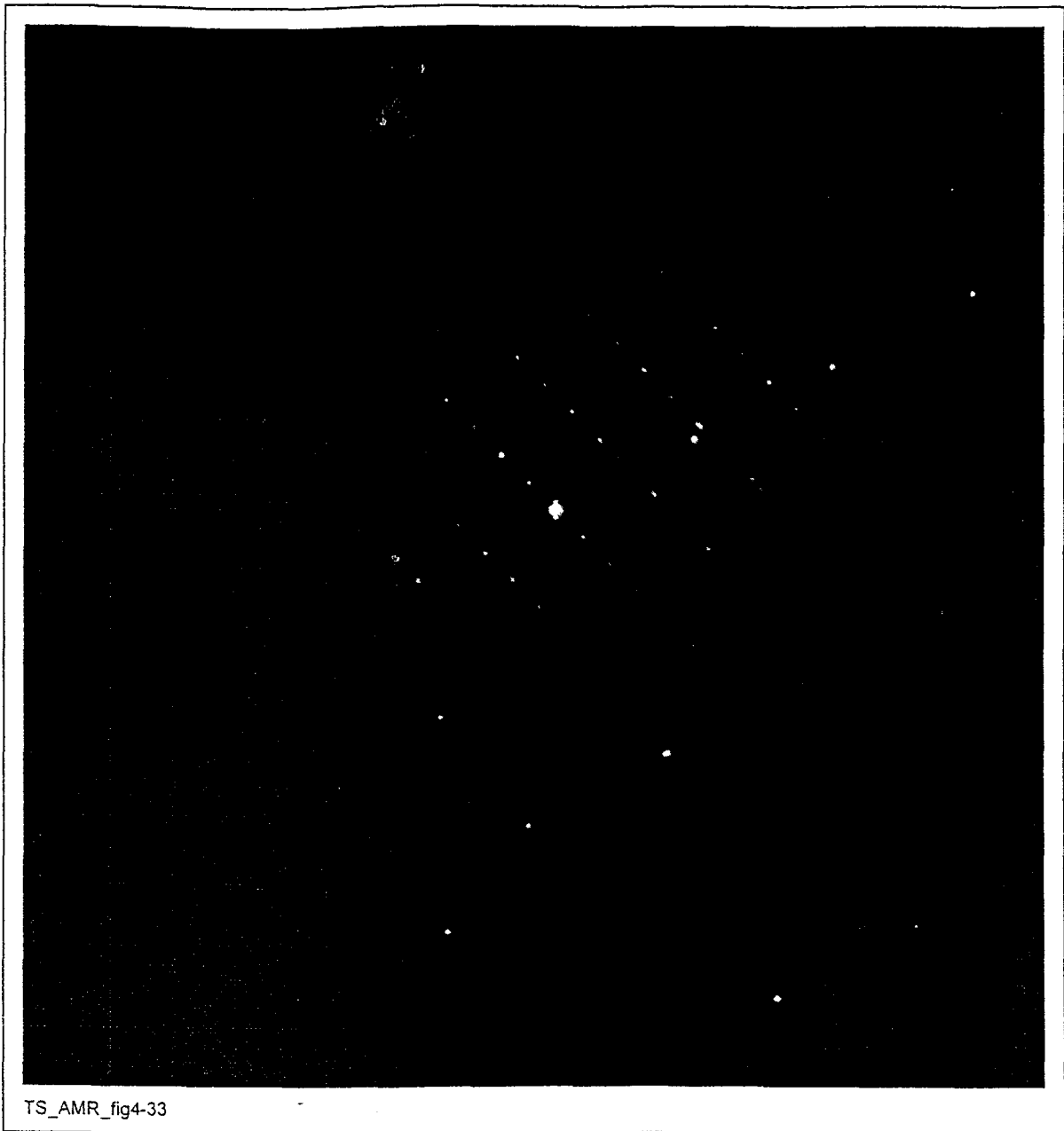
TS_AMR_fig4-31

Figure 4-31. SAD Pattern from the Sigma Phase Precipitate Shown in Figure 4-28
(TS369-004a, Image 1308, tilted $(-35, -2)$ from image 1300, 3/14/98, SN #369, p.113)



Figure 4-32. Precipitation in Alloy 22 Aged for 16,000 hr at 760°C

This phase was tentatively identified as μ phase. (TS369-004a, Image 1312, 3/14/98, SN #393, p.11)



TS_AMR_fig4-33

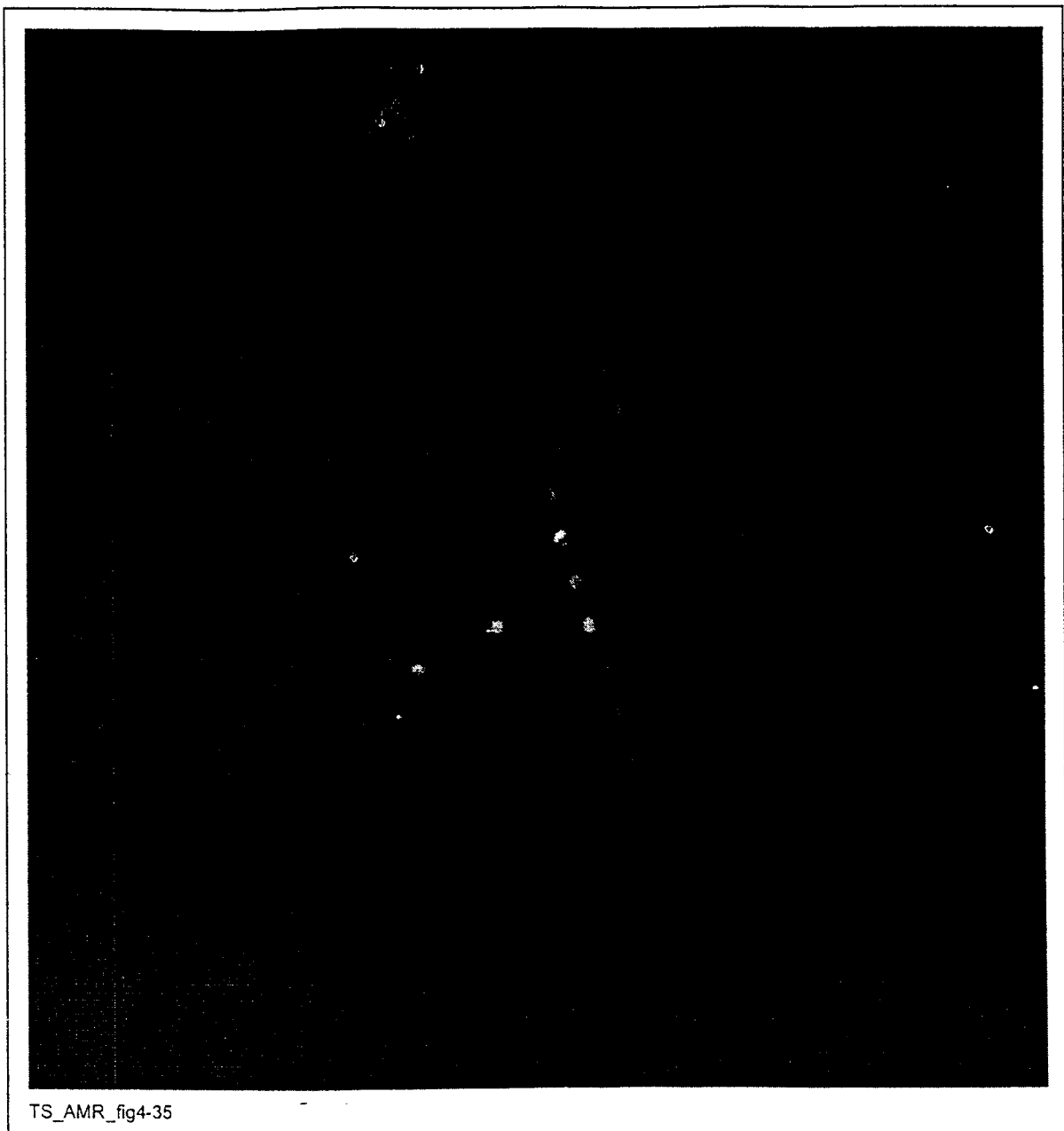
Figure 4-33. SAD Pattern from the μ Phase Precipitate Shown in Figure 4-28

(TS369-004a, Image 1314, 3/14/98, SN #393, p.13)



Figure 4-34. Grain Boundary Precipitation in Alloy 22 Aged for 16,000 hr at 760°C

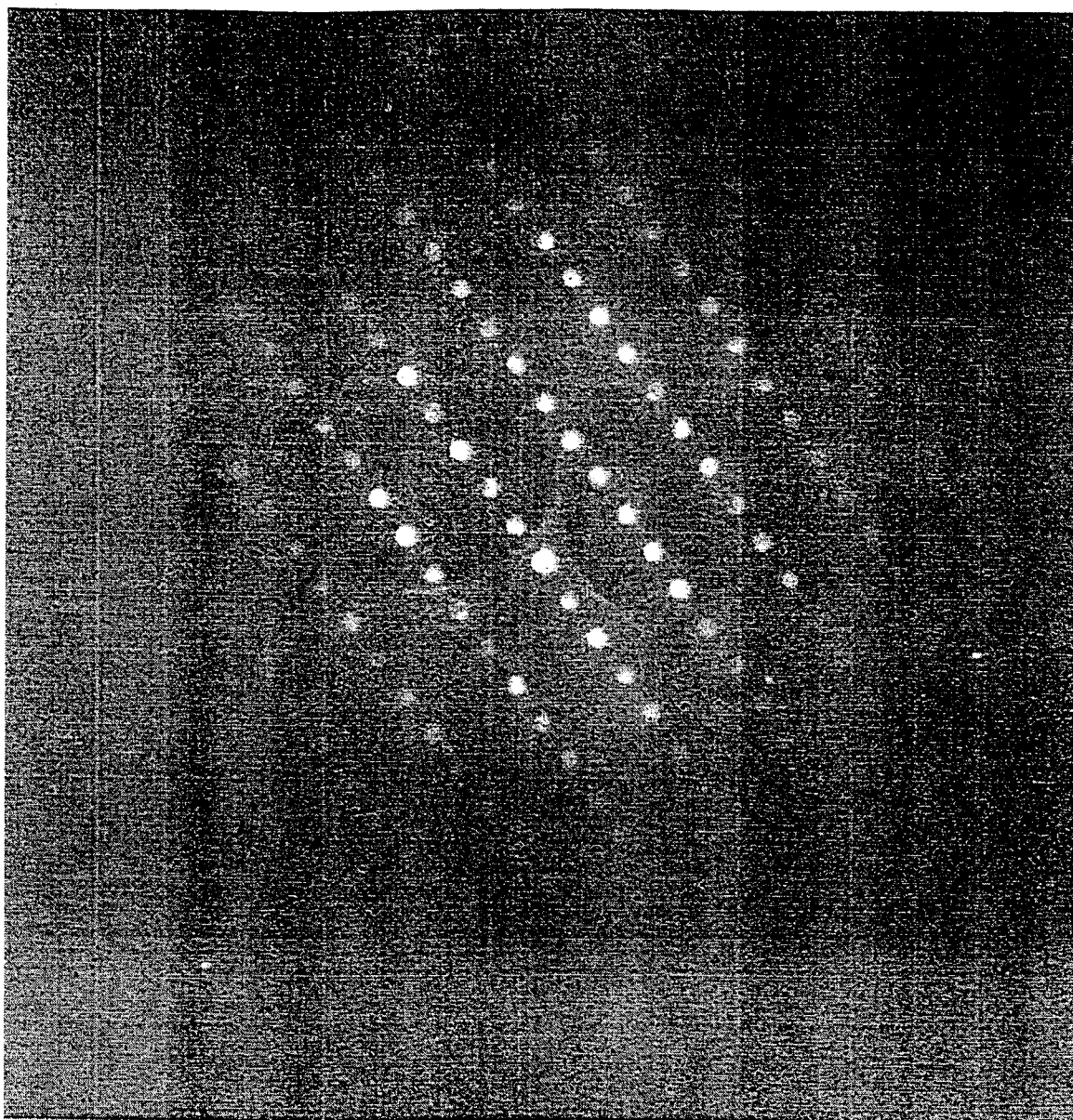
This phase was identified as μ phase. (TS369-004a, Image 1309, 3/14/98, SN #369, p.135)



TS_AMR_fig4-35

Figure 4-35. SAD Pattern from the μ Phase Precipitate Shown in Figure 4-34

(TS369-004a, Image 1310, 3/14/98, SN #369, p.150)



TS_AMR_fig4-36

Figure 4-36. SAD Pattern from the μ Phase Precipitate in Figure 4-34

(TS369-004a, Image 1311, 3/14/98, SN #369, p.153)

4.1.2 TEM Micrographs Used for Identification of Phases Forming in Alloy 22 as a Function of Aging Time and Temperature (to be determined [TBD]-427)

The TEM micrographs from the samples in Section 4.1.1 were taken from samples aged for 16,000 hr at 593, 649, 704, and 760°C. Samples aged for shorter time intervals have not been examined in TEM; thus, evolution of the phases during aging is not known. The phases precipitating during aging must be characterized as a function of aging time and temperature.

4.1.3 X-Ray Diffraction Data Used for Quantification and Identification of Phases Forming in Alloy 22 as a Function of Aging Time and Temperature (TBD-426)

When a large number of precipitates is involved, TEM diffraction analysis is a cumbersome method of phase identification. This is especially true when the crystal structures of the various phases are similar. A single SAD pattern often is not enough to distinguish the phases that form in Alloy 22. Two patterns with a known tilt between them frequently must be analyzed. A procedure is being developed to extract the intermetallic and carbide phases from the Ni-base matrix so that the phases can be identified and the relative amounts can be quantified using x-ray diffraction. X-ray diffraction samples a much larger volume of material than does TEM so that the quantification of phases becomes simpler and has less uncertainty.

4.1.4 Micrographs Showing Precipitation in Alloy 22 Beginning On and Covering Grain Boundaries, Beginning on Twin Boundaries, and Beginning Within the Grains (TBV-1254)

This section contains optical and scanning electron microscopy (SEM) images (Figures 4-37 through 4-60) used to determine the time at which the various stages of intermetallic and carbide precipitation occur in Alloy 22 base metal after aging in the temperature range of 600 to 800°C. No distinction has been made between the various intermetallics and the carbides that form in Alloy 22. The intermetallic phases (μ , P, and sigma) are virtually indistinguishable in the SEM, and there is relatively little carbide precipitation.

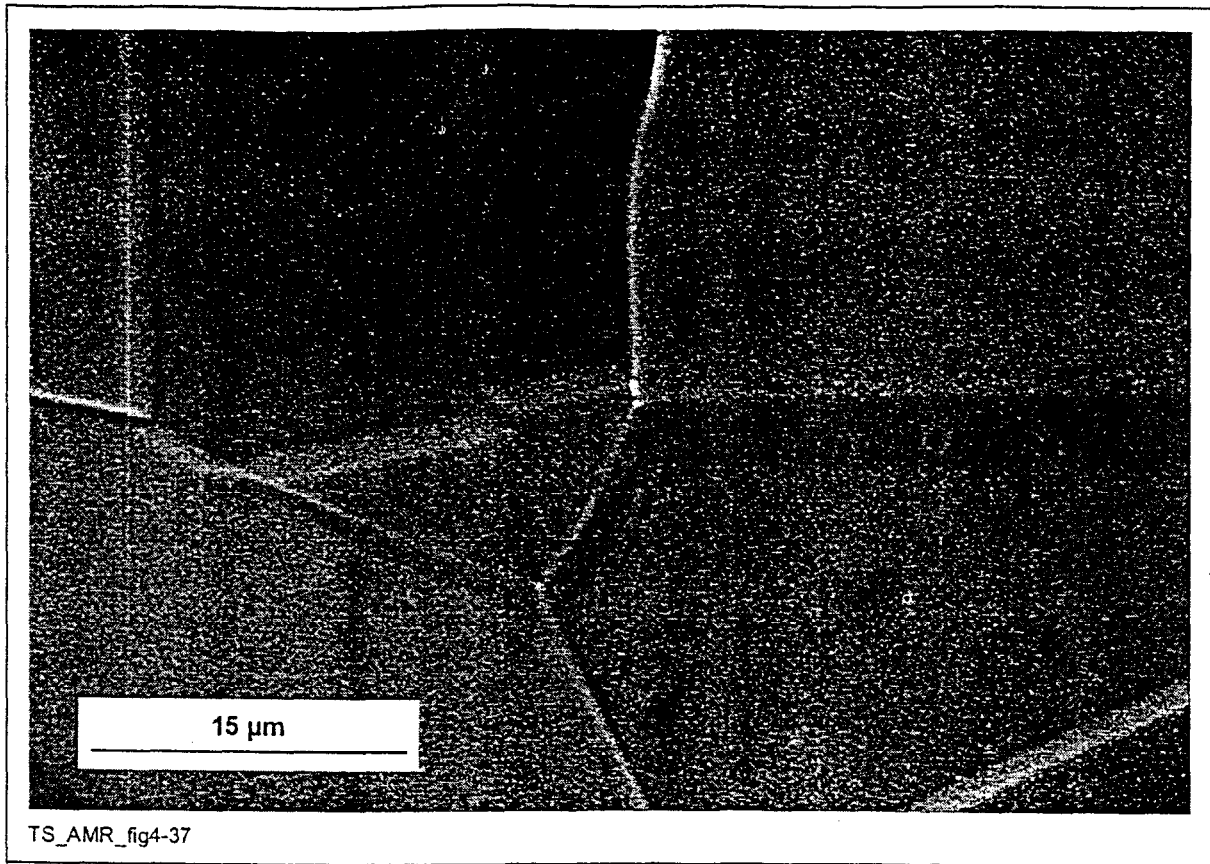


Figure 4-37. SEM Micrograph Showing Precipitation Just Beginning on Grain Boundaries After Aging Alloy 22 for 10 hr at 593°C

(TS393-028a, 2/15/99, SN #434 p.7)

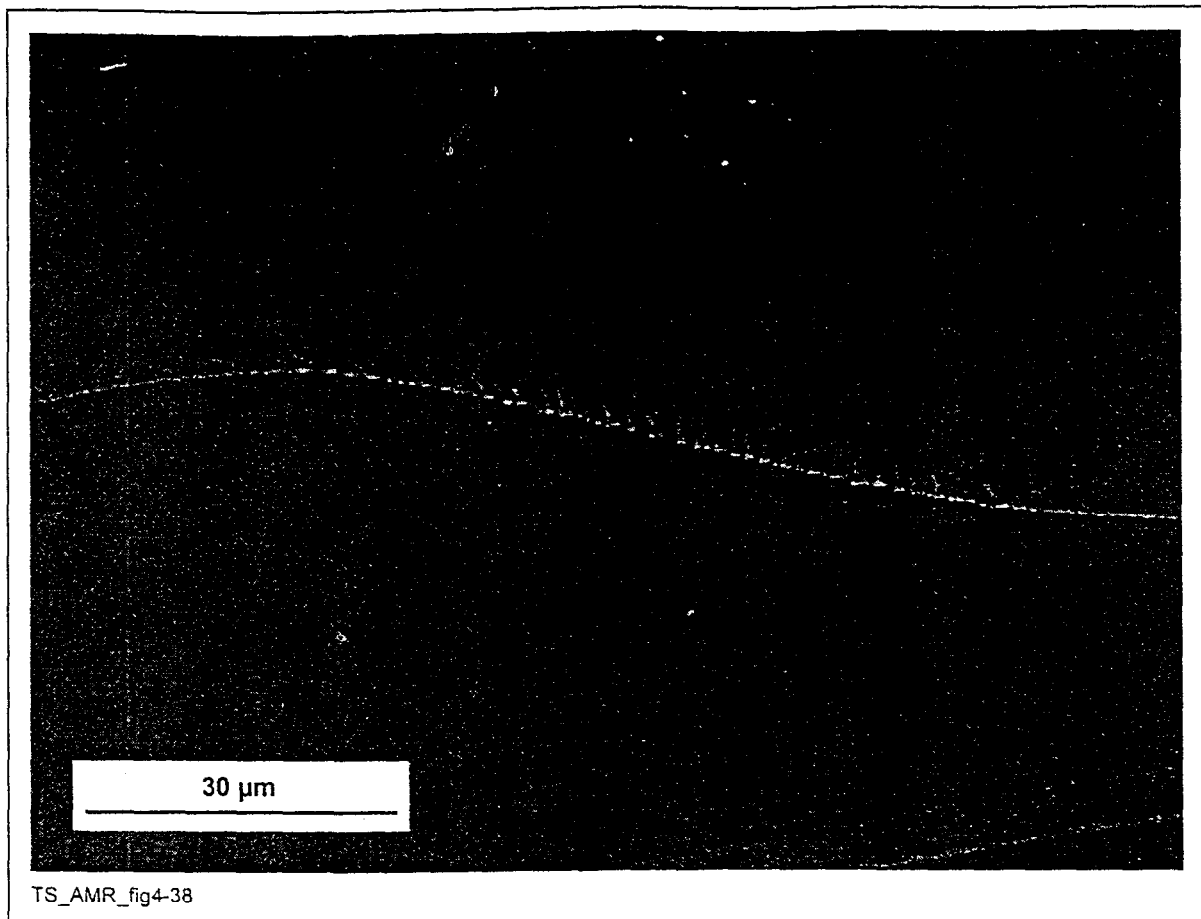


Figure 4-38. SEM Micrograph Showing Precipitation on Grain Boundaries After Aging Alloy 22 for 100 hr at 593°C

(TS393-029a, 2/15/99, SN #434 p.8)



Figure 4-39. Optical Micrograph Showing No Precipitation on Grain Boundaries After Aging Alloy 22 for 1 hr at 649°C

(TS393-008a, 12/7/98, SN #434 p.10)

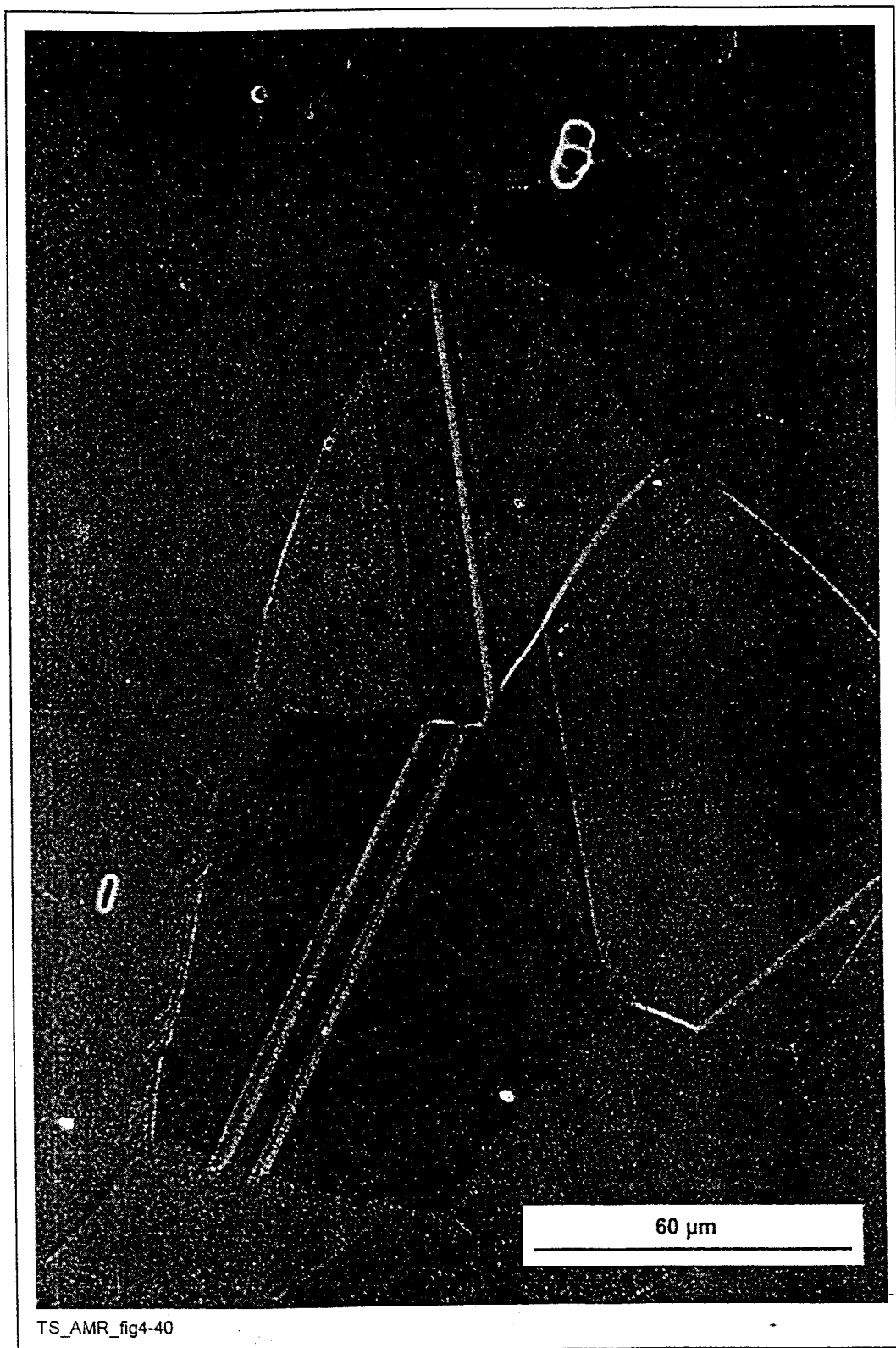


Figure 4-40. SEM Micrograph Showing Little or No Precipitation on Grain Boundaries After Aging Alloy 22 for 1 hr at 649°C

(TS393-008a, 12/7/98, SN #434 p.10)

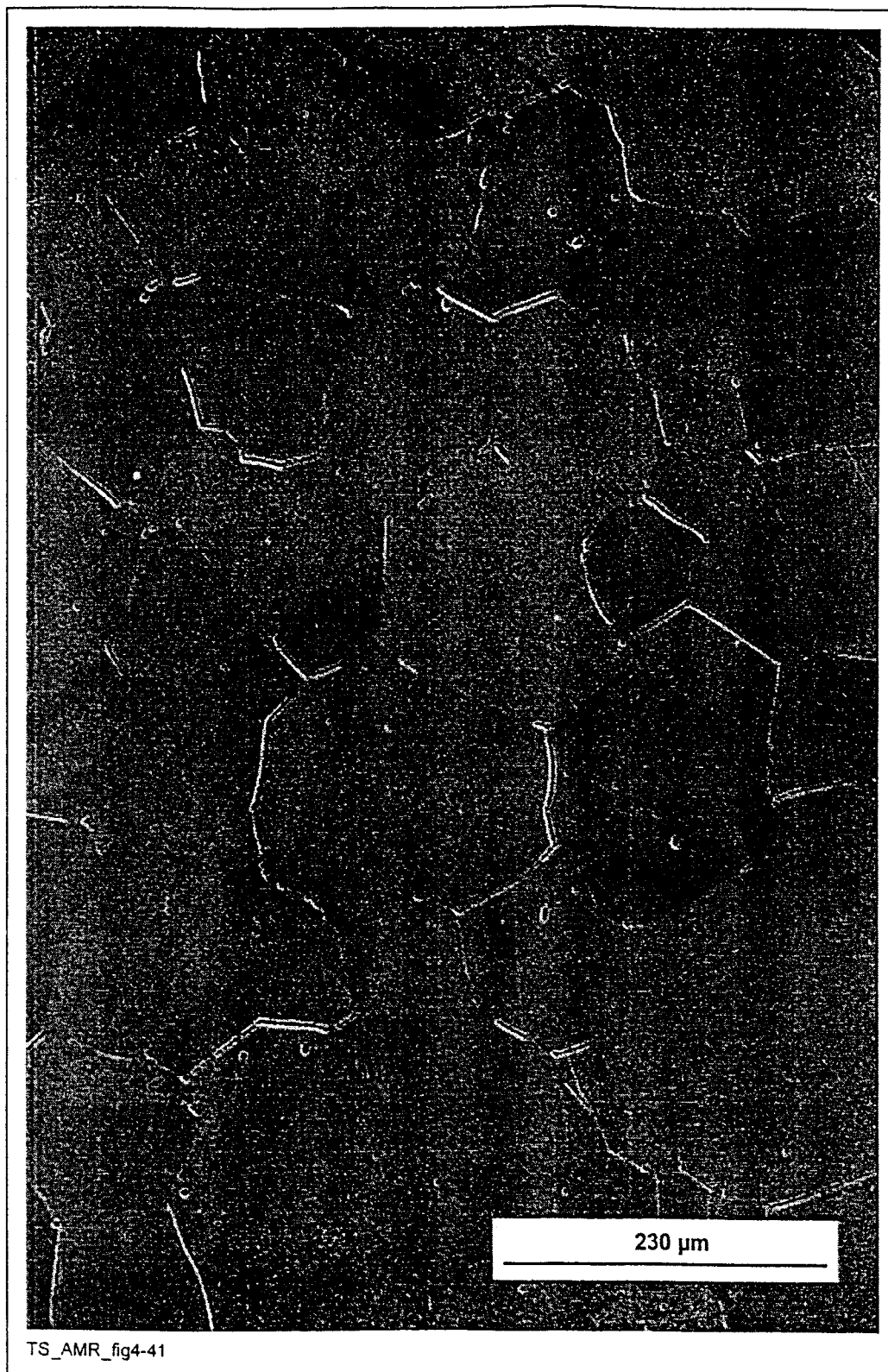


Figure 4-41. SEM Micrograph Showing Precipitation on Grain Boundaries After Aging Alloy 22 for 10 hr at 649°C

(TS393-009a, 12/7/98, SN #434 p.11)

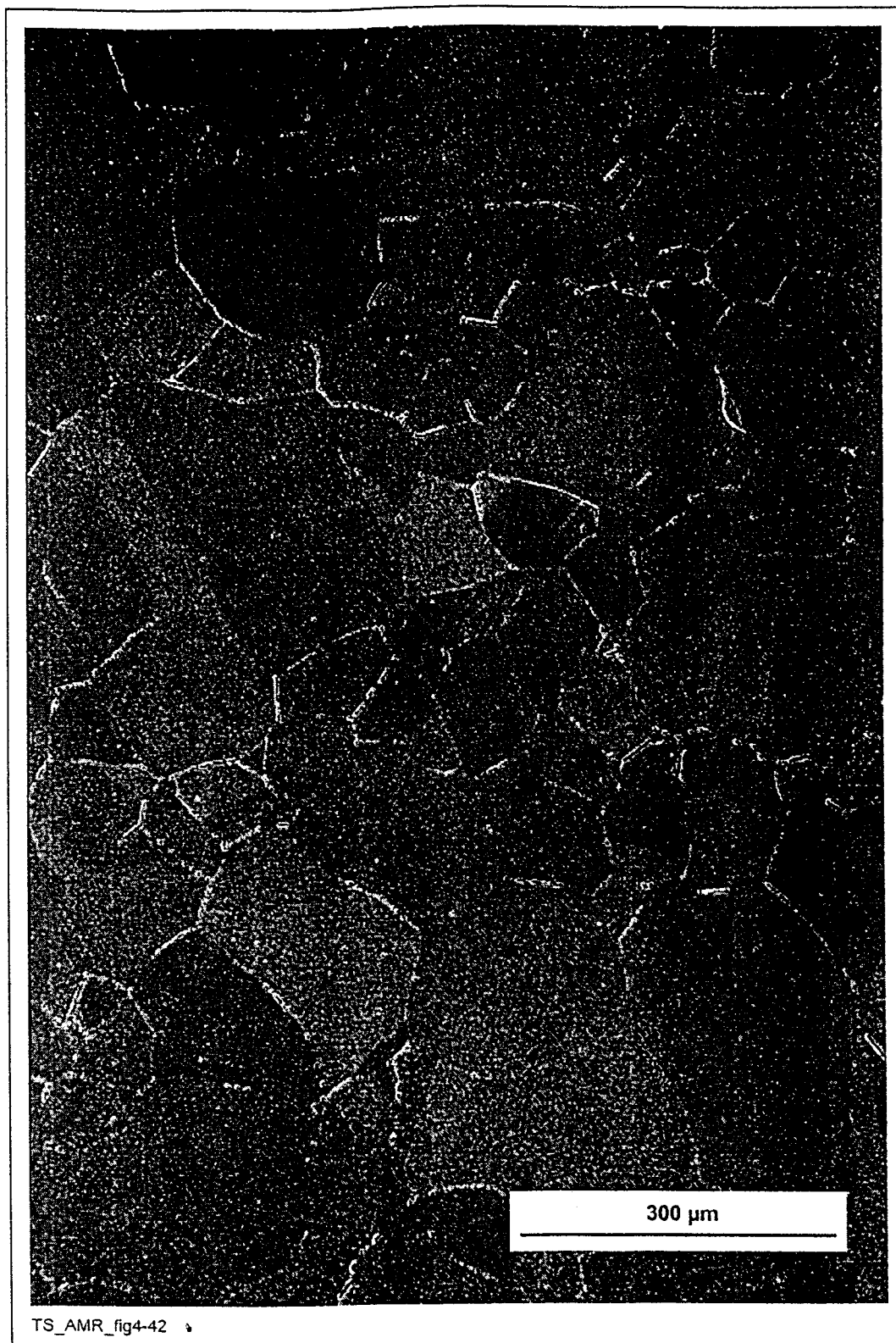


Figure 4-42. SEM Micrograph Showing Precipitation on Grain Boundaries After Aging Alloy 22 for 100 hr at 649°C

(TS393-010a, 12/7/98, SN #434 p.12)

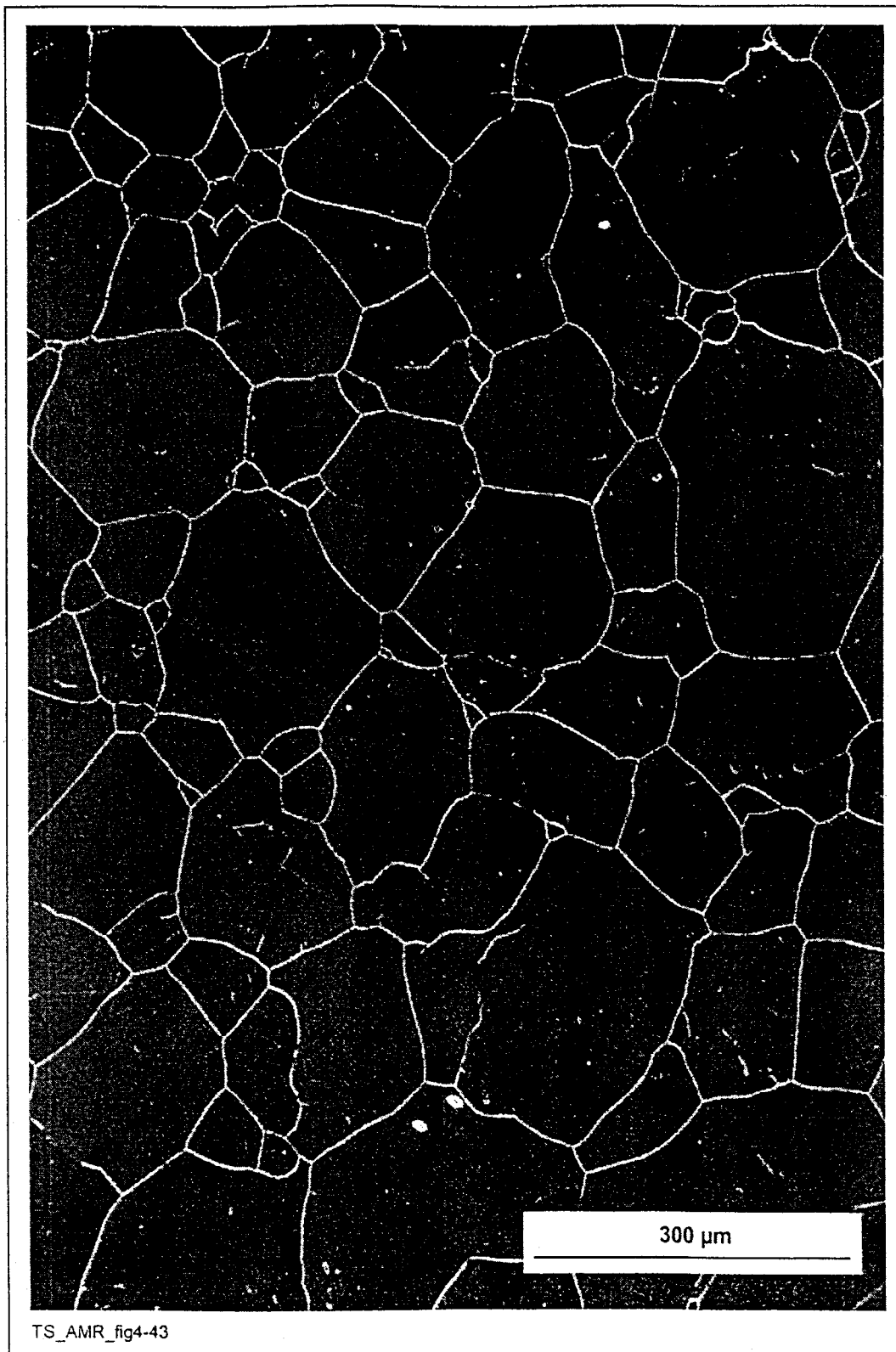


Figure 4-43. SEM Micrograph Showing Precipitation on Grain Boundaries After Aging Alloy 22 for 1000 hr at 649°C

(TS393-011a, 12/7/98, SN #434 p.12)

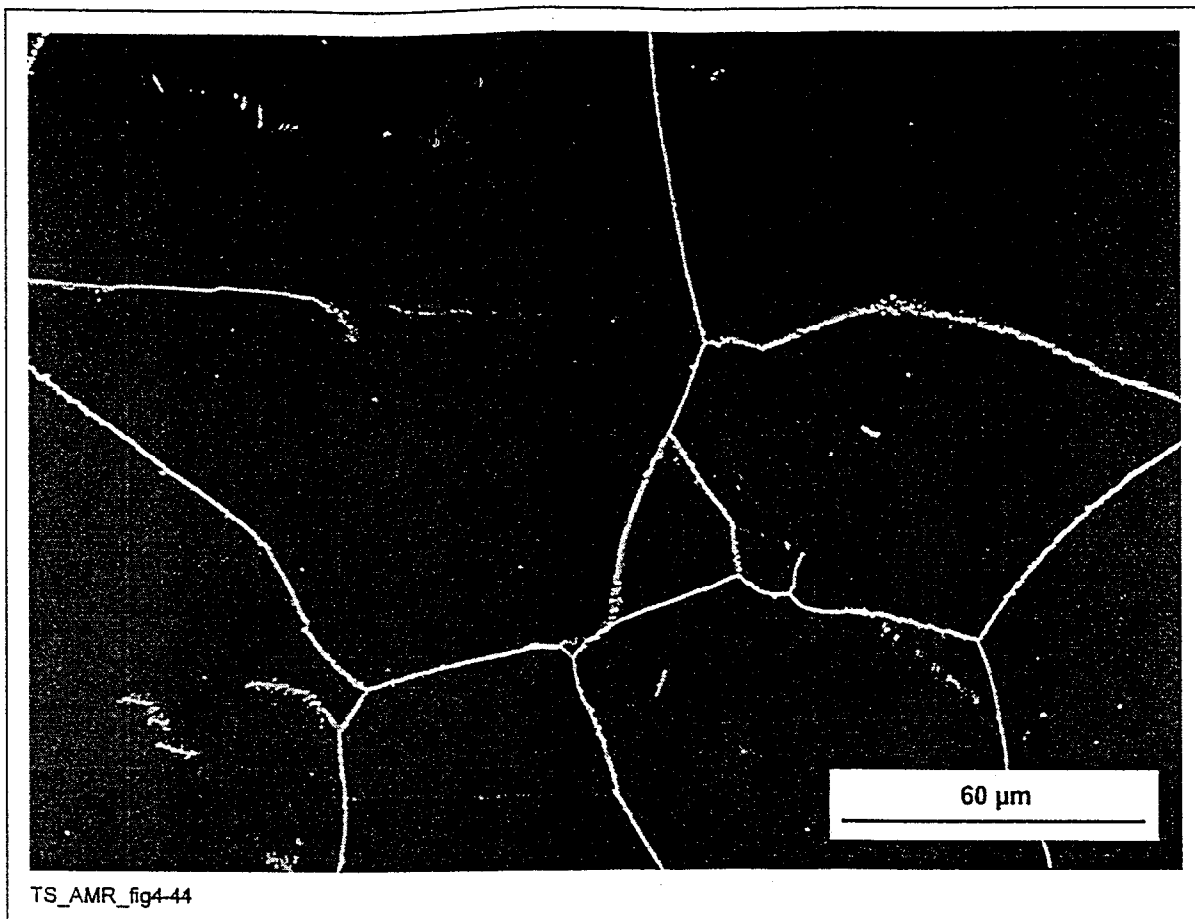


Figure 4-44. SEM Micrograph Showing Precipitation on Grain and on Twin Boundaries After Aging Alloy 22 for 1000 hr at 649°C

(TS393-011a, 12/7/98, SN #434 p.13)

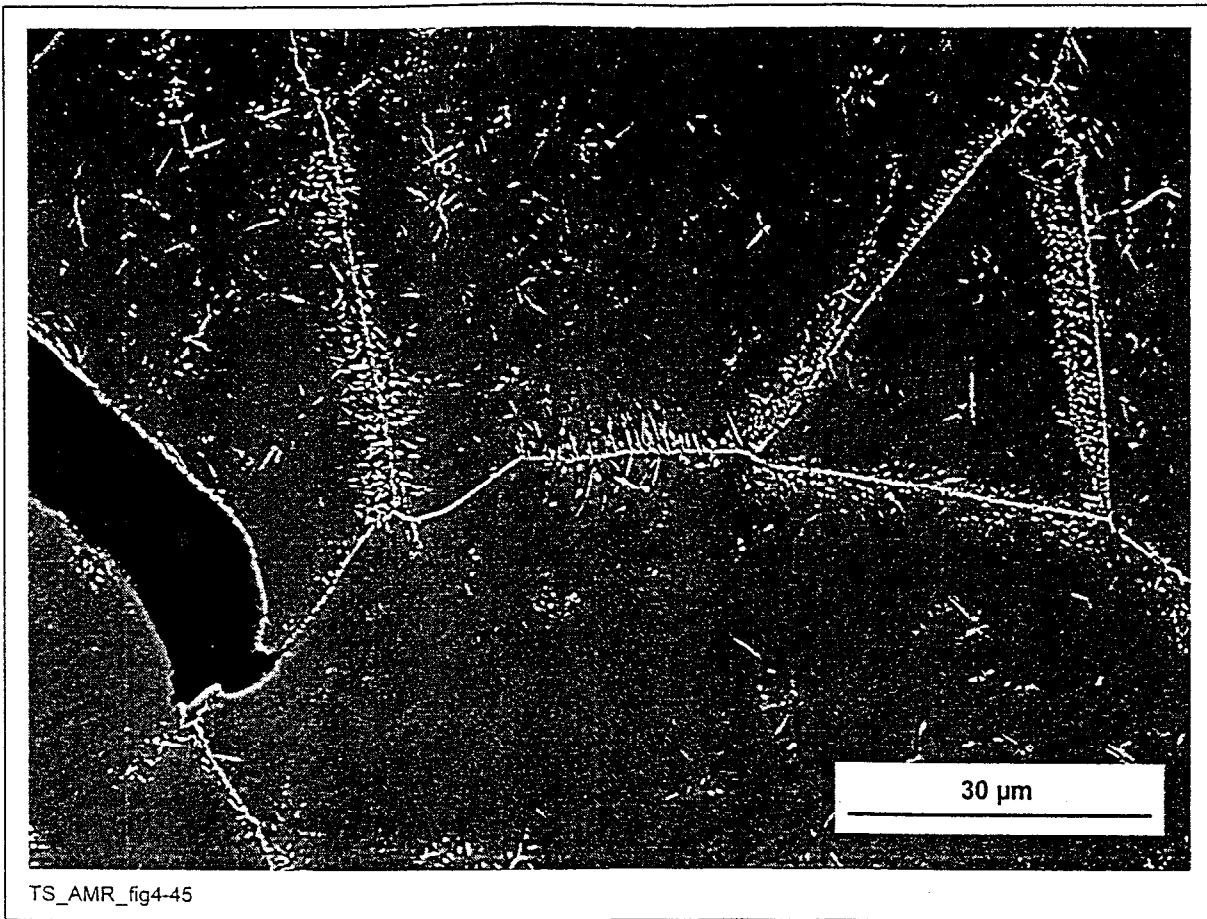


Figure 4-45. SEM Micrograph Showing Precipitation on Grain Boundaries and Within the Grains After Aging Alloy 22 for 16,000 hr at 649°C

(TS369-008b, 8/28/98, SN #434 p.14)

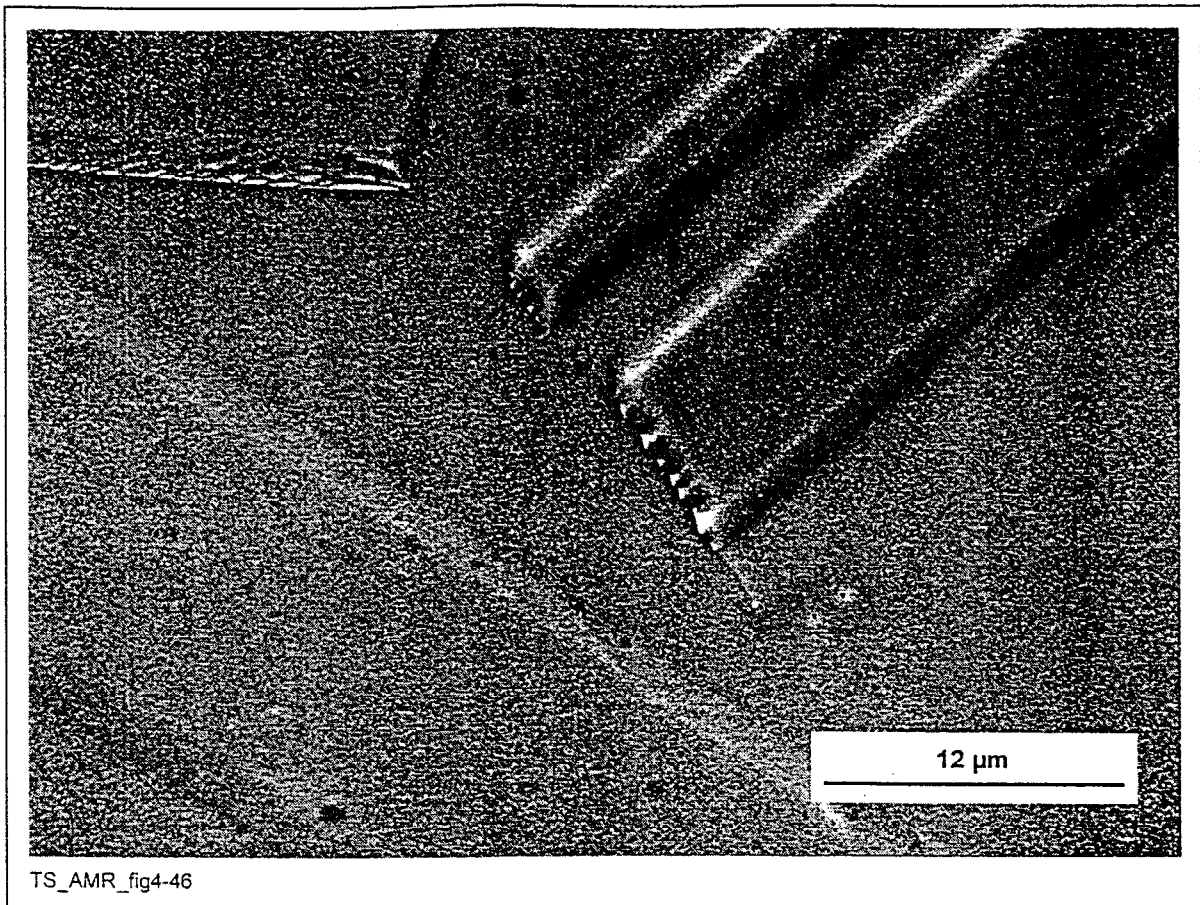


Figure 4-46. SEM Micrograph Showing Precipitation that Occurs at a Limited Number of Sites on Grain Boundaries in Alloy 22 After Aging for 1 hr at 704°C

(TS393-012a, 12/7/98, SN #434 p.15)

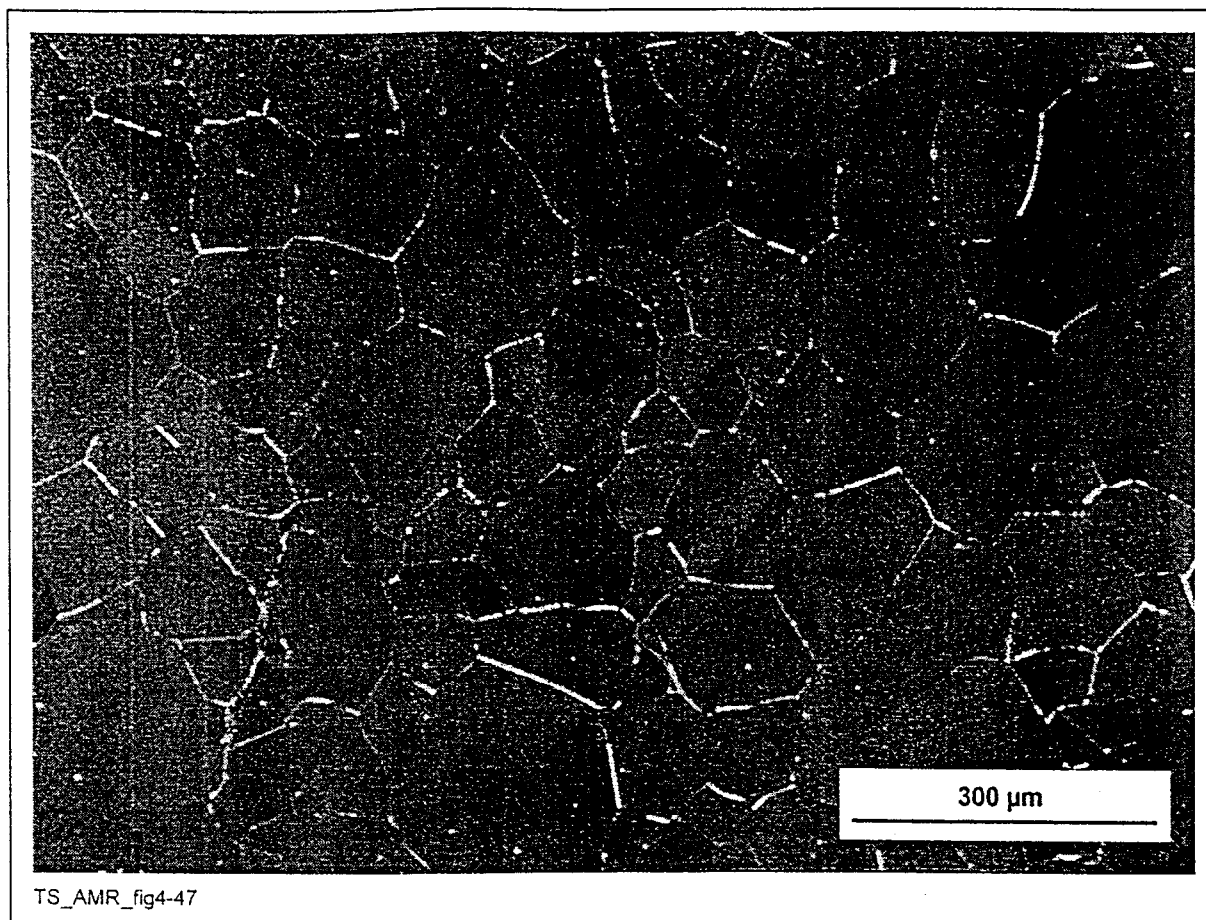


Figure 4-47. SEM Micrograph Showing Precipitation on Grain Boundaries After Aging Alloy 22 for 10 hr at 704°C

(TS393-013a, 12/7/98, SN #434 p.15)

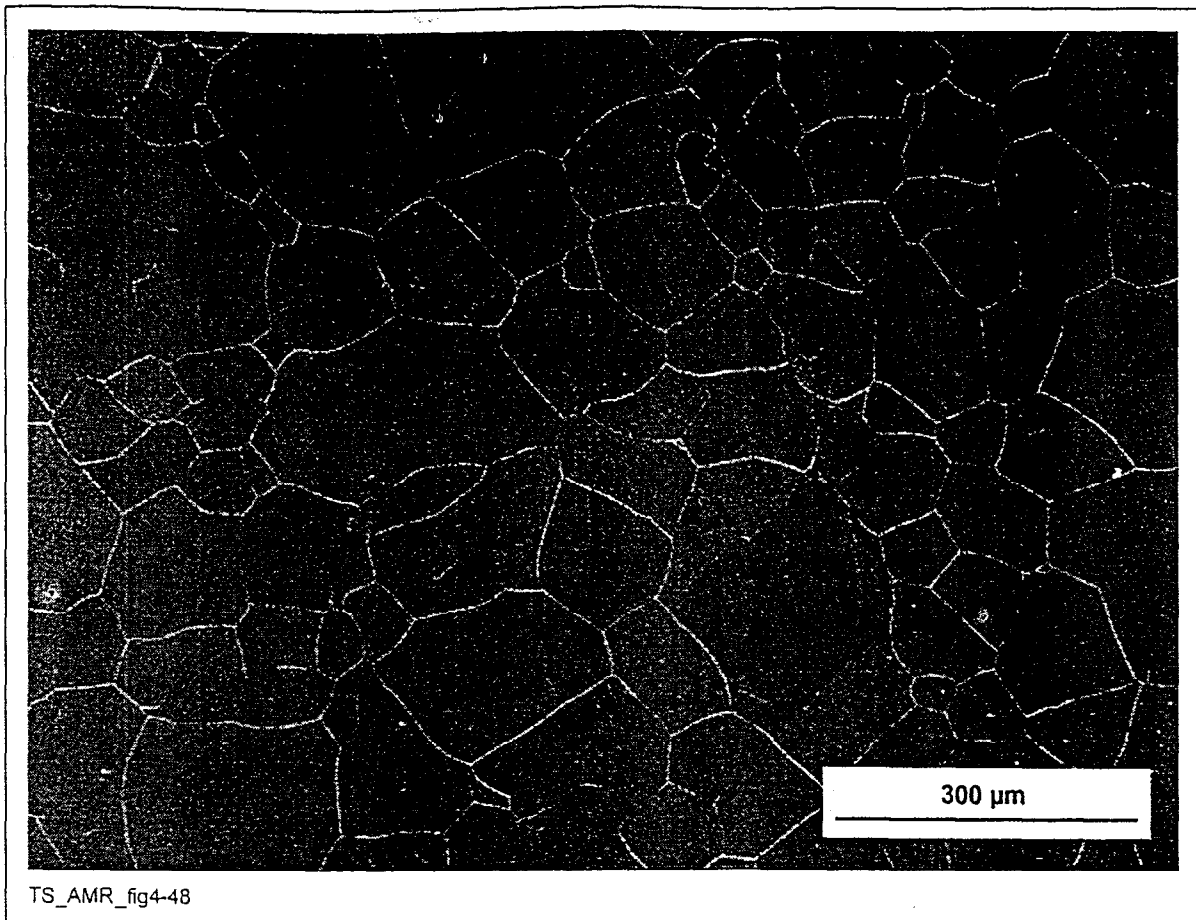


Figure 4-48. SEM Micrograph Showing Significant Grain Boundary Precipitation After Aging Alloy 22 for 100 hr at 704°C

(TS393-014a, 12/7/98, SN #434 p.16)

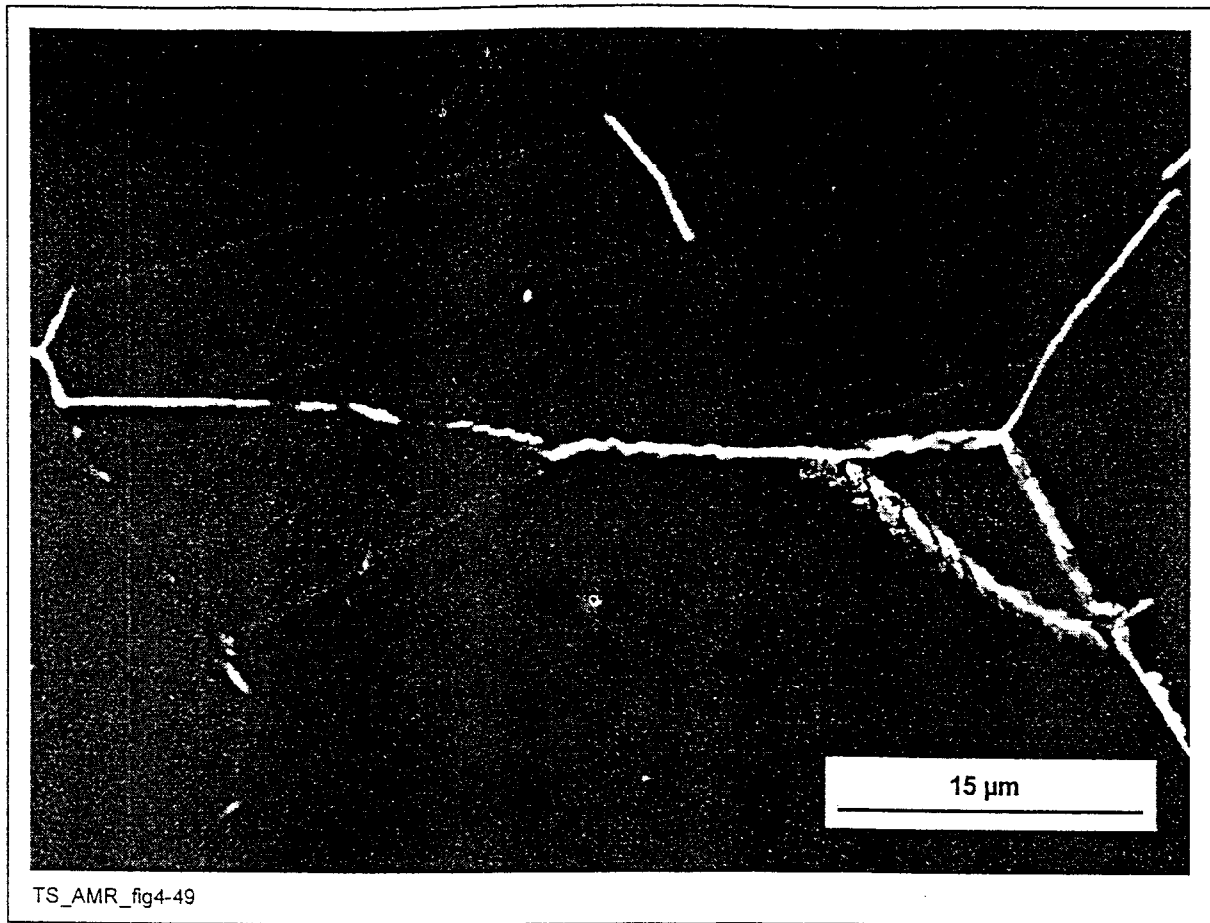


Figure 4-49. SEM Micrograph Showing Precipitation Just Beginning on Twin Boundaries After Aging Alloy 22 for 100 us at 704°C

(TS393-014a, 12/7/98, SN #434 p.17)

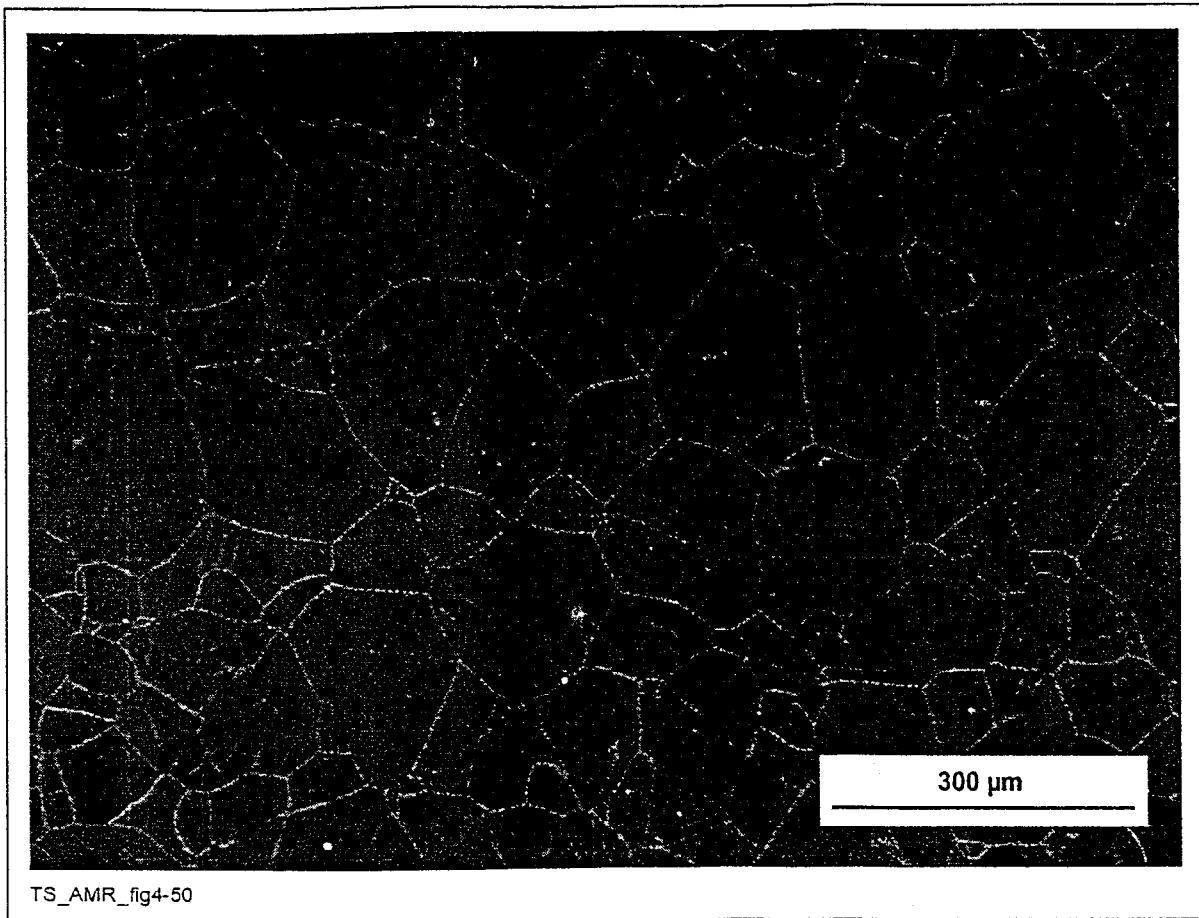


Figure 4-50. SEM Micrograph Showing Complete Grain Boundary Coverage by Precipitation and Precipitation on Twin Boundaries After Aging Alloy 22 for 1000 hr at 704°C

(TS393-015a, 12/7/98, SN #434 p.17)

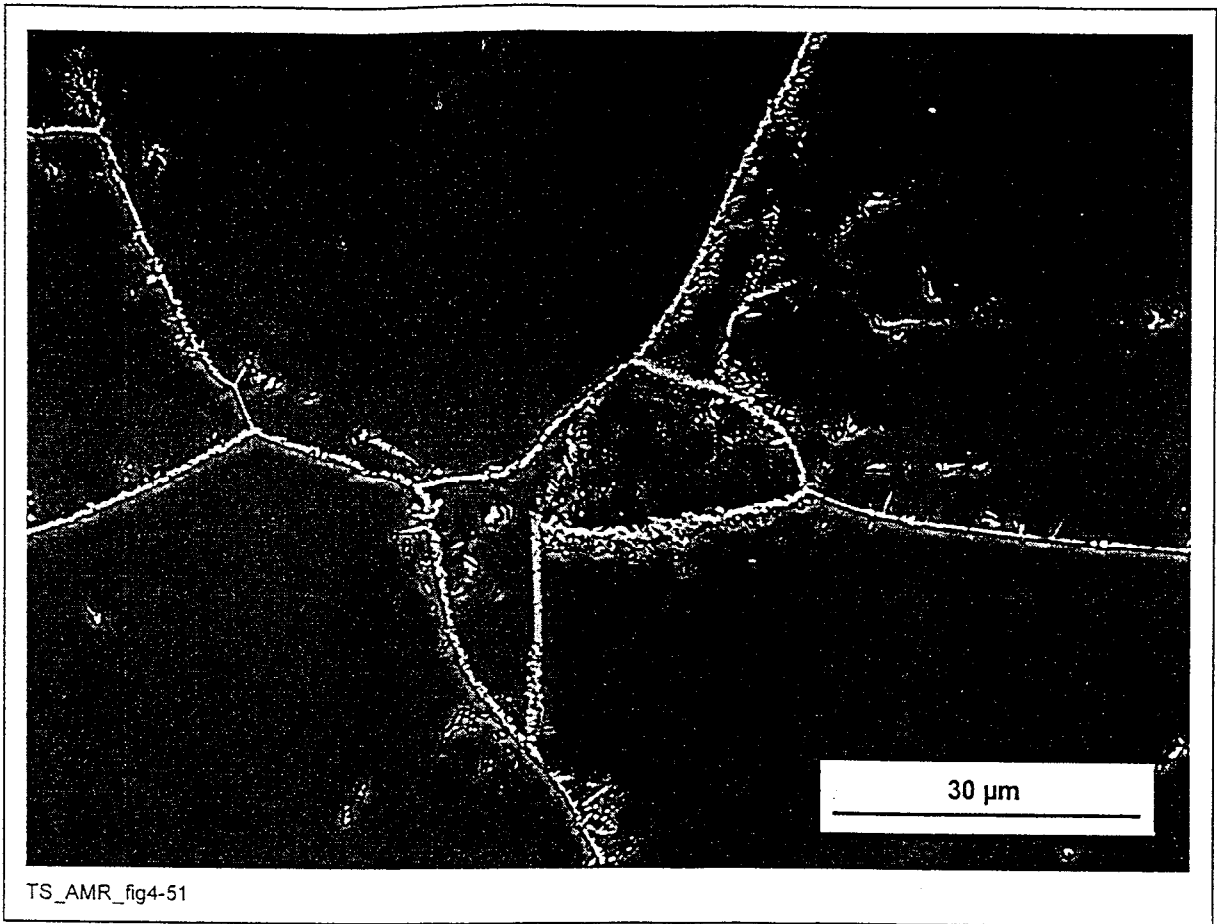


Figure 4-51. SEM Micrograph Showing Precipitation Beginning Within the Grains After Aging Alloy 22 for 1000 hr at 704°C

(TS393-015a, 12/7/98, SN #434 p.18)

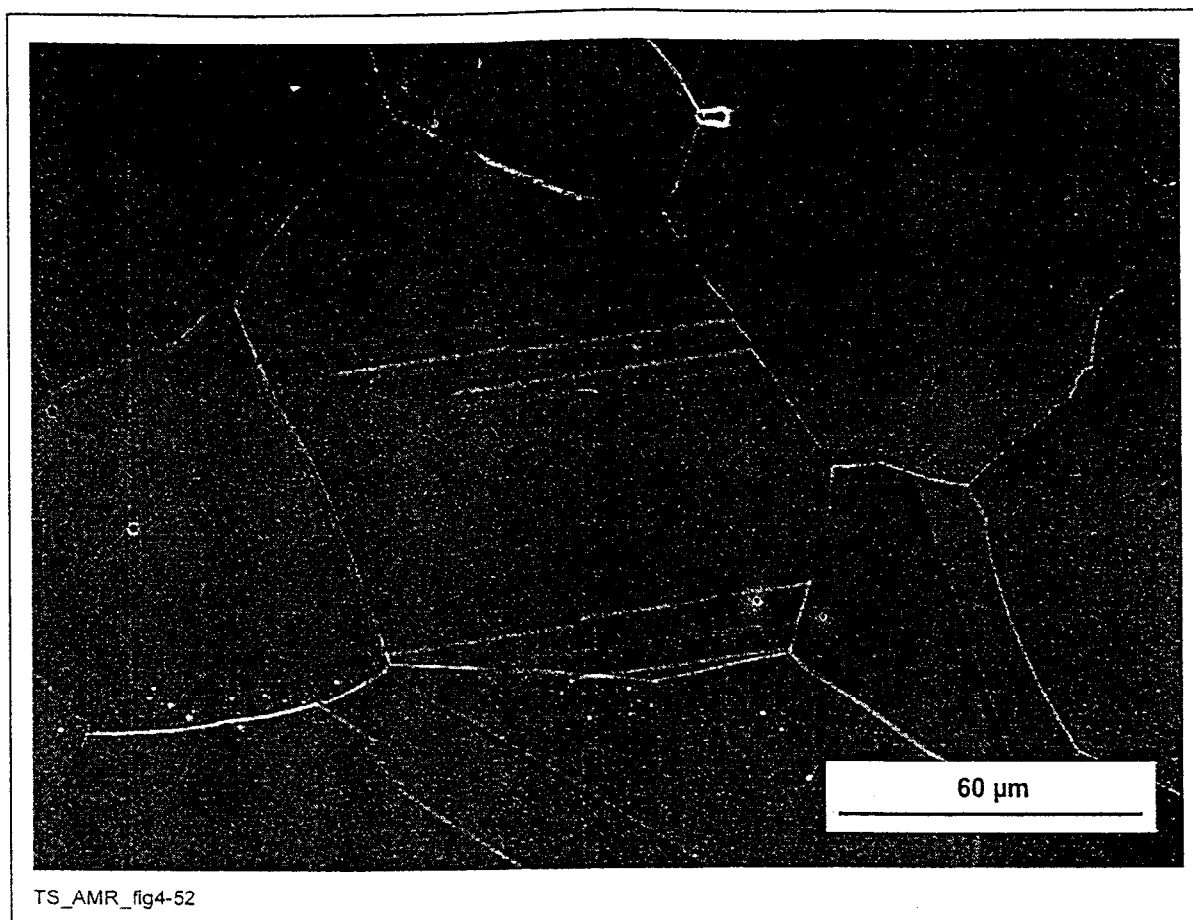


Figure 4-52. SEM Micrograph Showing that Grain Boundary Precipitation Has Begun After Aging Alloy 22 for 1 hr at 760°C

(TS369-014, 11/30/98, SN #434 p.19)

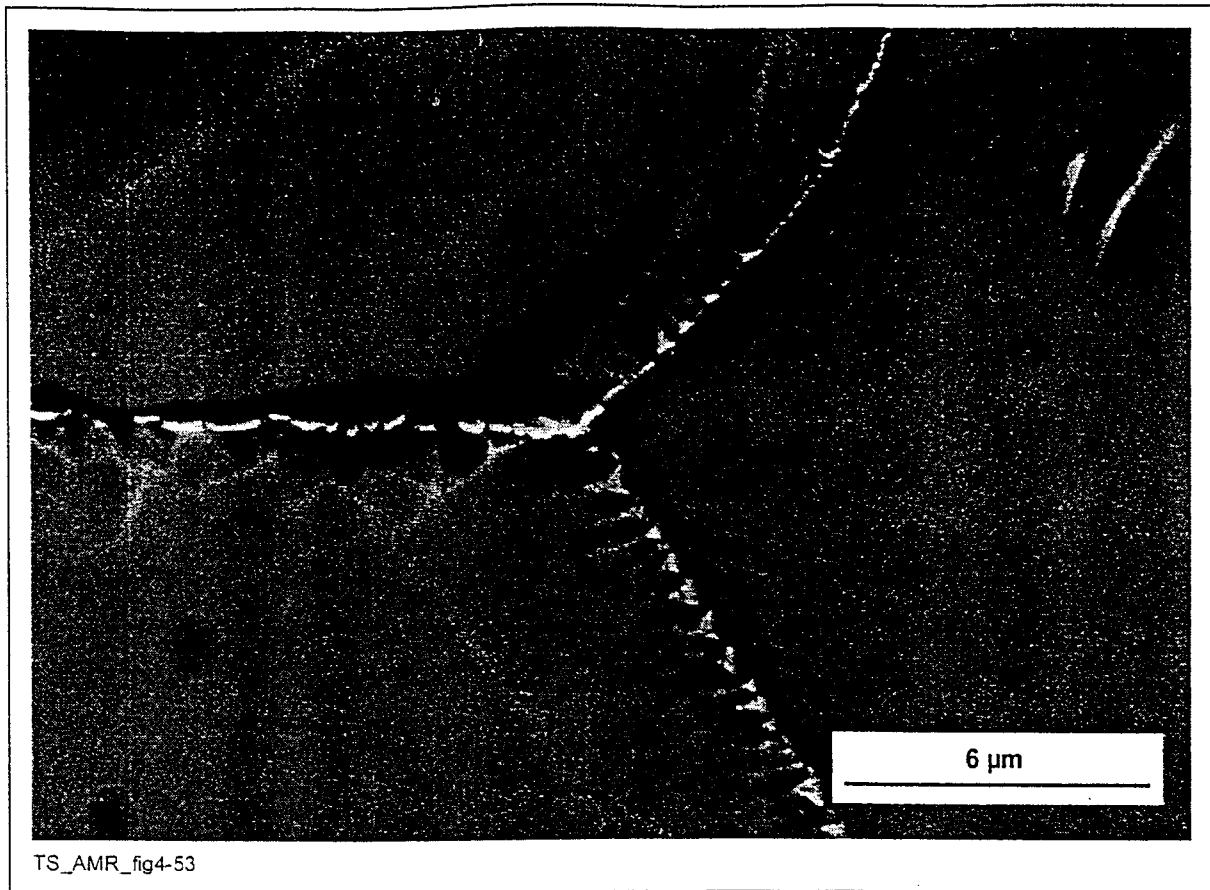


Figure 4-53. SEM Micrograph Showing that Grain Boundary Precipitation Has Begun After Aging Alloy 22 for 1 hr at 760°C

(TS369-014, 11/30/98, SN #434 p.20)

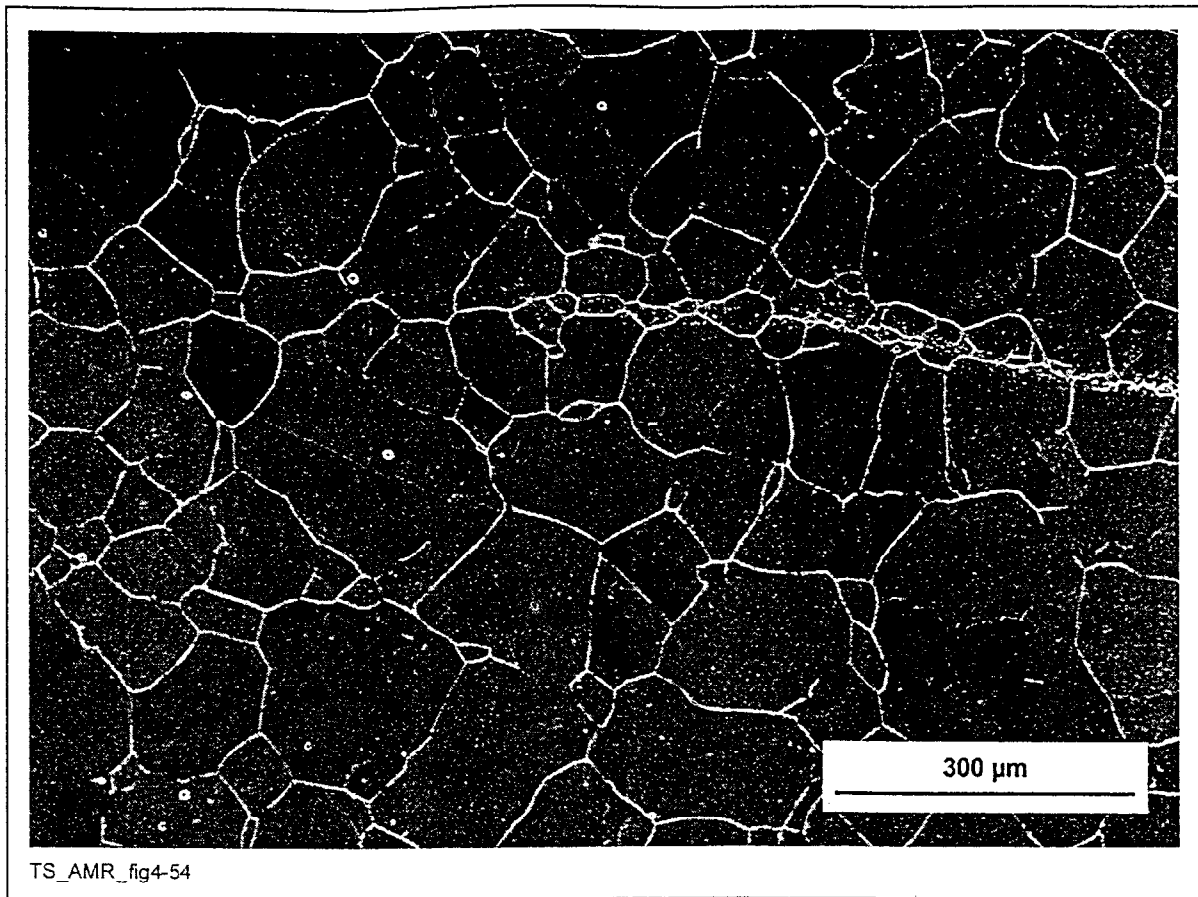


Figure 4-54. SEM Micrograph Showing Significant Grain Boundary Precipitation After Aging Alloy 22 for 10 hr at 760°C

(TS369-015, 11/30/98, SN #434 p.21)

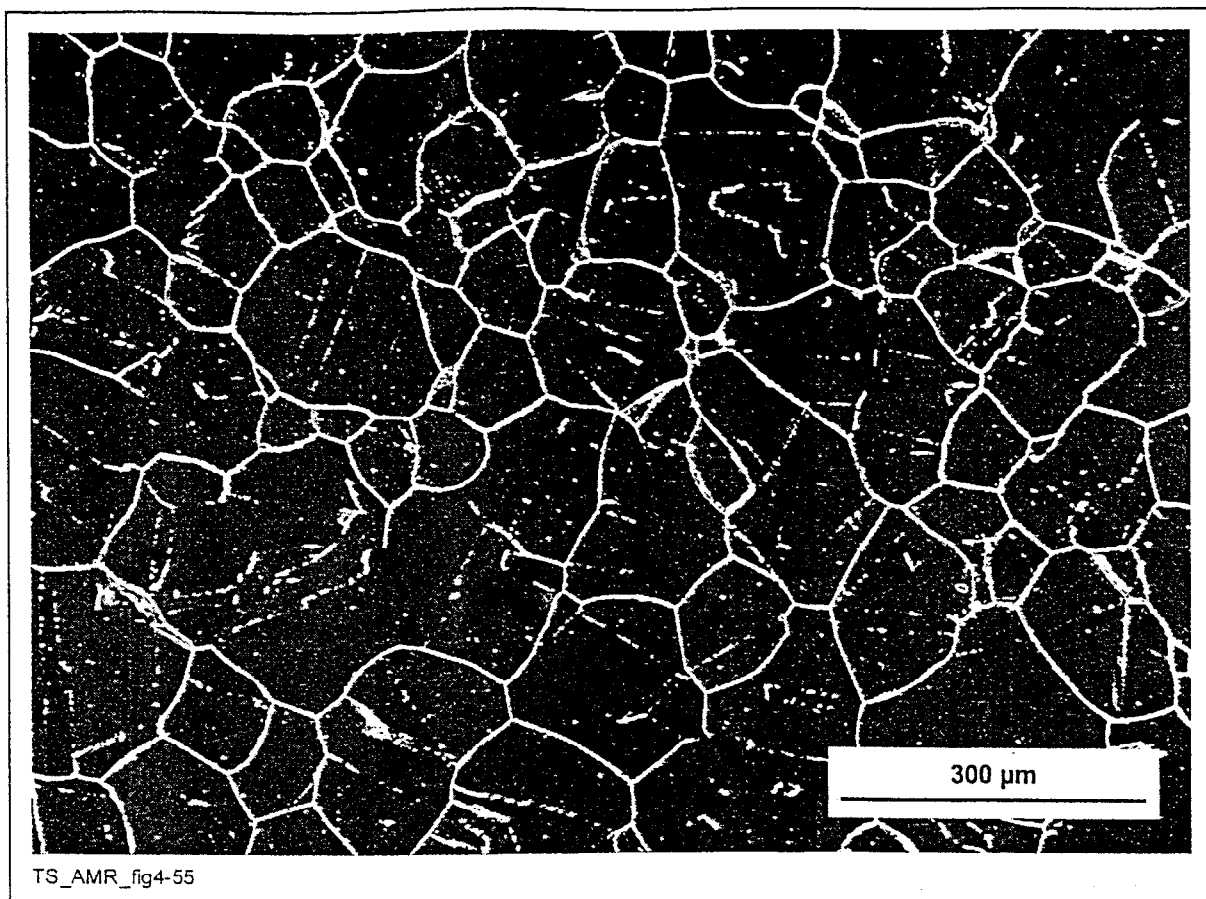


Figure 4-55. SEM Micrograph Showing Significant Grain Boundary Precipitation and Precipitation on Twin Boundaries After Aging Alloy 22 for 119 hr at 760°C

(TS369-016, 11/30/98, SN #434 p.22)

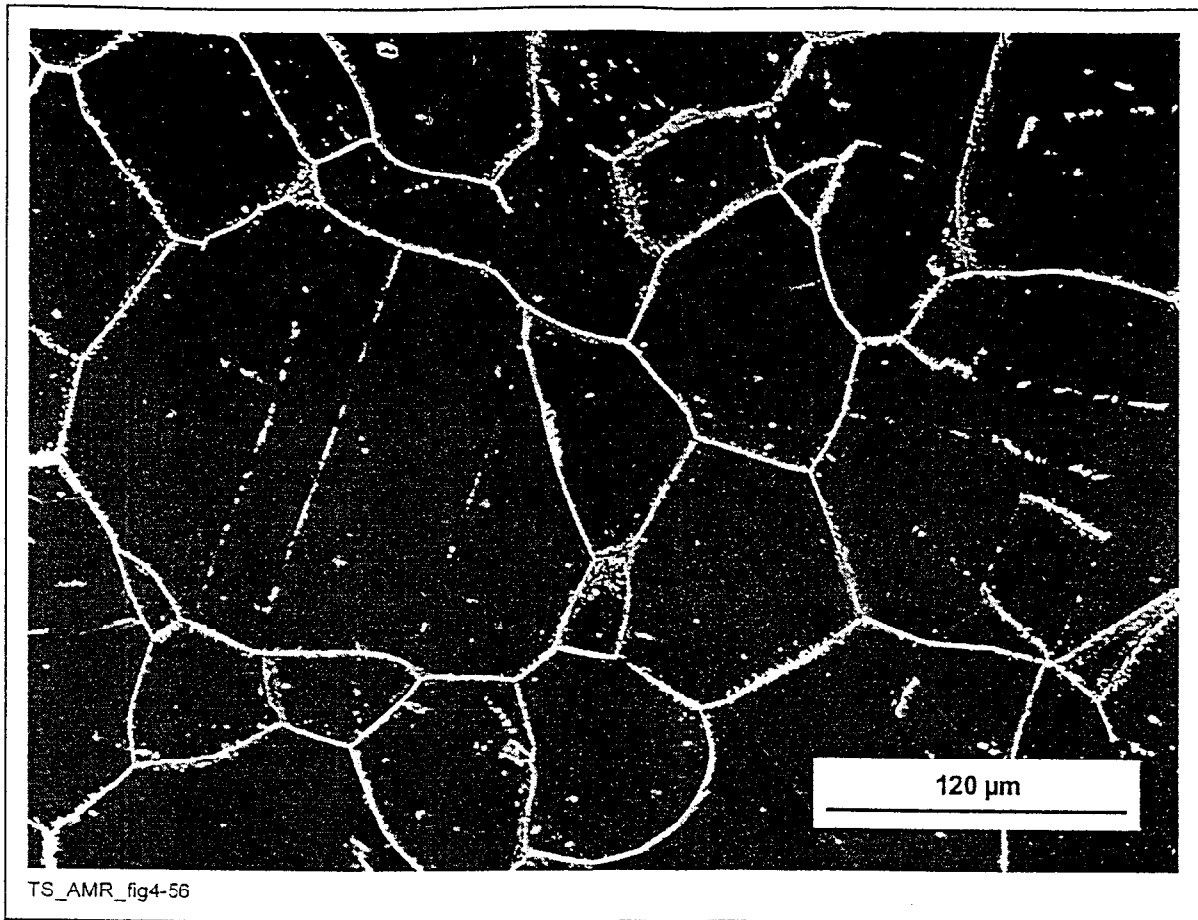


Figure 4-56. SEM Micrograph Showing Precipitation on Grain Boundaries, on Twin Boundaries, and Within the Grains After Aging Alloy 22 for 119 hr at 760°C

(TS369-016, 11/30/98, SN #434 p.24)

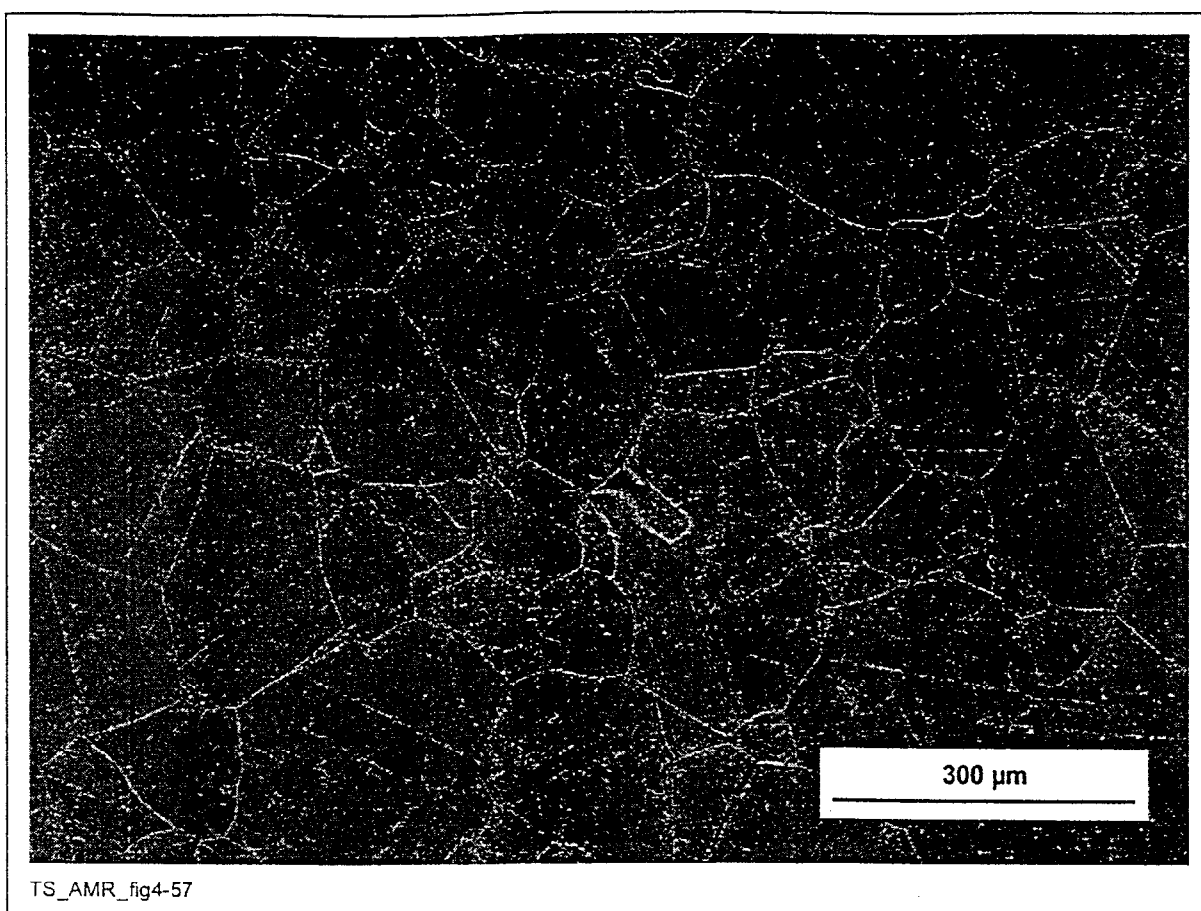


Figure 4-57. SEM Micrograph Showing Significant Precipitation Within the Grains of Alloy 22 After Aging for 1000 hr at 760°C

(TS393-007a, 12/7/98, SN #434 p.22)

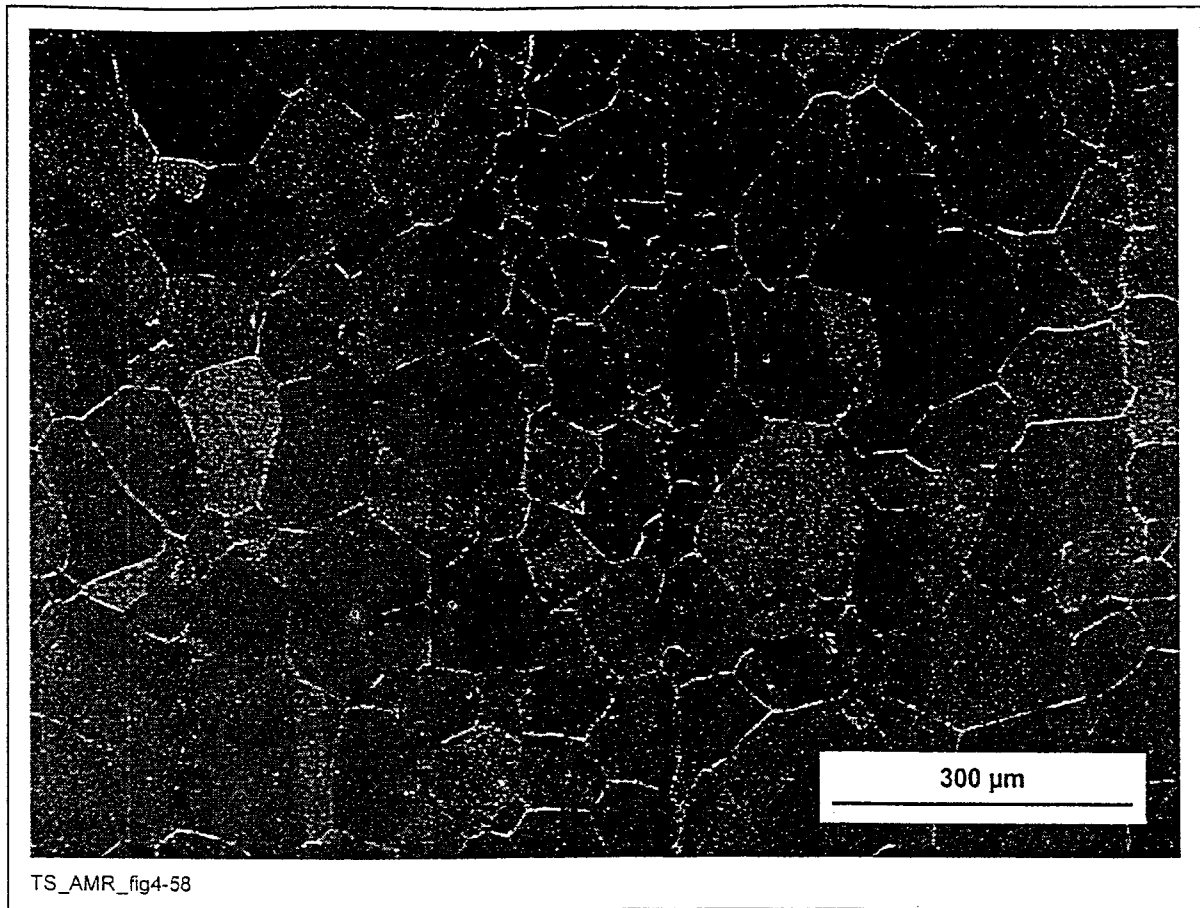


Figure 4-58. SEM Micrograph Showing Grain Boundary Precipitation in Alloy 22 After Aging for 1 hr at 800°C

(TS393-020a, 2/15/99, SN #434 p.25)

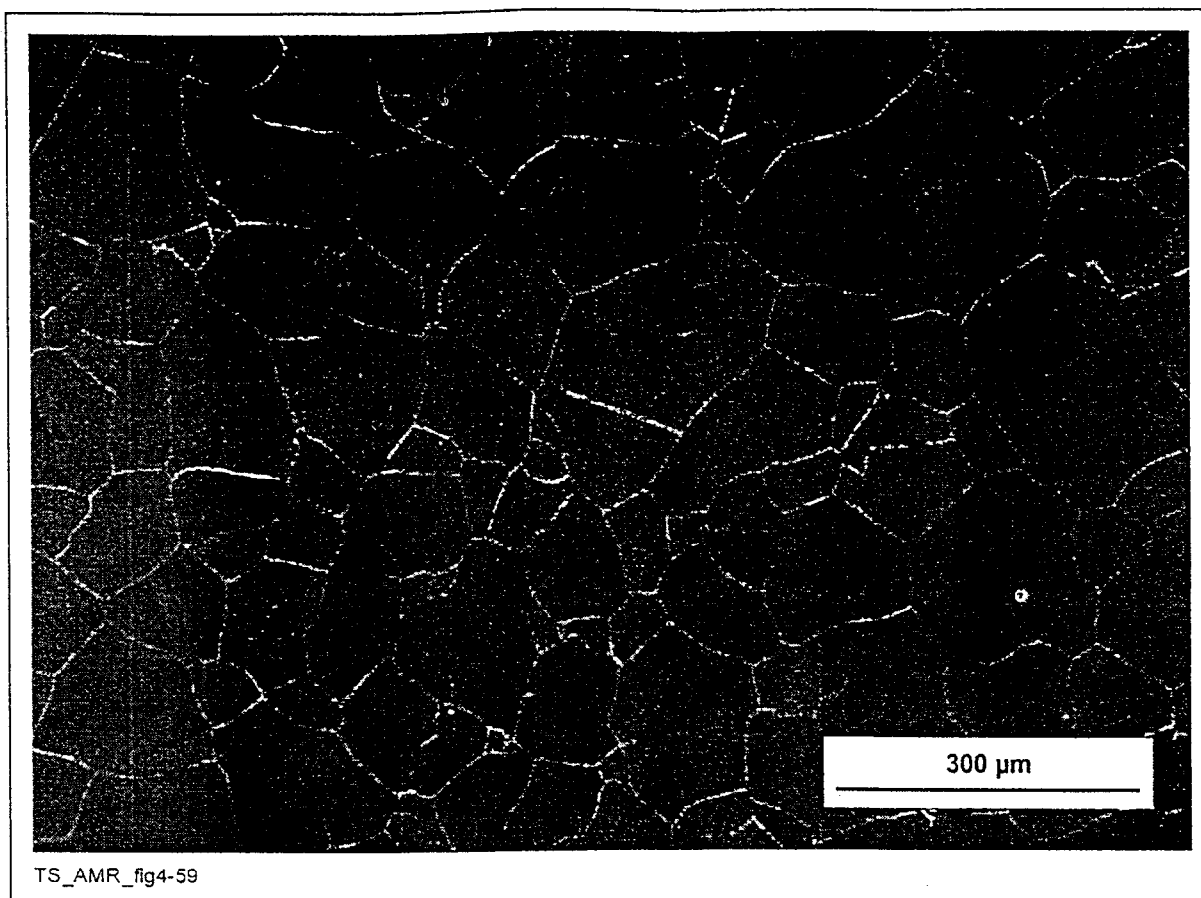


Figure 4-59. SEM Micrograph Showing Significant Grain Boundary Precipitation in Alloy 22 After Aging for 10 hr at 800°C

(TS393-021a, 2/15/99, SN #434 p.26)

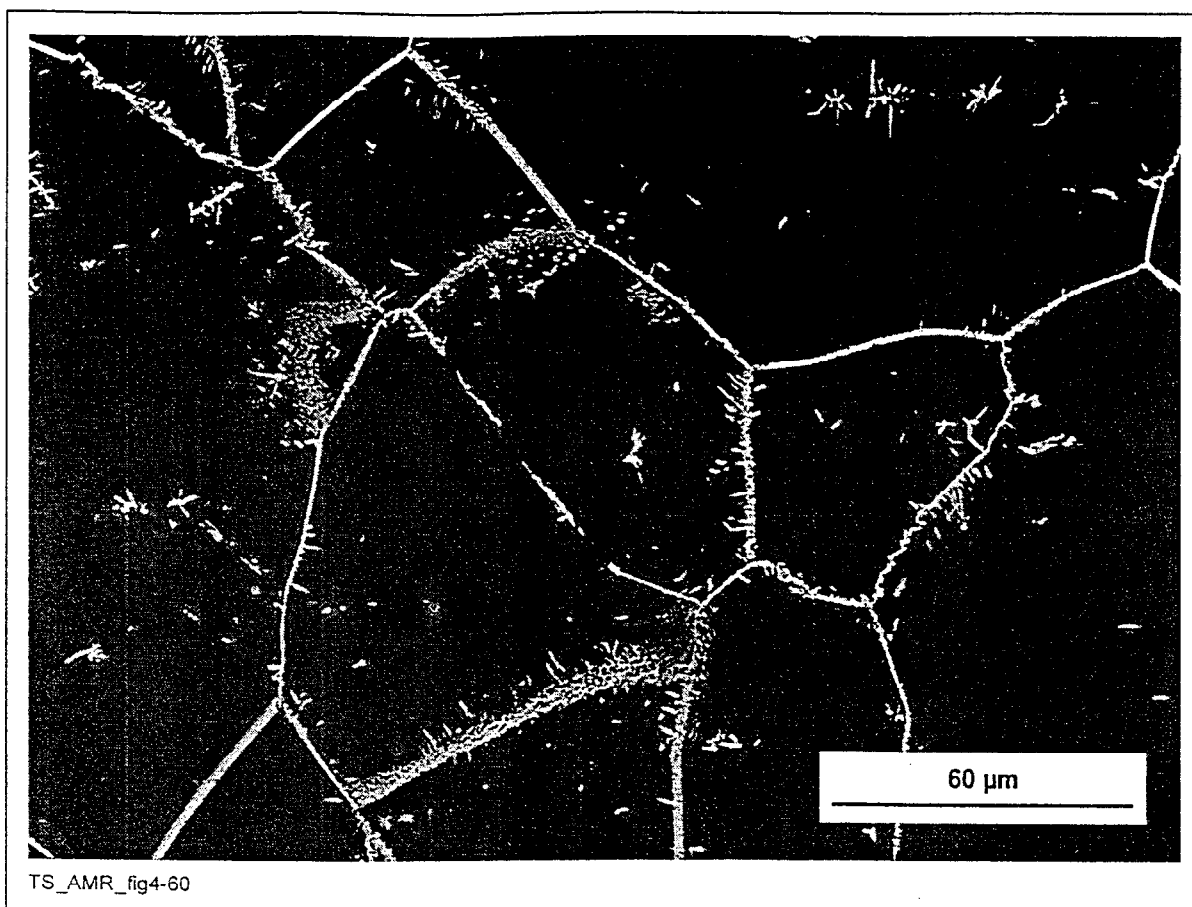


Figure 4-60. SEM Micrograph Showing Precipitation on Grain Boundaries, on Twin Boundaries, and Within the Grains After Aging Alloy 22 for 100 hr at 800°C

(TS393-022a, 2/15/99, SN #434 p.27)

4.1.5 Fraction Intermetallic and Carbide Precipitation in Alloy 22 as a Function of Aging Time and Temperature (TBD-425)

The volume fraction of precipitates in the samples imaged in Section 4.1.4 must be determined and fit to nucleation and growth theory such as that presented in Section 6.2. In addition, more samples must be aged and volume fractions measured to decrease the time interval between observations and to decrease the uncertainty in the analysis.

4.1.6 Micrographs Showing Intermetallic Particles in Alloy 22 Welds (TBV-1253)

The intermetallic phases μ , P, and sigma are known to form in Alloy 22 welds (Cieslak et al. 1986 p. 2041, ¶ 2). This subsection (4.1.6) contains optical, SEM, and TEM images (Figures 4-61 to 4-83) in the preliminary characterization of Alloy 22 welds. Two samples have been examined: one was examined in the as-welded condition; the other was aged for 40,000 hr at 427°C. Although the two welds were produced in the same way, the aged sample did not come from the same weld as did the unaged sample. Thus, some variation is expected between the samples, and direct comparisons on the small scale of differences seen between these samples should not be made.

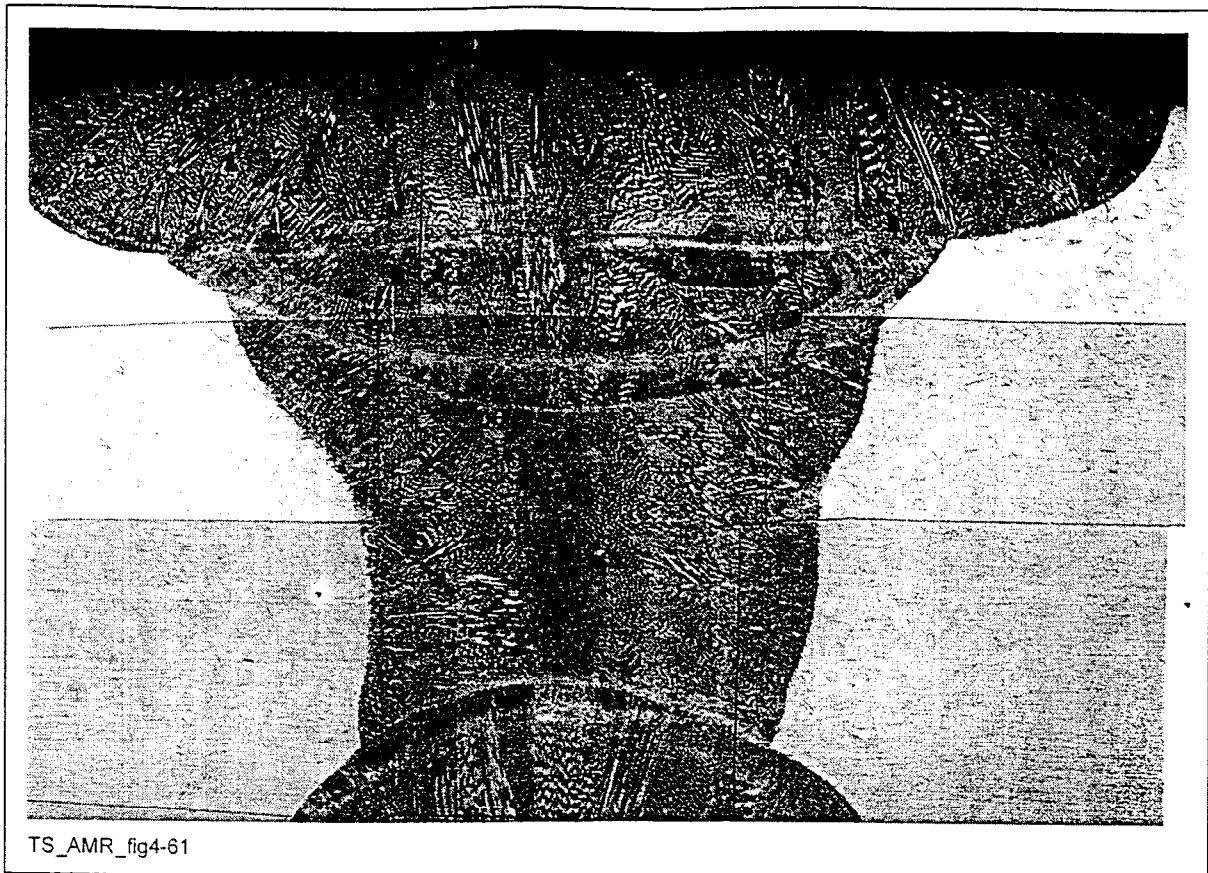


Figure 4-61. Low-Magnification Optical Micrograph of an Alloy 22 Multipass, Double-V Gas-Tungsten-Arc-Welding (GTAW) Weld with Matching Filler Metal

Only approximately three quarters of the half-inch plate is shown. (TS393-019, 8/28/98, SN #393 p.9-10)

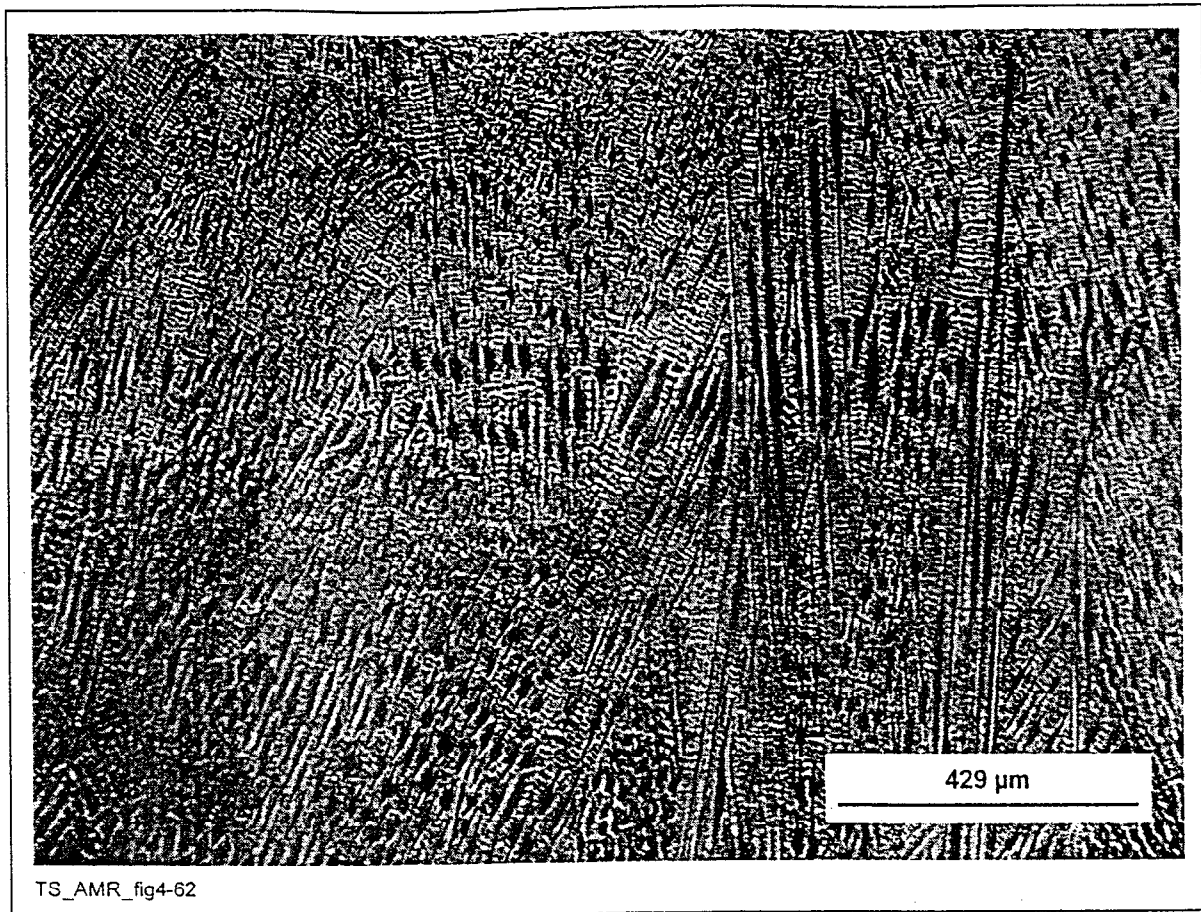


Figure 4-62. SEM Micrograph of the Alloy 22 Weld Shown in Figure 4-58 Showing the Dendritic Structure Typical of Welds

(TS393-019, 8/28/98, SN #393 p.10)

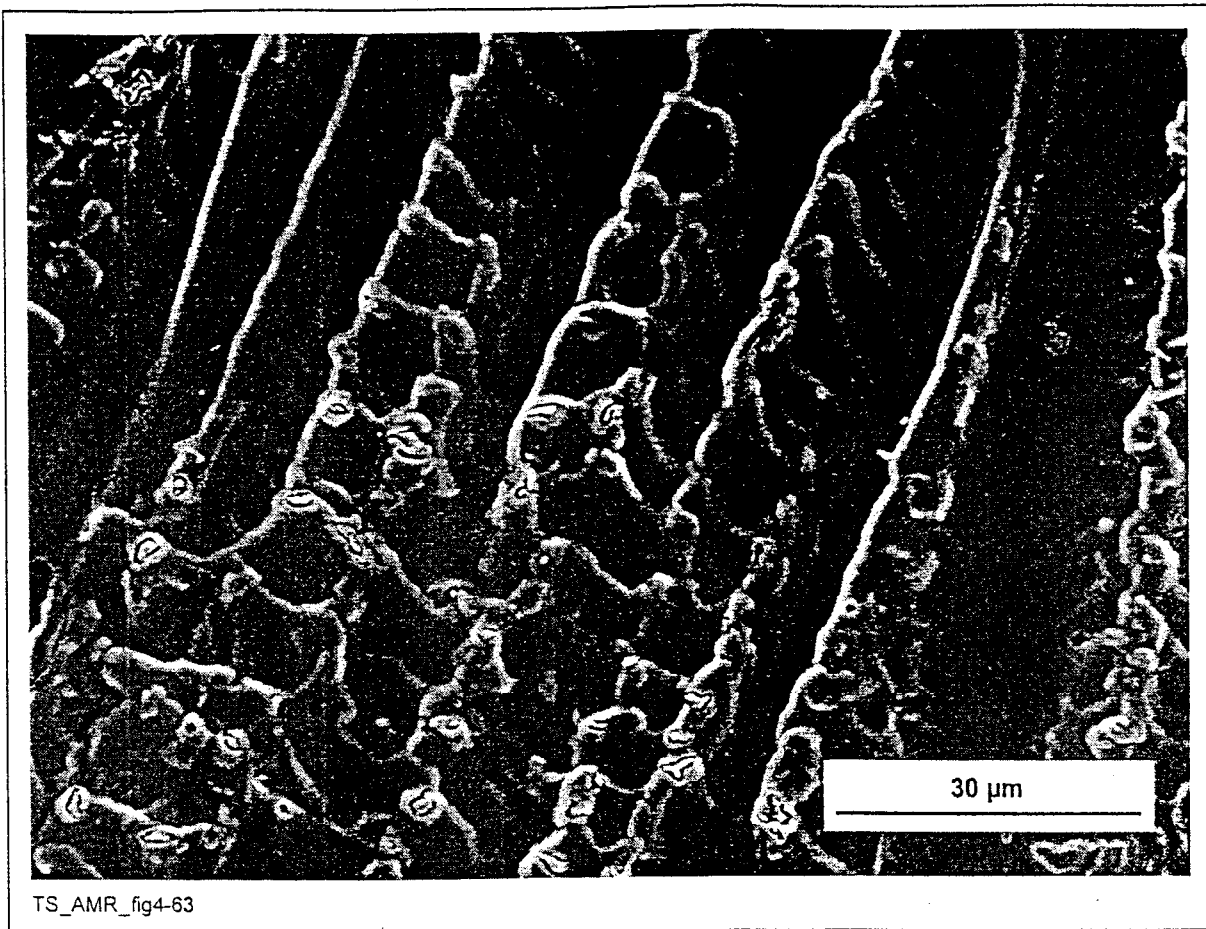


Figure 4-63. SEM Micrograph of the Alloy 22 Weld Shown in Figure 4-58 Showing the Dendritic Structure Typical of Welds

Intermetallic particles are seen to form in the interdendritic regions. (TS393-019, 8/28/98, SN #393 p.10)

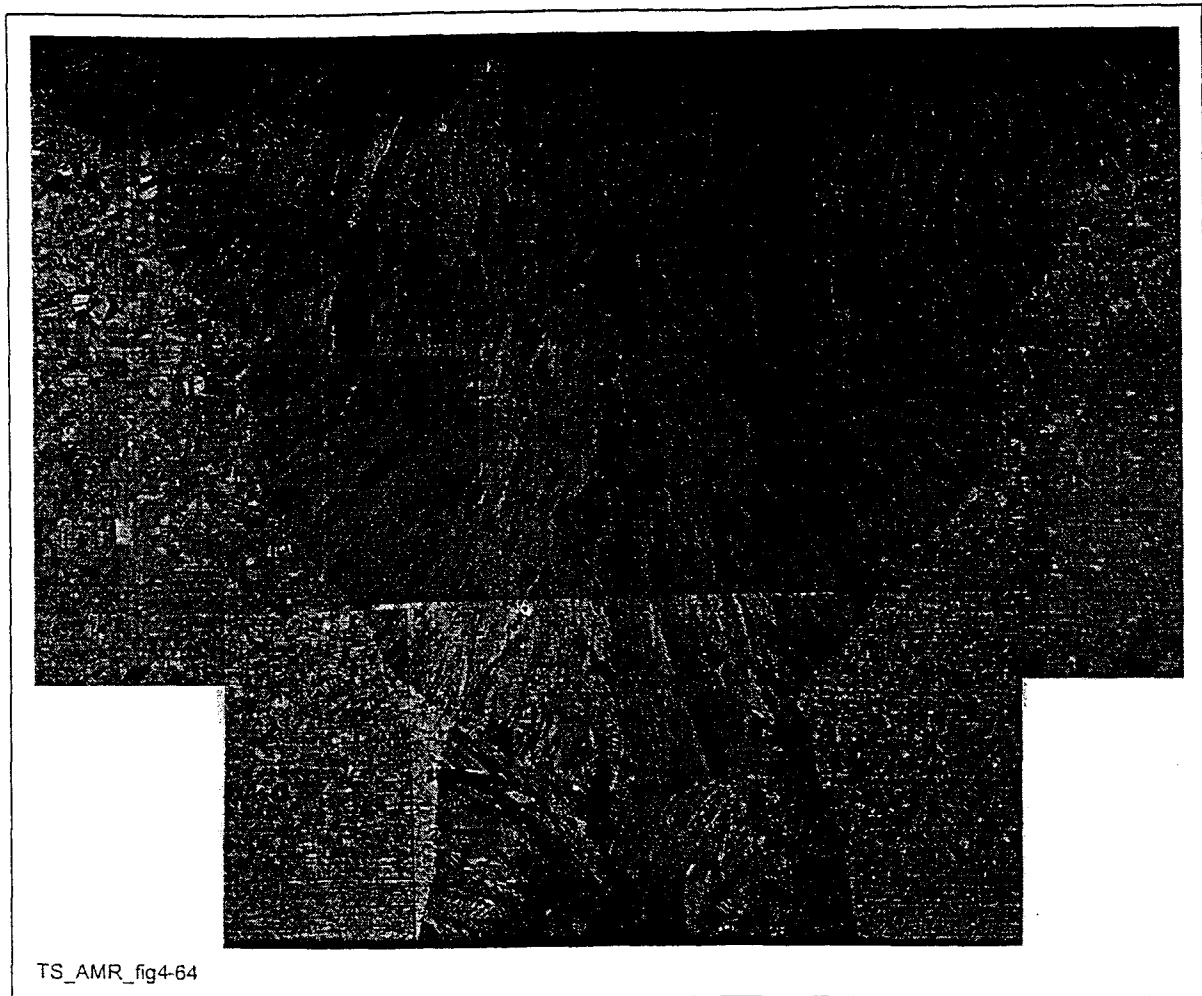


Figure 4-64. Low-Magnification Optical Micrograph of an Alloy 22 Weld Similar to that Shown in Figure 4-58, But Aged for 40,000 hr at 427°C

Only approximately one-half of the half-inch plate is shown. (TS393-005b, 5/12/98, SN #369 p.20)

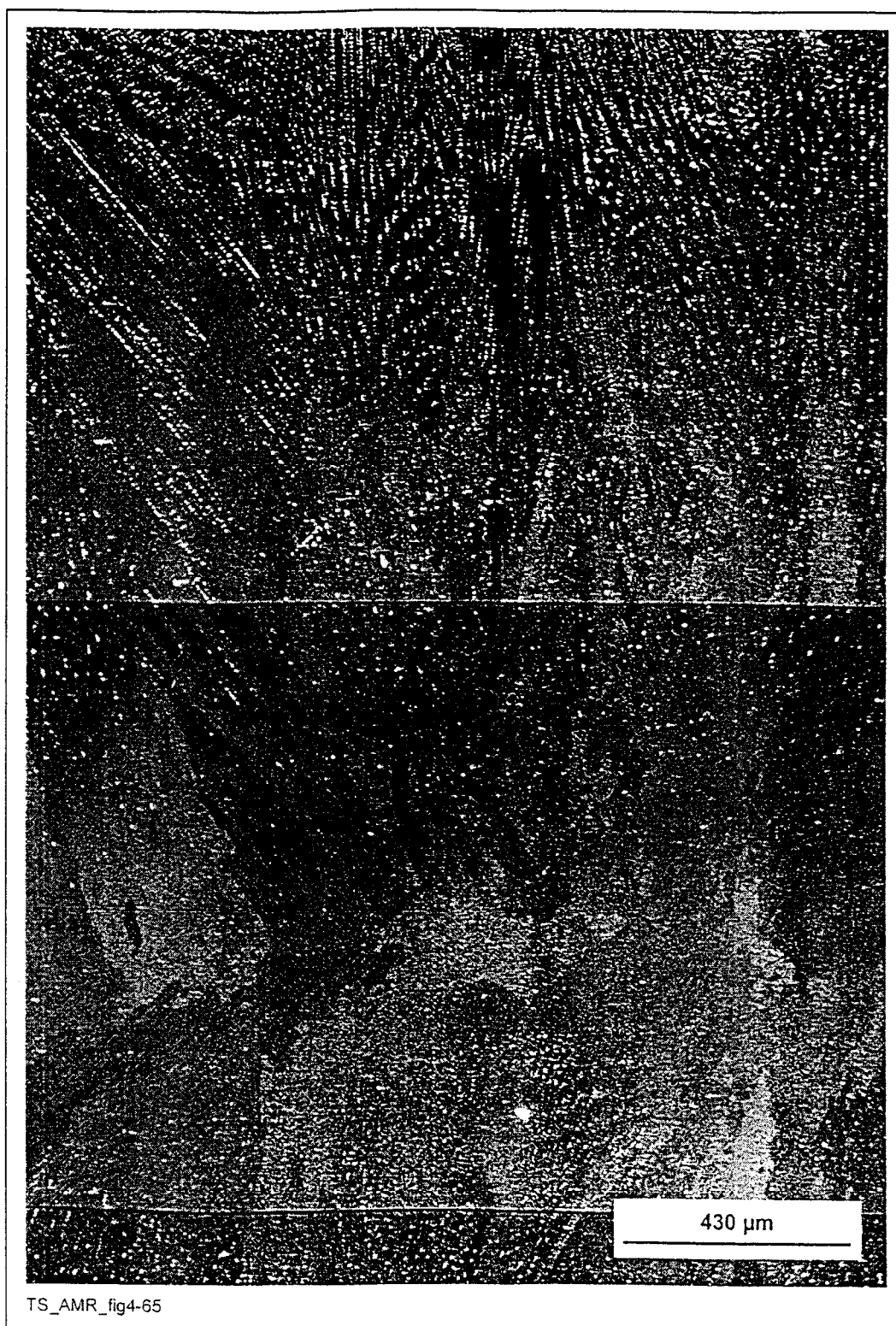


Figure 4-65. SEM Micrograph of the Alloy 22 Weld Shown in Figure 4-61 at the Junction of Two Weld Passes

The white intermetallic particles are distributed nonuniformly throughout the weld. (TS393-005b, 5/12/98, SN #369 p.20)

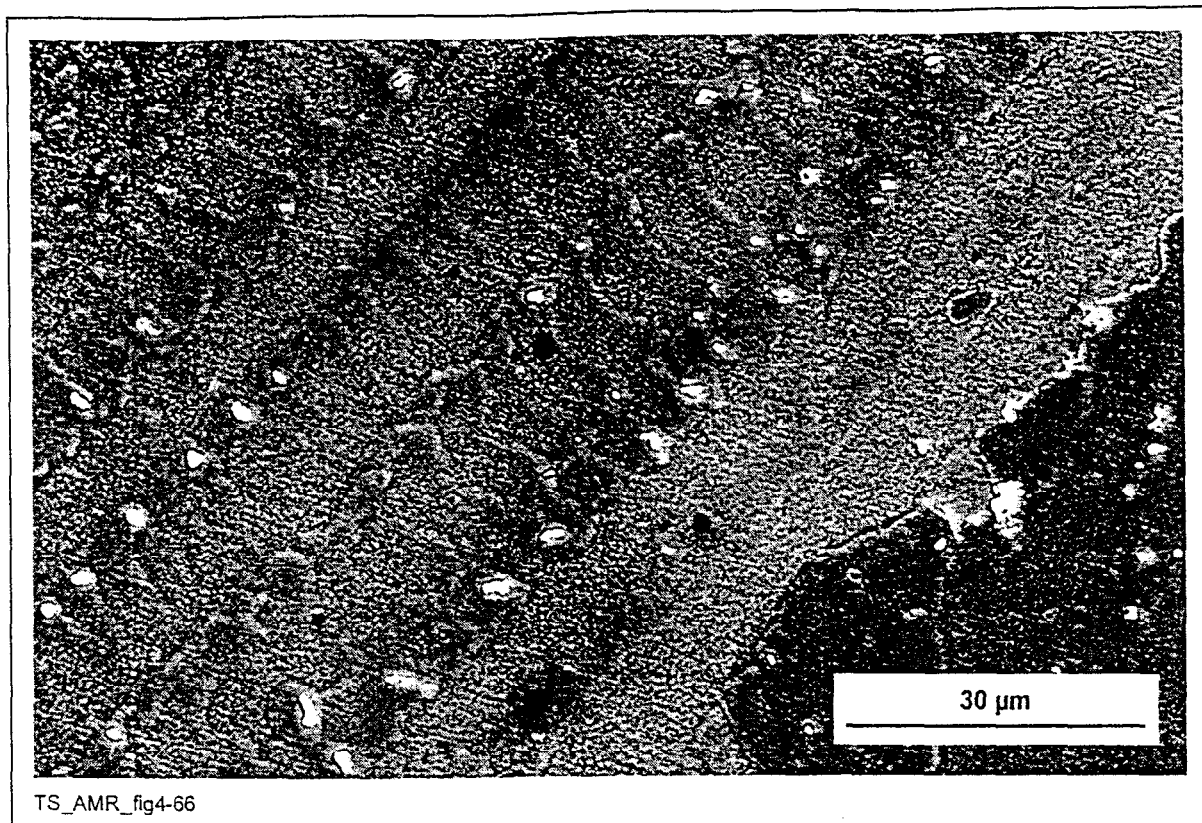


Figure 4-66. SEM Micrograph of the Alloy 22 Weld Shown in Figure 4-61 Showing the Dendritic Structure Typical of Welds

Intermetallic particles are seen to form in the interdendritic regions, as was seen in the unaged weld of Figure 4-60. (TS393-005b, 5/12/98, SN #369 p.20)



Figure 4-67. Optical Micrograph at the Fusion Line of the Alloy 22 Weld Shown in Figure 4-61

Very few precipitates are seen in the HAZ of the aged weld.
(TS393-005b, 5/12/98, SN #369 p.20)

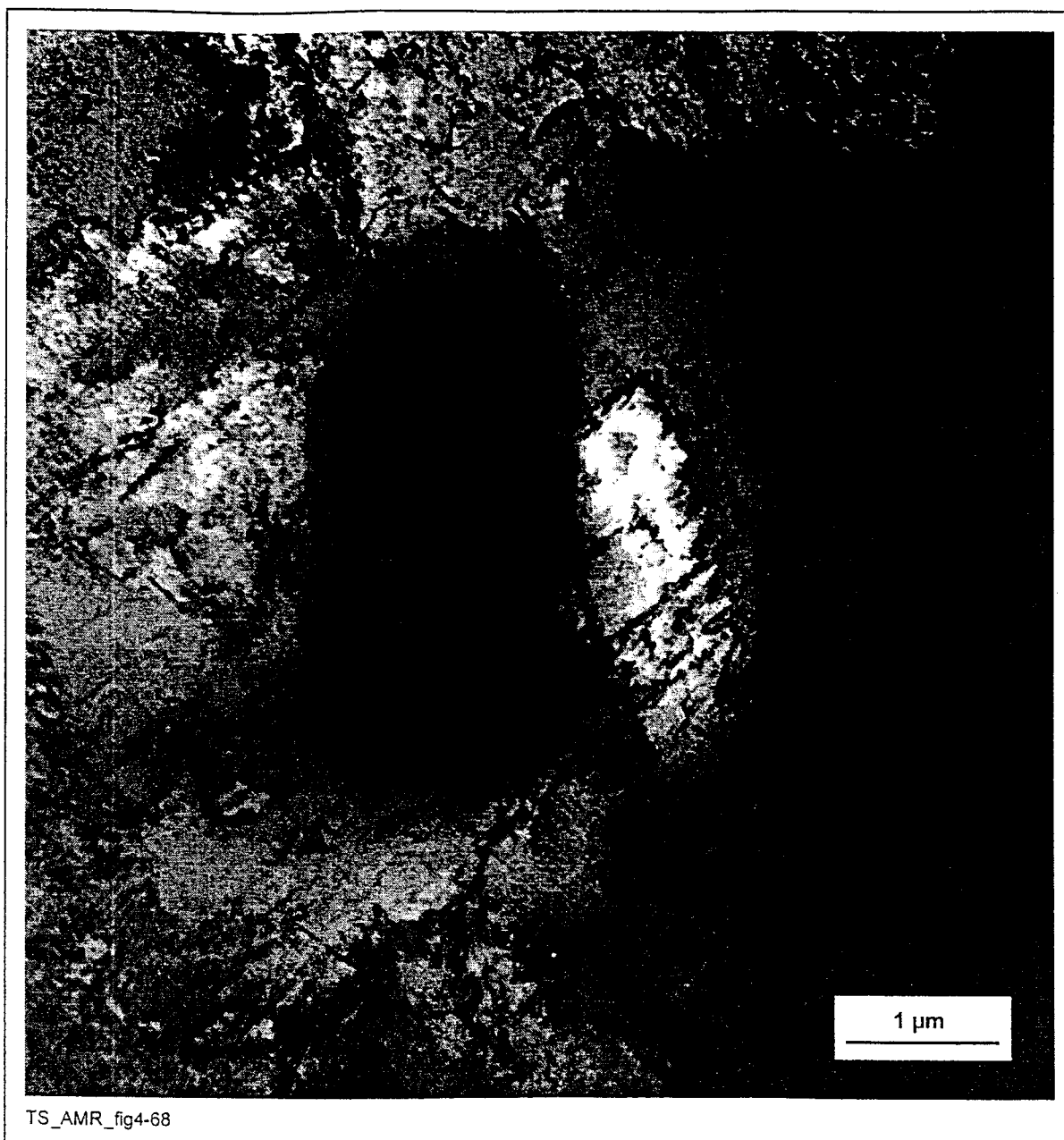
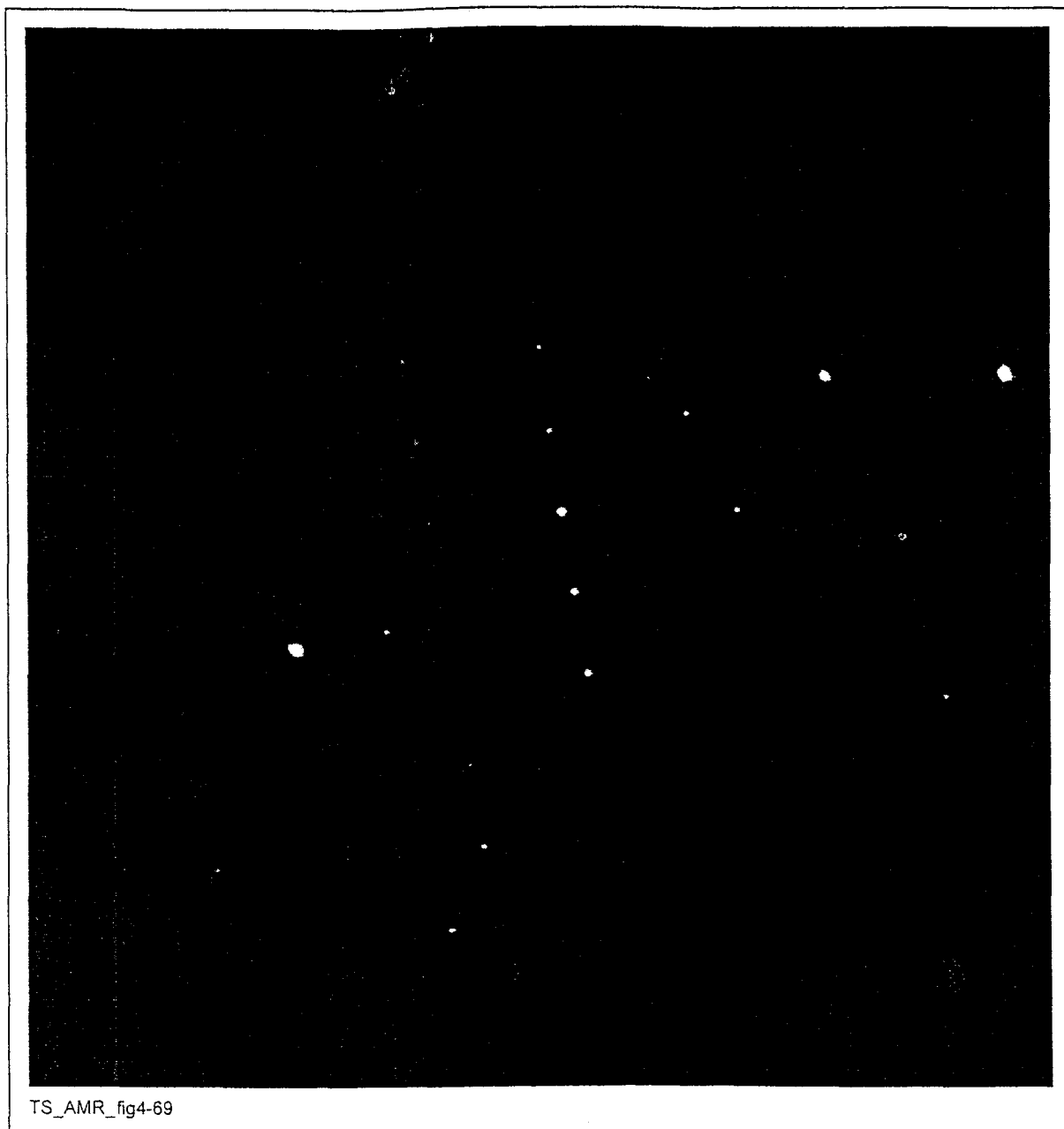


Figure 4-68. One of Few Precipitates Seen in the Alloy 22 Weld of Figure 4-61 Aged for 40,000 hr at 427°C

This particle was not conclusively identified, but could be either P or sigma (TS369-005a, Image 1373, 5/21/98, SN #393, p.27)



TS_AMR_fig4-69

Figure 4-69. SAD Pattern from the Precipitate Shown in Figure 4-65

This pattern could be indexed as either P phase or sigma. (TS369-005a, Image 1374, 5/21/98, SN #393, p.27)



Figure 4-70. SAD Pattern from the Precipitate Shown in Figure 4-65

This pattern could be indexed as either P phase or sigma. (TS369-005a, Image 1375, 5/21/98, SN #393, p.31)



Figure 4-71. TEM Micrograph Showing One of Few Precipitates Seen in the HAZ of the Aged Alloy 22 Weld of Figure 4-61

A SAD pattern was not taken from this particle, but it appears to be a carbide and was probably present in the base metal prior to welding. (TS369-005a, Image 1378, 5/22/98, SN #393, p.37)

4.1.7 Volume Fraction of Intermetallic and Carbide Precipitation in Alloy 22 Weld HAZ as a Function of Aging Time, Temperature, and Weld Type (TBD-424)

The volume fraction of precipitates in the HAZ of Alloy 22 weld samples must be determined and fit to nucleation and growth theory such as that presented in Section 6.2. Because of the thermal pulse received by the HAZ during the welding process, the kinetics of precipitation in these regions may differ from those in the base metal. Weld samples will be aged and the precipitation in the HAZ characterized.

4.1.8 Volume Fraction and Particle Size of Intermetallics and Carbides in Alloy 22 Welds as a Function of Aging Time, Temperature, and Weld Type (TBD-423)

Intermetallics and carbides form in Alloy 22 welds during the welding process. It must be determined whether these precipitates grow or shrink with aging under repository conditions. Alloy 22 weld samples will be aged, and the volume fraction and average precipitate size will be determined as a function of aging time, temperature, and welding parameters. In addition, the effect of this aging on the properties of the welds will be measured.

4.1.9 TEM Micrographs Showing When LRO Has Been Observed (TBV-1253)

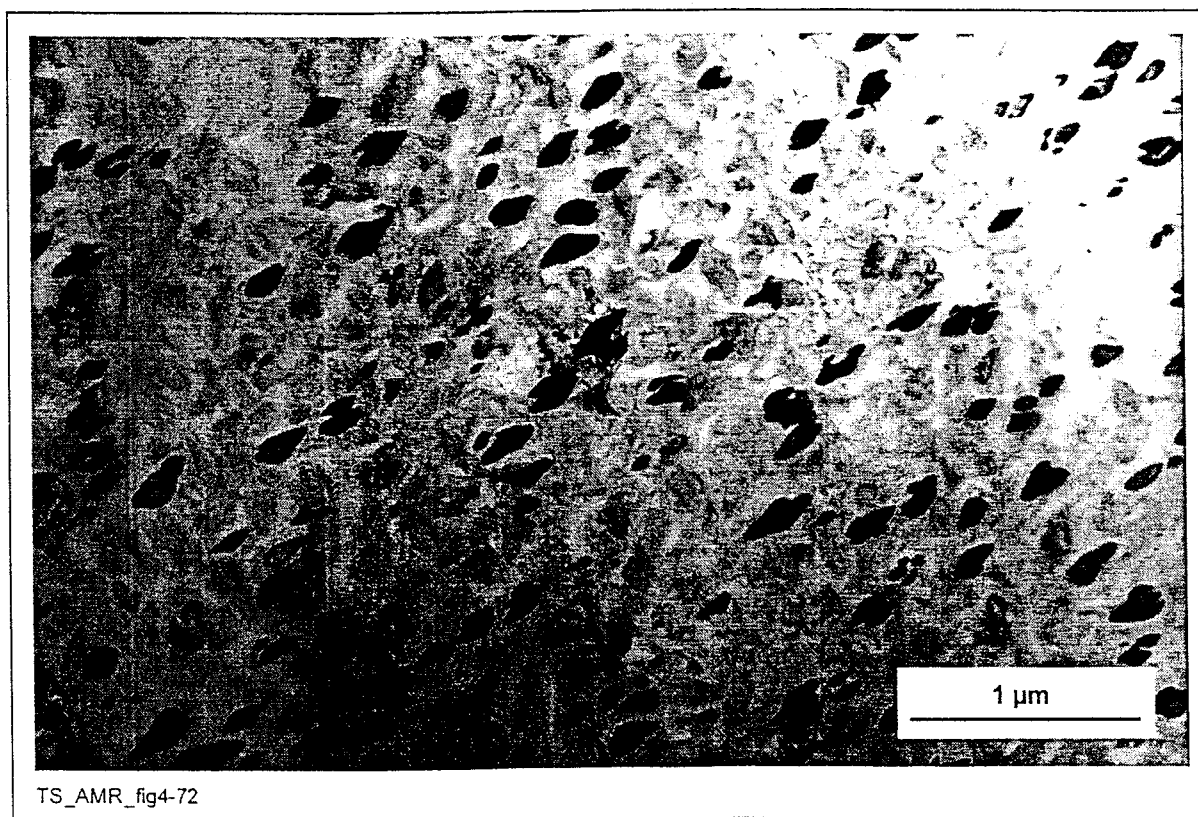


Figure 4-72. TEM Micrograph Showing LRO Domains in an Alloy 22 Base Metal Sample Aged for 16,000 hr at 593°C

(TS369-003a, Image 1484, 12/16/98, SN #393, p.61)



Figure 4-73. Dark-Field Image Corresponding to Figure 4-69

One variant of the ordered domains appears light. (TS369-003a, Image 1485, 12/16/98, SN #393, p.61)

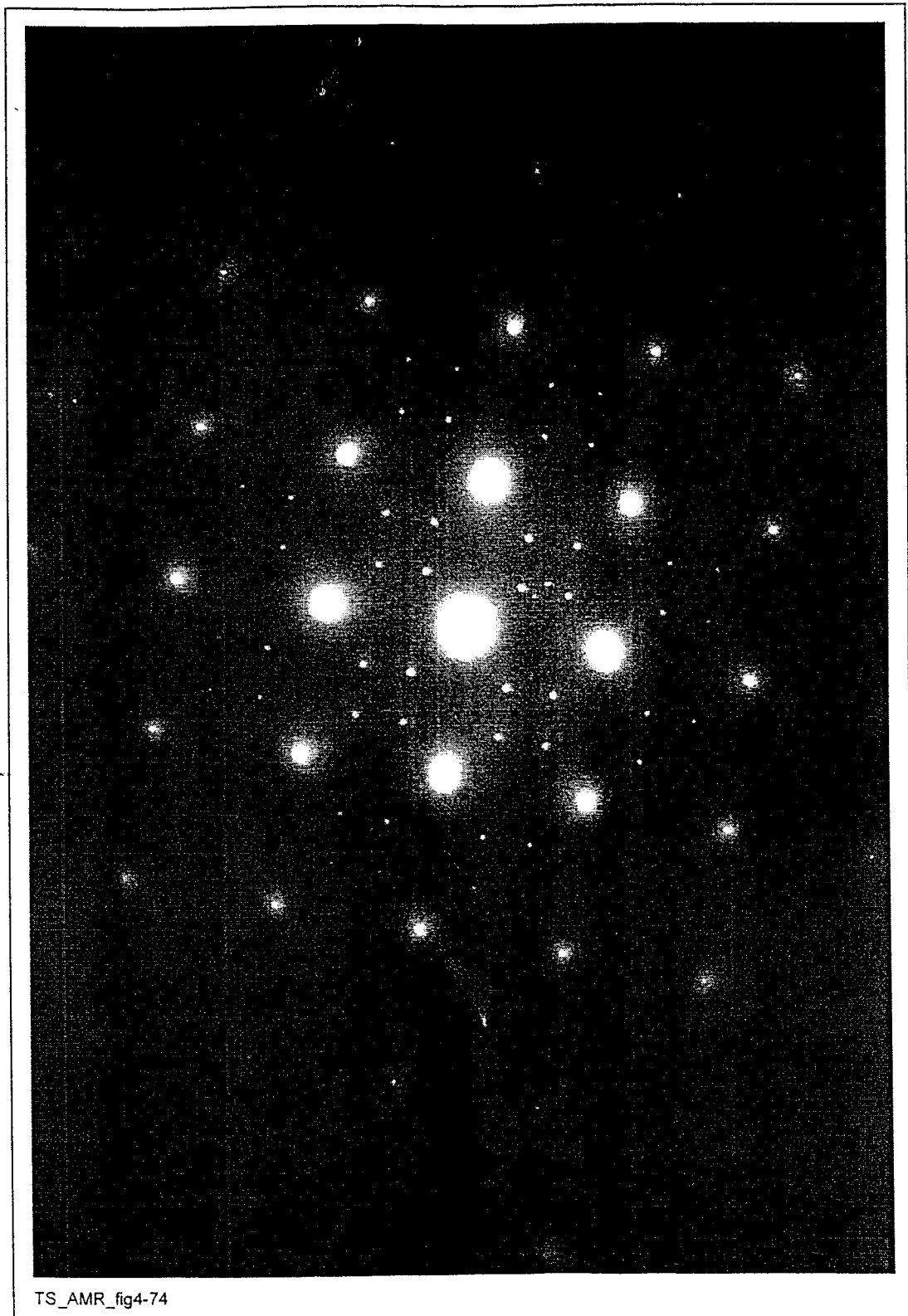


Figure 4-74. SAD Pattern from the Area Shown in Figure 4-69

The faint superlattice reflections are due to LRO. (TS369-003a, Image 1483, 12/16/98, SN #393, pp.61-65)

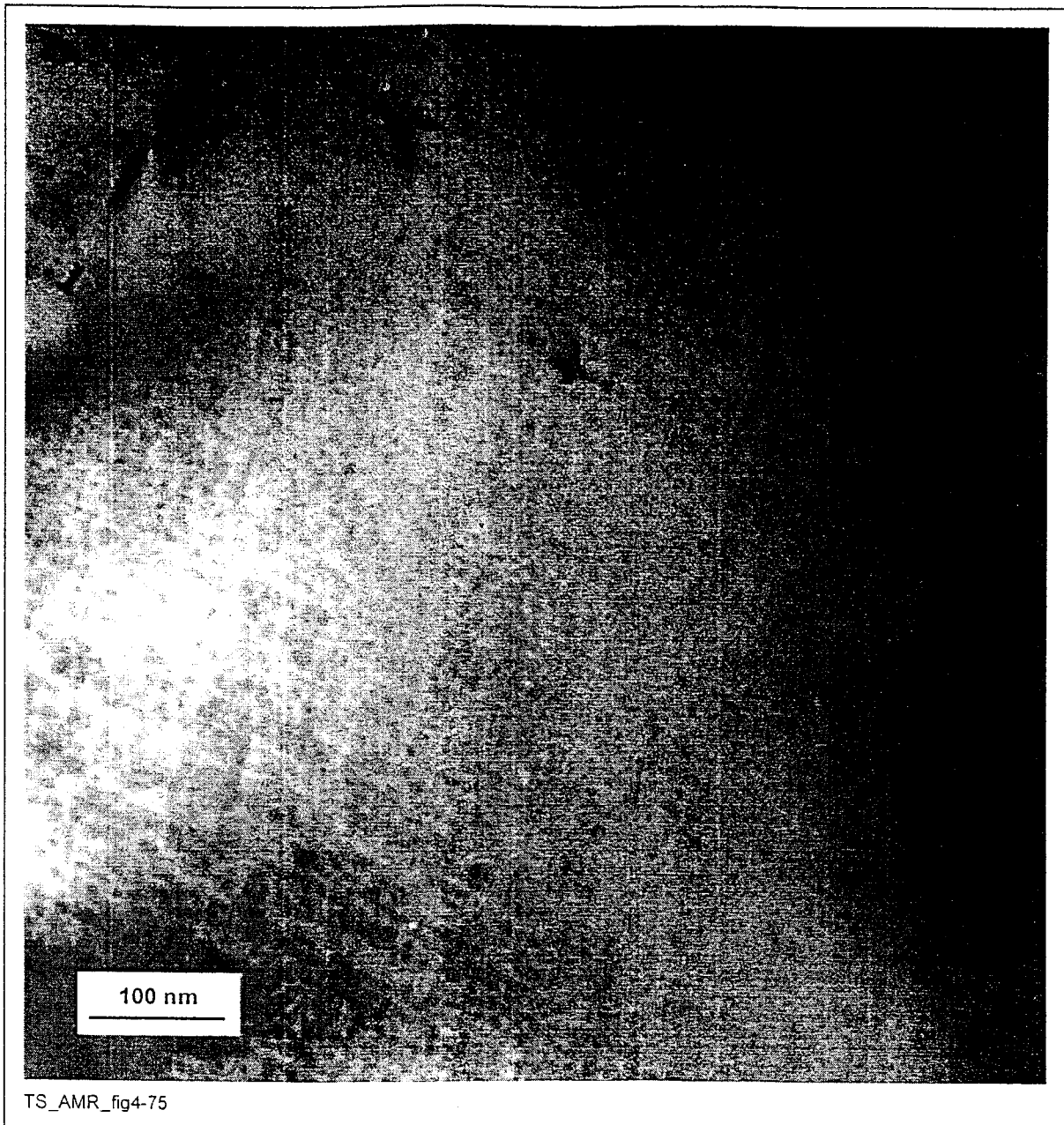


Figure 4-75. TEM Micrograph from the Base Metal of an Alloy 22 Weld Sample Aged for 40,000 hr at 427°C (TS369-005a base metal, Image 1354, 3/20/98, SN #369 p.132)

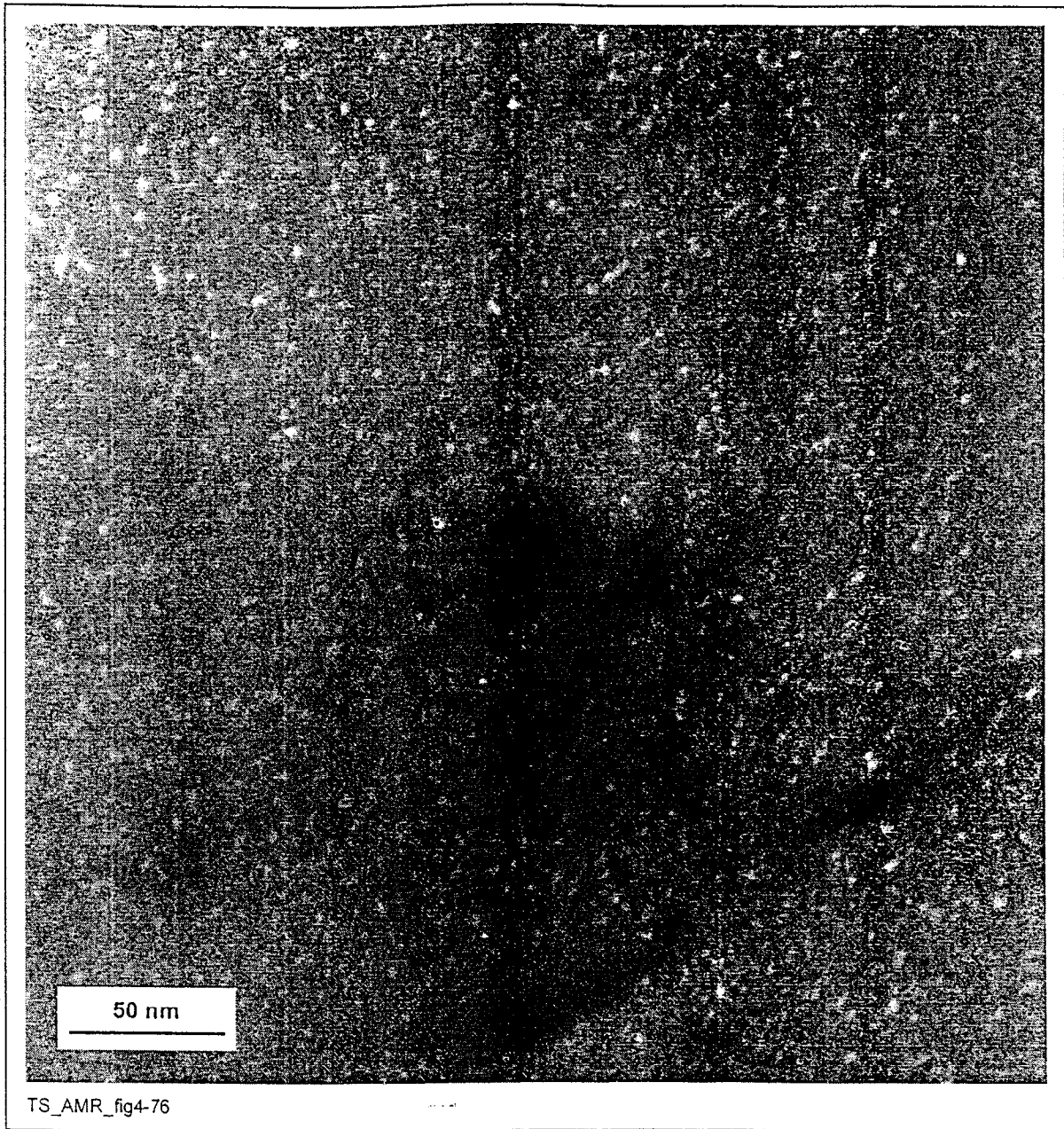


Figure 4-76. Dark-Field Image Corresponding to Figure 4-72

One variant of the ordered domains appears light. (TS369-005a base metal, Image 1356, 3/20/98, SN #369 p.133)

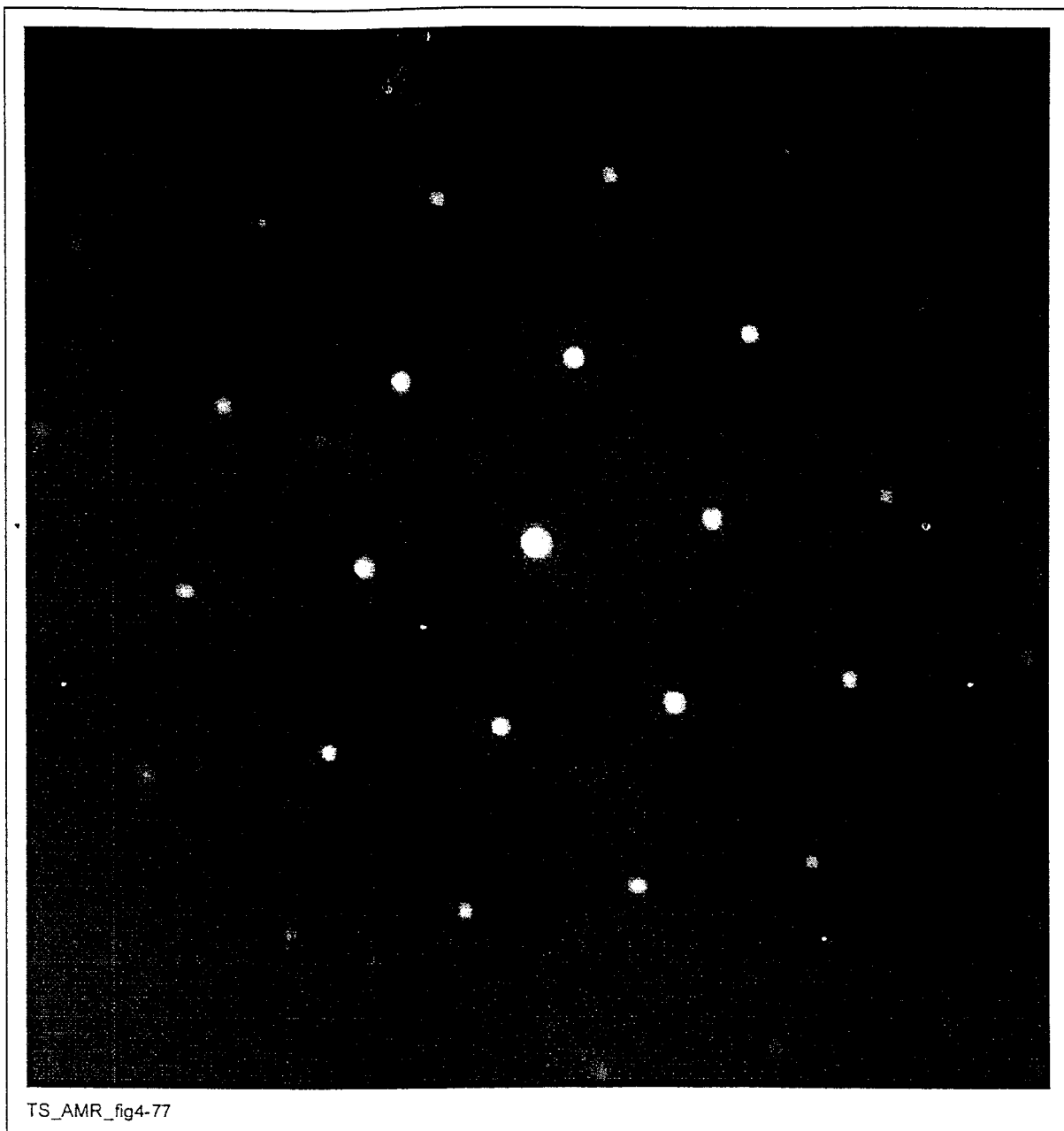


Figure 4-77. SAD Pattern from the Area Shown in Figure 4-74

The faint superlattice reflections are due to LRO. (TS369-005a base metal, Image 1353, 3/20/98, SN #369 p.131)

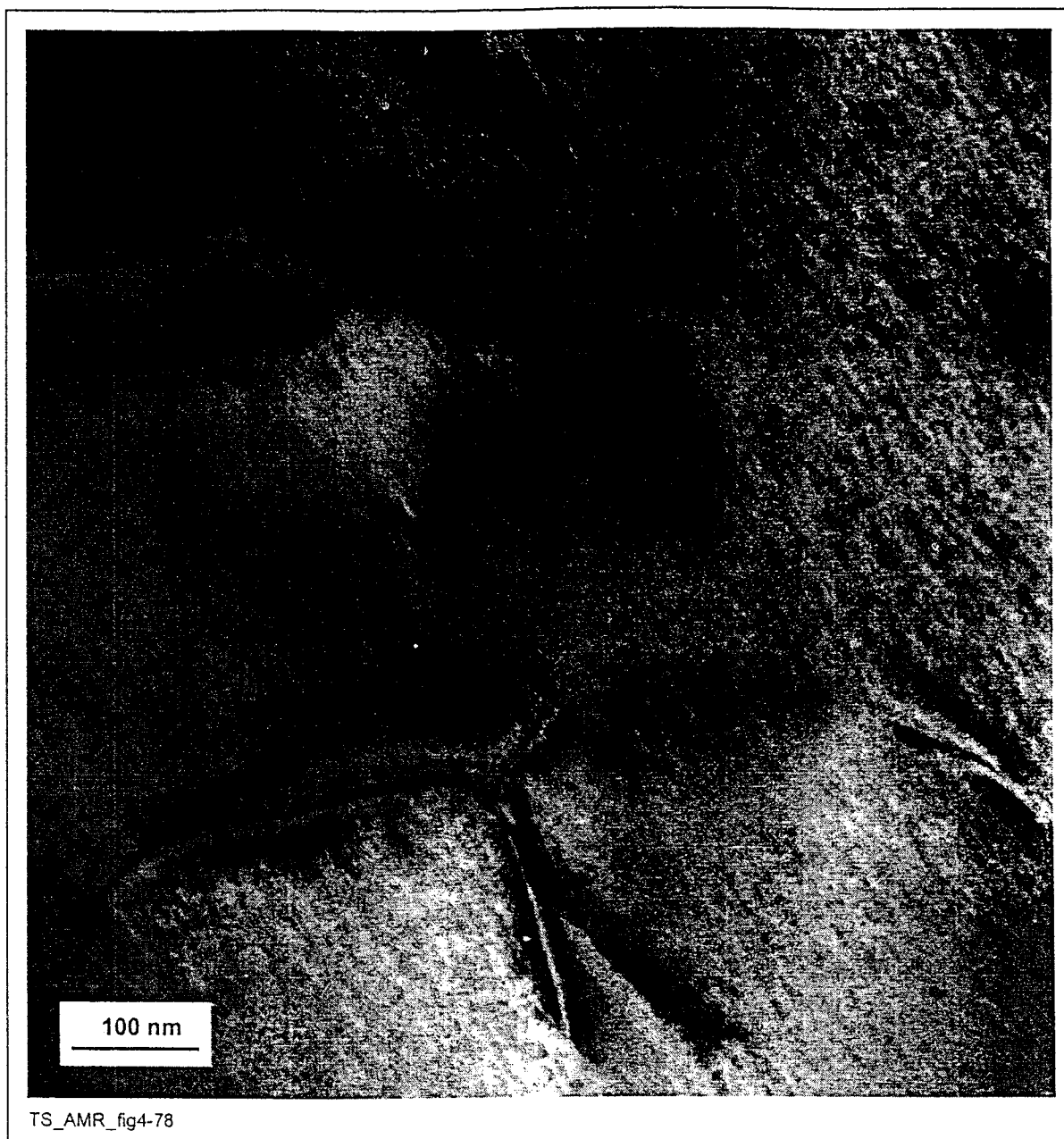


Figure 4-78. TEM Micrograph from the Weld Metal of an Alloy 22 Multipass, Double-V GTAW Weld with Matching Filler Metal Aged for 40,000 hr at 427°C

(TS369-005a weld metal, Image 1371, 5/21/98, SN #393, p.26)

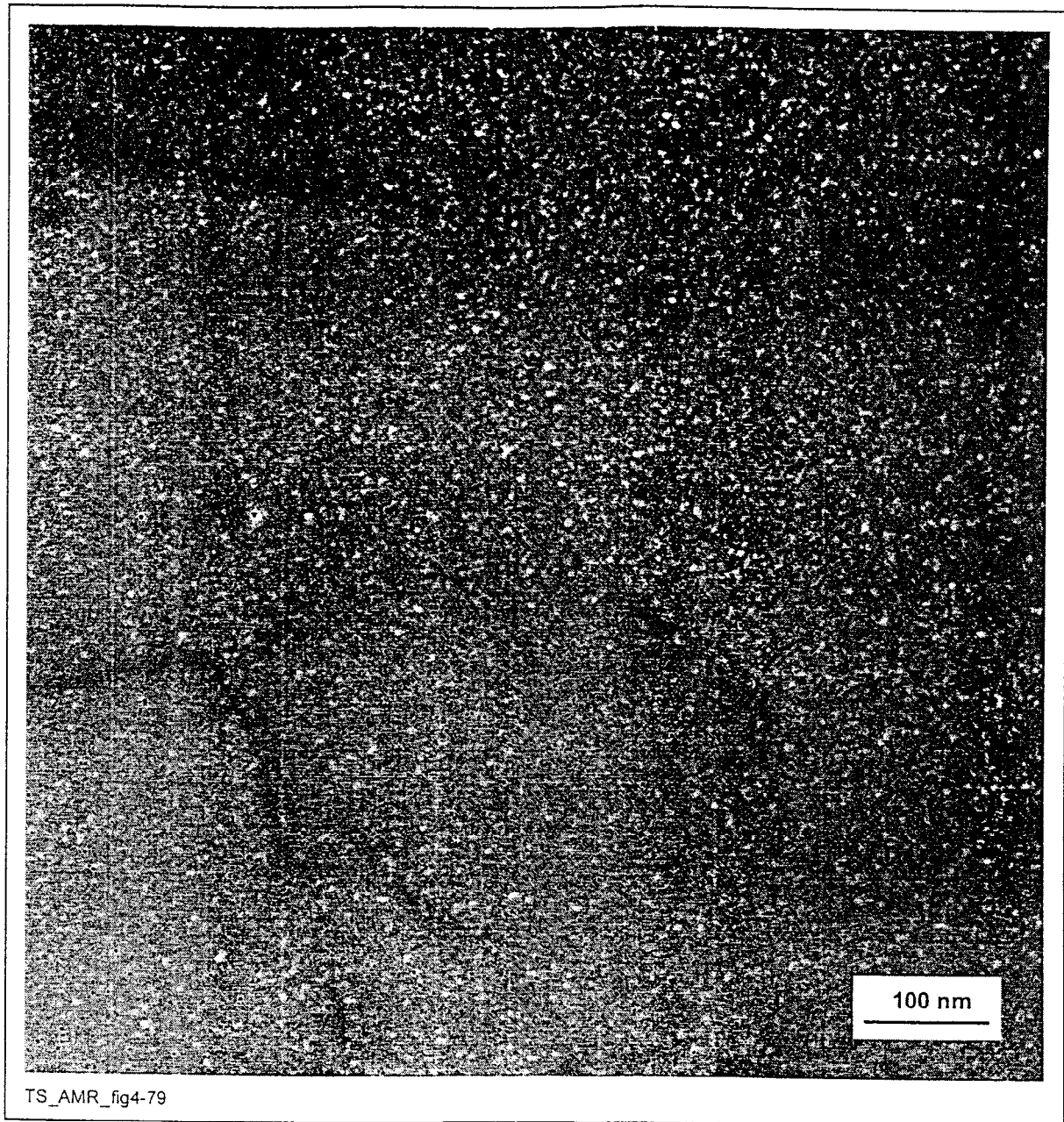
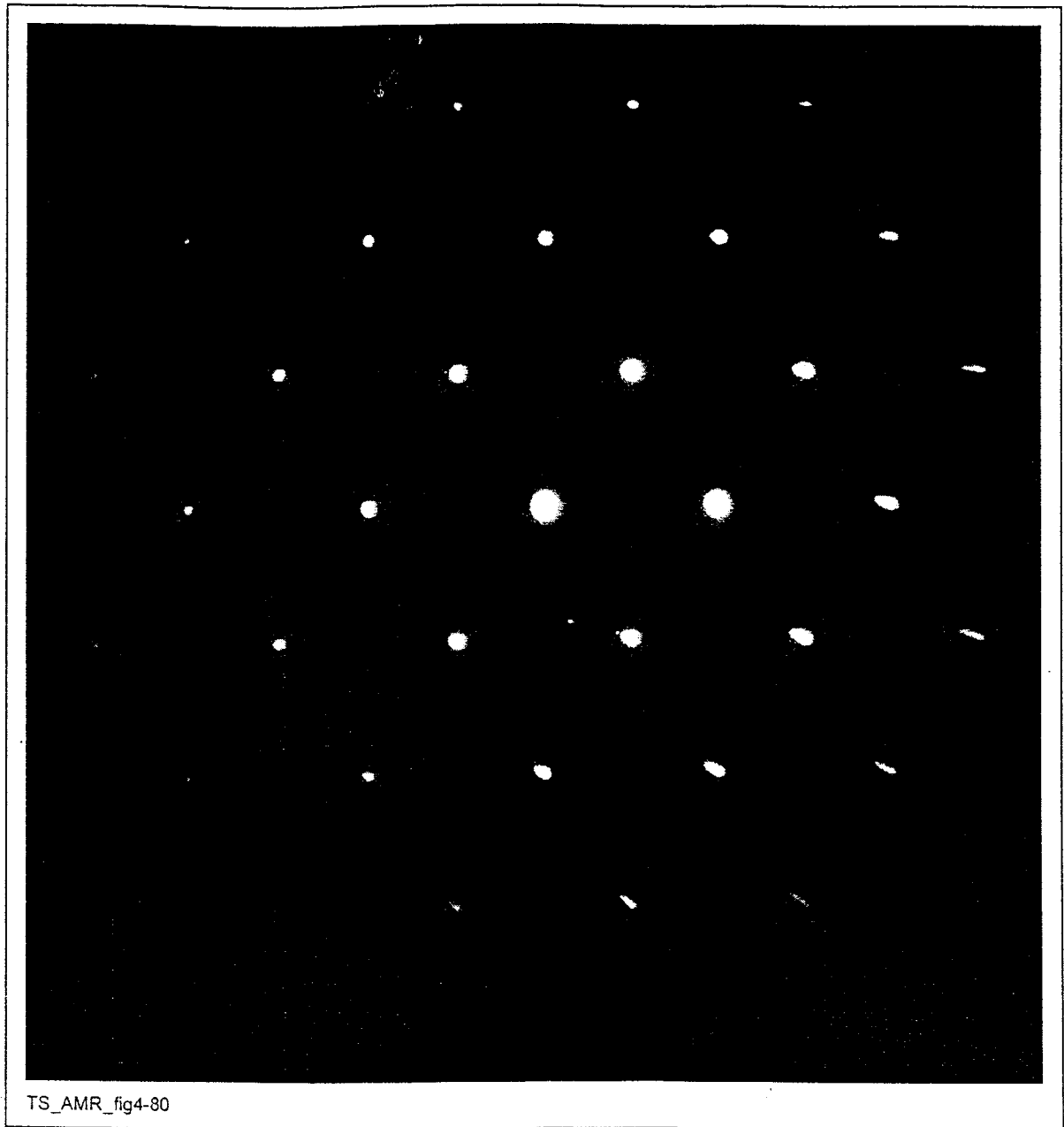


Figure 4-79. Dark-Field Image Corresponding to Figure 4-75

The faint white regions are ordered domains. (TS369-005a weld metal, Image 1372, 5/21/98, SN #393, p.26)



TS_AMR_fig4-80

Figure 4-80. SAD Pattern from the Area Shown in Figure 4-75

The faint superlattice reflections are due to LRO. (TS369-005a weld metal, Image 1370, 5/21/98, SN #393, p.25)



Figure 4-81. TEM Micrograph from the HAZ of the Alloy 22 Multipass, Double-V GTAW Weld with Matching Filler Metal (Figure 4-75) Aged for 40,000 hr at 427°C

(TS369-005a HAZ, Image 1379, 5/22/98, SN #393, p.38)

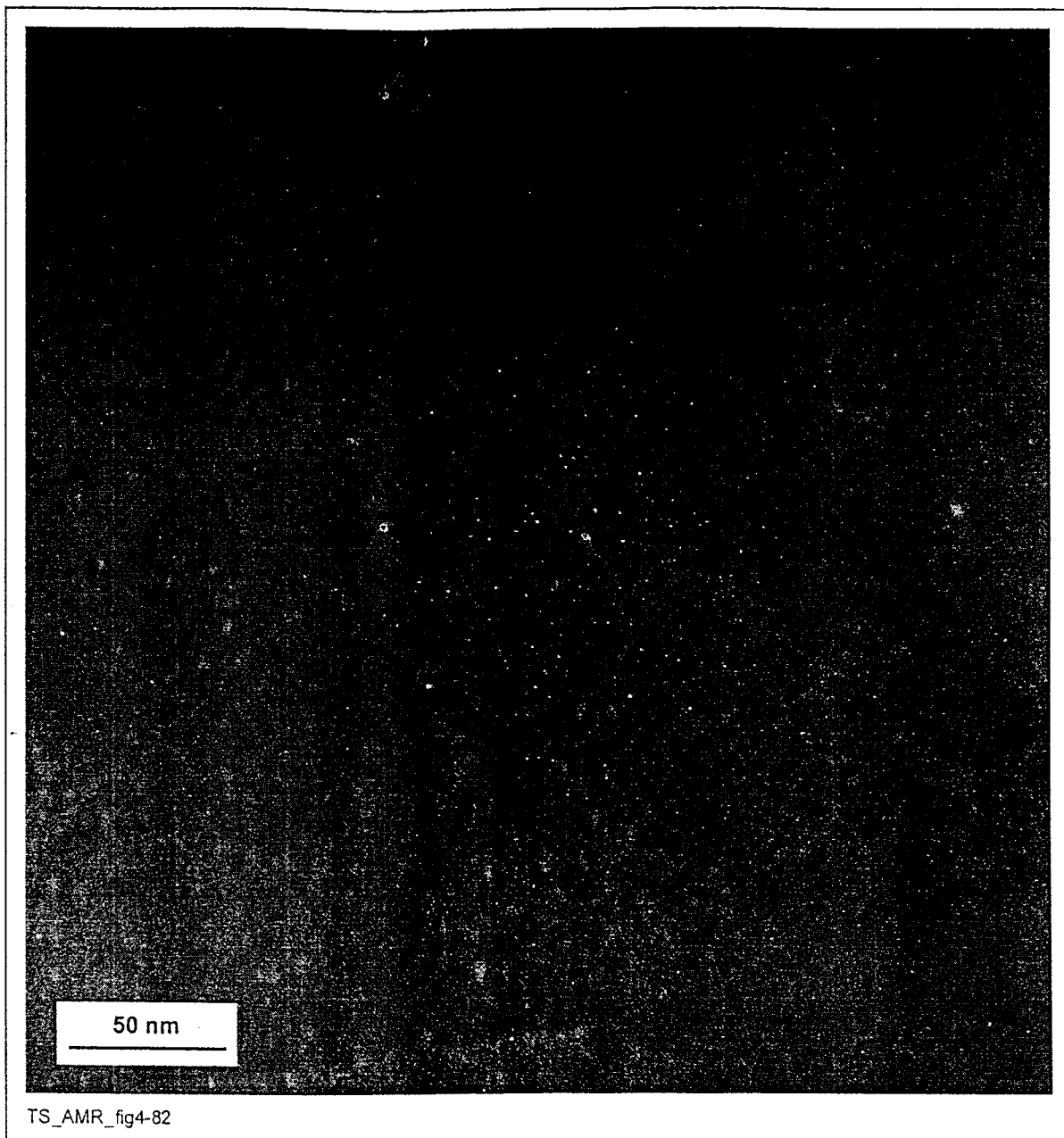
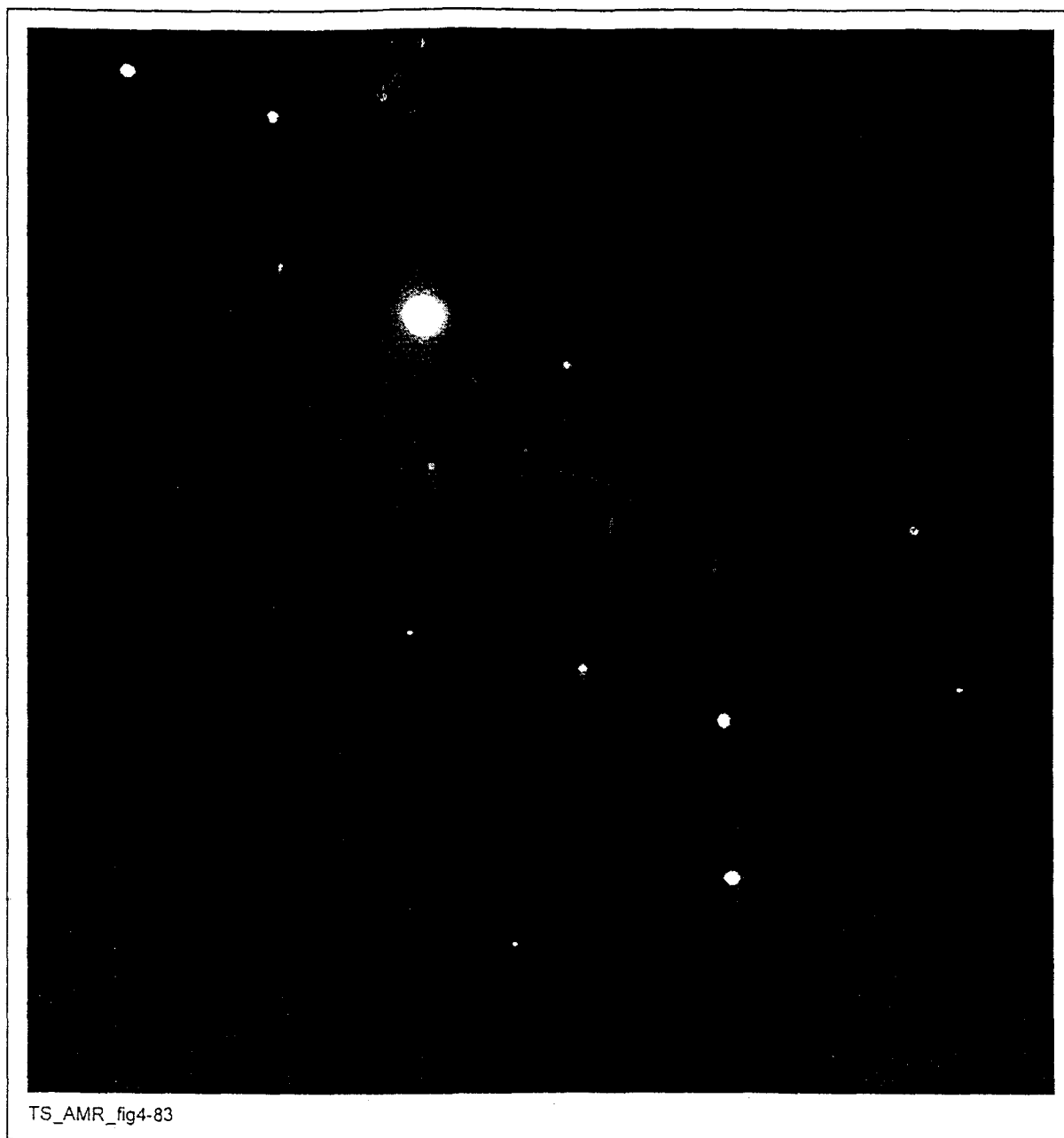


Figure 4-82. Dark-Field Image Corresponding to Figure 4-78

The faint white regions are ordered domains. (TS369-005a HAZ, Image 1380, 5/22/98, SN #393, p.39)



TS_AMR_fig4-83

Figure 4-83. SAD Pattern from the Area Shown in Figure 4-78

The faint superlattice reflections are due to LRO. (TS369-005a HAZ, Image 1381, 5/22/98, SN #393, p.39)

CHECK COPY

4.1.10 TEM Micrographs Used to Determine Volume Fraction of Ordered Domains Present in Alloy 22 as a Function of Aging Time, Temperature, and Starting Material (Base Metal or Weld) (TBD-422)

Ordering has been observed, as shown in Figures 4-72 through 4-83, in a sample aged at 593°C for 16,000 hr and in samples aged at 427°C for 40,000 hr. To determine the rate at which ordering occurs in Alloy 22, the volume fraction of ordered domains must be measured as a function of aging time and temperature. Alloy 22 samples will be aged at temperatures less than 600°C and examined in TEM to determine the rate at which LRO occurs.

4.2 CRITERIA

The following criteria apply to phase stability studies of the WPOB:

- The disposal container shall be designed such that no more than 1 percent of all waste packages breach during the first 1000 yr after emplacement (breaching is defined as an opening through the wall of the waste package through which advective or diffusive transport of gas or radionuclides can occur) (CRWMS M&O 1999b, subsection 1.2.1.3).
- The disposal container shall be designed such that for 10,000 yr after permanent closure of the repository, the release rate of any radionuclide from all waste packages shall not exceed 1 part in 100,000 per year of the inventory of that radionuclide calculated to be present at 1000 yr following permanent closure; provided that this requirement does not apply to any radionuclide that is released at a rate less than 0.1 percent of the calculated total release-rate limit. The calculated total release-rate limit shall be taken to be 1 part in 100,000 per year of the inventory of radioactive waste, originally emplaced in the underground facility, that remains after 1000 yr of radioactive decay (CRWMS M&O 1999b, subsection 1.2.1.4).

4.3 CODES AND STANDARDS

There are no codes or standards used in this document.

5. ASSUMPTIONS

5.1 RELEVANT WPOB MATERIAL TEMPERATURES LESS THAN 350°C

"The disposal container shall maintain Spent Nuclear Fuel (SNF) Zircaloy™ and stainless steel cladding temperature below 350°C" (CRWMS M&O 1999b, subsection 1.2.1.11). Because the WPOB material will be at a lower temperature than will the SNF cladding, the relevant temperatures are assumed to be less than 350°C.

5.2 KINETICS SAME FOR THE INTERMETALLIC AND CARBIDE PHASES IN ALLOY 22 (TBV)

The relative amounts of μ , P, sigma, and carbide phases have not been quantified; thus, the kinetics of formation of these phases cannot be calculated independently at this time; it is probably reasonable to assume that their rates of formation are similar. The amount of carbide and sigma phases tends to be low in the samples examined thus far. Therefore, the rates of formation of these phases are not likely to contribute significantly to the overall performance of the WPOB nor are they likely to affect the transformation rates calculated based on volume fraction measurements, which include these phases in the total precipitate volume. The μ and P phases are very similar (Leonard 1969, p. 225, ¶ 4; Raghavan et al. 1982, p. 983, Conclusions section, pt. 2), and the rate at which they form is likely to be similar. It also appears that P phase is a precursor to μ phase (Leonard 1969, p. 223, Figure 1). This would also explain why more P phase (relative to the amount of μ phase) has been observed at the lower temperatures than at the higher temperatures. If P phase is a precursor to μ phase, including the total amount of P+ μ as input to the kinetic model is appropriate. A procedure for the quantification of the individual amounts of μ , P, sigma, and carbide is currently being developed. Once this procedure is developed, this assumption can be tested directly.

5.3 TRANSFORMATION MECHANISMS OPERATING AT THE HIGHER TEMPERATURES INVESTIGATED ALSO OPERATE AT THE LOWER EXPECTED REPOSITORY TEMPERATURES (TBV)

For a WP lifetime of 10,000 yr, it is impossible to test directly in the laboratory the behavior of WPOB materials under expected repository conditions. The changes that may occur in these materials must be accelerated. For phase-stability studies, phase transformations are accelerated by increasing the temperature. Extrapolation to low temperatures of kinetic data taken at high temperatures assumes two things: 1) the phases that are thermodynamically stable at high temperatures are also stable at the lower temperatures and 2) the mechanism by which the phases form at high temperatures also operates at the lower temperatures. The lower the temperature from which the extrapolation is made, the more likely the validity of these assumptions. Long-term aging studies, which are currently underway, will allow measurements to be made at temperatures as low as 260°C. Also, theoretical modeling aimed at calculating the Alloy 22 phase diagram and precipitation kinetics has just been started (see Sections 6.8 and 6.9). These calculations will further support the use of this assumption or provide means of calculating WPOB lifetime in the absence of this assumption.

5.4 MINOR CHEMISTRY CHANGES WITHIN ASTM SPECIFICATION B575 (HEAT-TO-HEAT VARIABILITY) DO NOT SIGNIFICANTLY AFFECT THE PHASE STABILITY OF ALLOY 22 (TBV)

It is assumed, in this version of the phase-stability analysis, that compositional changes falling within the range acceptable according to ASTM specification B575 (ASTM 1994) for Alloy 22 do not significantly affect the precipitation kinetics. Eventually, work will need to be done to investigate heat-to-heat variability. At that time, if this assumption turns out not to be valid, the effect of minor compositional changes on phase stability will be evaluated.

6. ANALYSIS/MODEL

6.1 PHASE IDENTIFICATION IN ALLOY 22

Alloy 22 samples were aged for 16,000 hr at 593, 649, 704, and 760°C and examined in TEM. A weld sample aged at 427°C for 40,000 hr was also observed in the weld metal, in the HAZ, and in the base metal removed from the weld. The other samples used for the subsequent kinetic arguments were not examined in TEM. Several phases were observed to form in Alloy 22: P, μ , sigma, carbide, and $\text{Ni}_2(\text{Cr},\text{Mo})$ LRO. At 593°C, P phase was observed only on the grain boundaries. This is shown in Figures 4-1 through 4-3. At the higher aging temperatures (649, 704, and 760°C), both μ and P phase precipitated on grain boundaries (see Figures 4-6 through 4-11, 4-15, 4-18, 4-19, 4-22, 4-24, and 4-34 through 4-36). As the aging temperature increased, more μ and P phase precipitation occurred within the grains (see Figures 4-12 through 4-14, 4-25 through 4-27, 4-32, 4-33, and Section 6.2). Grain boundary carbide precipitation was observed in samples aged at 593 and 704°C (see Figures 4-4, 4-5, 4-15 through 4-17, 4-20, and 4-21). Because of the small amount of carbide present in these samples and the small volume examined in TEM, it is likely that carbides also form at 649°C. They may or may not form at 760°C. Because of the similarity between the M_6C , the M_{12}C , and the M_{23}C_6 -type carbide crystal structures, the specific carbide forming in these samples was not identified; however, it is a cubic carbide with lattice parameter of 10–11 Å. Sigma phase was observed in the samples aged at 704 and 760°C (see Figures 4-22, 4-23, and 4-28 through 4-31). The amount of sigma observed in these samples was small compared to the amount of μ and P. LRO was observed in the sample aged at 593°C for 16,000 hr (see Figures 4-72 through 4-74) and in the sample aged at 427°C for 40,000 hr (see Figures 4-75 through 4-83). These observations are summarized in Table 6-1.

Table 6-1. Phases Observed in Alloy 22 in TEM (TBV)

Aging Condition	Phases Observed to Form in Alloy 22
427°C for 40,000 hr	LRO No signs of grain boundary precipitation in base metal
593°C for 16,000 hr	LRO Grain boundary films of P phase Carbide precipitates at grain boundaries
649°C for 16,000 hr	Precipitation of P and μ phase mainly at grain boundaries
704°C for 16,000 hr	Precipitation of P and μ phase at grain boundaries and within the grains Carbide and Sigma precipitation at grain boundaries
760°C for 16,000 hr	Precipitation of P and μ phase at grain boundaries and within the grains Sigma precipitation at grain boundaries

6.2 KINETICS OF INTERMETALLIC PRECIPITATION IN ALLOY 22

For this preliminary investigation, no distinction has been made between the various intermetallic and carbide phases that form. It is very difficult to distinguish these phases in SEM. Instead, it is assumed that the P and μ phases are kinetically similar and that there is only a small amount of carbide and σ phase. It is generally accepted that P and μ are similar (Leonard 1969, p. 225, ¶ 4; Raghavan et al. 1982, p. 983, Conclusions section, pt. 2), and thus the kinetics of their formation is expected to be similar. The validity of these assumptions will be verified as discussed in Section 5.2.

CHECK COPY

Table 6-2 lists the approximate times for the noted stages of intermetallic precipitation in Alloy 22 as a function of temperature. These times were approximated from the images in Figures 4-37 through 4-60. Aged samples were observed after approximately 1, 10, 100, 1000, and in some cases 16,000 hr. The errors noted are due to the uncertainty associated with the coarse time intervals of examination and not with any measurement and test equipment uncertainties, which are assumed to be much smaller. For example, if precipitation was observed on twin boundaries at 100 hr, it could have begun at any time between 10 and 100 hr. In that case, the time noted would be 64.5 hr, with upper and lower error bars of 54.5 hr. Because of the coarse examination intervals, there is some judgment involved in choosing the times noted in Table 6-2. These measurements are only intended as an initial estimate of the precipitation kinetics. The preceding observations were also used to generate the isothermal time-temperature-transformation (TTT) diagram shown in Figure 6-1. The curve associated with LRO came from TEM observations. Only a limited number of samples were examined in TEM; thus, it is likely that ordering occurs at shorter times than indicated in Figure 6-1.

Table 6-2. Time for Intermetallic and Carbide Precipitation in Alloy 22 to Begin On and Cover Grain Boundaries, Begin on Twin Boundaries, and Begin Within the Grains as a Function of Temperature

(TBV-1256)

Temp	Time to Start on Grain Boundaries			Time to Cover Grain Boundaries		
°C	Lower Error	Time (hr)	Upper Error	Lower Error	Time (hr)	Upper Error
593	0	10	90	15000	16000	0
649	1	1	9	450	550	450
704	1	1	0	90	100	900
760	1	1	0	9	10	109
800	1	1	0	9	10	90
Temp	Time to Start on Twin Boundaries			Time to Start Within Grains		
°C	Lower Error	Time (hr)	Upper Error	Lower Error	Time (hr)	Upper Error
593						
649	900	1000	0	7500	8500	7500
704	90	100	900	900	1000	0
760	54.5	64.5	54.5	109	119	881
800	45	55	45	45	55	45

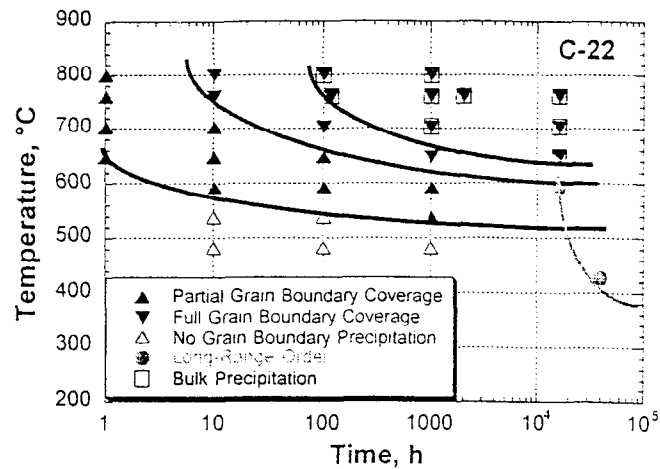


Figure 6-1. Isothermal TTT Diagram for Alloy 2 (TBV;

Nucleation and growth kinetics can often be represented by an equation of the form:

$$f = 1 - \exp(-kt^n) \quad (6.1)$$

where f is the volume fraction of the precipitating phase, t is time at the aging temperature, and k and n are constants (Christian 1975, p. 19, eqn. 4.11). The value of k depends on nucleation and growth rates and thus depends very strongly on temperature, usually of the form

$$k = C_1 \exp(-C_2 / T) \quad (6.2)$$

where C_1 and C_2 are constants, and T is the temperature (e.g., Christian 1975, p. 438 eqn. 49.2). Ideally, the volume fraction of precipitation would be measured as a function of time and temperature and fit to Eq 6.1. The times in Table 6-2 can be fit to Eq 6.1 if it is modified for a constant volume fraction. Combining Eq 6.1 and Eq 6.2 at constant volume fraction yields:

$$\ln(t_f) = \frac{C_2}{n} \cdot \frac{1}{T} + C_f \quad (6.3)$$

The times in Table 6-2 can be fit to Eq 6.3 because complete grain boundary coverage, for example, occurs at a constant volume fraction at different temperatures if the grain size and the thickness of the precipitation layer at the boundaries are the same. Plots of $\log(\text{time})$ vs. reciprocal temperature for the various precipitation stages are given in Figure 6-2. Only two points are plotted for the time at which grain boundary precipitation starts. At the higher temperatures, grain boundary precipitation was seen to have already begun after 1 hr, which is the shortest aging time investigated thus far. Because precipitation on grain boundaries actually began at shorter times, these times were not plotted. The time at 649°C, however, was plotted because precipitation had only just started at a few sites on the grain boundaries in that sample.

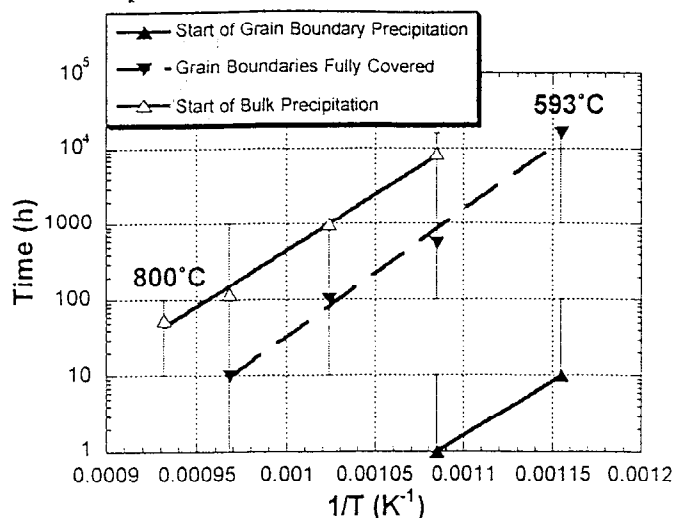


Figure 6-2. Time to Reach Various Stages of Precipitation in Aged Alloy 22 Plotted on a Log Scale as a Function of Reciprocal Temperature (See Eq 6.3)

If it can be assumed that the precipitation mechanism does not change, the lines in Figure 6-2 can be extrapolated to give the times that can be expected for the various stages of precipitation at lower temperatures. These data are very preliminary, however. The times were estimated from examination of micrographs from samples with widely spaced aging times. Extrapolation to lower temperatures is difficult because the precipitation rate is quite sensitive to temperature; small changes in slope make a very large change in the time obtained from extrapolation to lower temperatures. For this reason, no extrapolation is attempted at this time. In the future, the volume fraction of precipitation will be measured, and the time to give various amounts of precipitation will be taken from a plot of f versus t . This procedure will reduce the error associated with the times in Table 6-2 and Figure 6-2 and make possible a more meaningful extrapolation. Also, the data in Figure 6-2 represent the precipitation kinetics during an isothermal anneal. The repository temperature is not expected to remain constant. Instead, it will peak at some value less than 350°C and slowly decrease over time. A more quantitative model based on Eq 6.1 that can be integrated over a variable temperature profile will be developed to provide more accurate results. In addition, a theoretical model will be developed that will give more precision in extrapolation to lower temperatures. In the meantime, extrapolation of the preceding curves, although fraught with uncertainty, does not indicate that phase stability of Alloy 22 *base metal* will be a problem at less than about 300°C.

As a measure of the reasonableness of the data plotted in Figure 6-2, the activation energy can be calculated. The slopes of the lines in Figure 6-2 (after accounting for the $\log(e)$ factor) are equal to C_2/n in Eq 6.3. If these slopes are averaged and n is assumed to be equal to one, which is a reasonable value for n (Christian 1975, p. 542, Table IX), there is an activation energy of 290 kJ/mol (70 kcal/mol). This is fairly close to the value of 62 kcal/mol obtained by Hodge (1973, p. 378 ¶ 1) for precipitation in alloy C-276. This value is also fairly typical for diffusion of relevant elements in nickel (Ni) (Brandes and Brook 1992, Ch. 13, p. 13-23). For example, the activation energy for diffusion of chromium in Ni is 272.6 kJ/mol, that of iron is 253-270 kJ/mol, and that of tungsten in Ni is 300-308 kJ/mol.

6.3 EXTRAPOLATION OF EMPIRICAL INTERMETALLIC AND CARBIDE PRECIPITATION KINETICS DATA (TBD)

The semilogarithmic plot in Figure 6-2 is difficult to extrapolate to lower temperatures (higher $1/T$) because the result of such an extrapolation is very sensitive to the slope of the line that is used. Because only a few samples were examined at each temperature, the error associated with the points plotted in Figure 6-2 is relatively high, making an extrapolation somewhat meaningless. To reduce the error, the volume fraction of precipitates will be measured as a function of aging time and temperature. The time to give fixed volume fraction will be more accurately determined from a plot of volume fraction as a function of time for each temperature. In addition, more samples will be aged near the times of interest determined from the volume fraction versus time plots and the TTT diagram of Figure 6-1. The decrease in the time interval at which samples are examined and the quantification of volume fraction should reduce the error to the point that extrapolation of data, such as that presented in Figure 6-2, is more meaningful. Also, measurement of volume fraction as a function of time allows integration over a variable temperature profile.

6.4 EFFECT OF INTERMETALLIC AND CARBIDE PRECIPITATION ON MECHANICAL PROPERTIES OF ALLOY 22 BASE METAL (TBD)

Intermetallic and carbide phases, especially those forming at grain boundaries, are known to embrittle Ni-Cr-Mo alloys such as Alloy 22 (Matthews 1976, p. 219). The mechanical properties such as strength and elongation measured in a uniaxial tension test and toughness will be measured as a function of volume fraction of precipitates forming. These data will allow the determination of the effect of any precipitation that is predicted to form on mechanical properties.

6.5 KINETICS OF INTERMETALLIC PRECIPITATION IN ALLOY 22 WELD HAZ (TBD)

The HAZ of a weld is the region of the base metal near the weld that is subjected to a significant thermal pulse during the welding process. Intermetallic precipitation kinetics in the HAZ will be similar to that in the base metal, discussed in Section 6.2, but actual rates of precipitation may be different. The high temperatures, approaching the melting point, seen in the HAZ of welds might trigger nucleation of intermetallic and/or carbide precipitates. If nuclei are already present, precipitation will proceed much faster than in the base metal where they are not present. Thus, weld samples will be aged, and the volume fraction of precipitates in the HAZ will be measured as a function of aging time and temperature. These data will be used to obtain kinetic information empirically with an equation (such as Eq 6.1) and theoretically (Section 6.9).

Very few precipitates have been observed in the HAZ of weld samples thus far (Figures 4-64 and 4-68), but only two weld samples have been examined: one in the as-welded condition and one after aging at 427°C. These precipitates may simply be carbides that were present in the mill-annealed (i.e. as-received) condition. Carbides are known to be present in Ni-base alloys similar to Alloy 22, but they are usually within the grains and are generally called primary carbides to distinguish them from other secondary phases that form, often on grain boundaries, after an aging treatment (Tawancy et al. 1983, p. 40, ¶ 3). The particle in Figure 4-68 was not identified, but could be one of these primary carbides.

6.6 STABILITY OF INTERMETALLIC AND CARBIDE PRECIPITATES IN ALLOY 22 WELDS (TBD)

Welding causes melting of the alloy and the development of an as-cast structure upon cooling. The dendritic structure typical of welds can be seen in Figures 4-61 through 4-66. Because Mo and Cr tend to segregate out of the solid as the weld metal solidifies, the interdendritic regions tend to be rich in these elements (Cieslak et al. 1986, p. 2039, Figure 7), and intermetallic particles form there. Intermetallic particles can be seen in Figure 4-63. Primarily P phase is seen in the as-welded condition of Alloy 22 welds, but σ and μ phase are also seen (Cieslak et al. 1986, p. 2041, ¶ 2). Only one particle was seen in TEM in an Alloy 22 weld (Figures 4-68 through 4-70); this particle could be indexed as either P or σ phase.

Because precipitates are present in Alloy 22 welds from the beginning, kinetics of precipitation is not an issue as it is in the base metal and HAZ. Instead, it must be verified that the weld's mechanical and corrosion properties are not degraded by this precipitation. Whether these precipitates are stable and grow or unstable and dissolve with aging at repository-relevant temperatures must also be determined. Weld samples will be aged and characterized microstructurally (see Section 4.1.8). In addition, the mechanical and corrosion properties will be tested as a function of aging time and temperature. The effect of aging on weld properties will be used to infer the stability of the precipitates present in the as-welded condition. The results of the theoretical calculation of the Alloy 22 phase diagram (Section 6.8) will also indicate stability of the precipitates at repository temperatures.

6.7 KINETICS OF LRO REACTIONS IN ALLOY 22 (TBD)

The kinetics of LRO will be treated in a manner similar to that discussed for intermetallic and carbide precipitation in Sections 6.2 and 6.3. The volume fraction of ordered domains will be measured as a function of time and temperature, and the results will be used to generate plots such as those in Figures 6-1 and 6-2 and as input to the modeling effort discussed in Sections 6.8 and 6.9. Thus far, LRO has been observed in three samples. A very fine dispersion of ordered domains was seen after aging for 40,000 hr at 427°C in Alloy 22 base metal (Figures 4-75 through 4-77) and in a weld (Figures 4-78 through 4-83). The ordering in these cases is so fine that it is difficult to measure the volume fraction of the ordered domains. LRO was also observed in Alloy 22 base metal aged at 593°C for 16,000 hr (Figures 4-72 through 4-74). The volume fraction of ordered domains has not been measured in this sample.

6.8 THEORETICAL CALCULATION OF ALLOY PHASE DIAGRAM AT REPOSITORY-RELEVANT TEMPERATURES (TBD)

The work discussed in Sections 6.8 through 6.11 was performed in collaboration with Dr. Larry Kaufman (MIT; consultant at LLNL). A complete description of THERMOCALC and DICTRA is contained in *CALPHAD, Calculation of Phase Diagrams: A Comprehensive Guide* (Saunders and Miodownik 1998,). The electronic-structure approach mentioned in Sections 6.8 and 6.10 is fully described in *The LMTO Method: Muffin-Tin Orbitals and Electronic Structure* (Skriver 1984).

The main thrust of this study is to provide theoretical support for predicting properties of alloys selected for radioactive-waste containers with an expected operational lifetime of more than 10,000 yr at temperatures as great as 400°C (the heating is caused by radioactive decay of the stored waste). One of the current candidate materials is the Ni-based Alloy 22. The composition

of this alloy suggests that its matrix will consist of a face-centered cubic (fcc) phase in which the ordered Ni_2Cr phase (of Pt_2Mo type) is precipitated. Because the precipitation of this alloy occurs at relatively low temperature, and therefore occurs very slowly, the range of stability of this phase in the Ni–Cr and Ni–Cr–Mo systems is difficult to determine experimentally.

To better describe the stability of this ordered phase in the Ni–Cr binary alloy, the Ni–Cr–Mo ternary alloy, and the higher-order multicomponent Alloy 22, a CALPHAD analysis of these systems is being performed using THERMOCALC (commercial software, version M, 1998) and databases (in particular, the commercially available SSOL97 database, 1999) in combination with *ab initio* quantum mechanical-based calculations within the linear muffin-tin orbital (LMTO) methodology. THERMOCALC, together with the database SSOL97, which has been selected for studying Alloy 22, has been validated for the binary Ni–Cr, Ni–Mo, and Cr–Mo alloys. The phase diagram of the ternary Ni–Cr–Mo alloy has also been validated with available experimental and interpolated data to temperatures as low as 850°C. The ordered phase of Pt_2Mo type and the μ phase have not been yet incorporated in the database.

Additional calculations, with these restrictions in mind, have been performed to determine, at temperatures as low as 600°C, phase stability for the ternary Ni–Cr–Mo alloy and to predict the corresponding phase diagrams. From preliminary work, results of the calculations on phase fraction versus temperature indicate that at repository-relevant temperatures, the commercial Alloy 22 should be, *at equilibrium*, in a two-phase region of stability, with an equilibrium between the fcc phase and the P phase and respective phase fraction of approximately 0.6 and 0.4, with minor fraction of carbides and silicides (less than 0.05). After further determination of the Gibbs energy for the ordered Ni_2Cr phase and the complex μ phase, more definitive conclusions can be drawn on the equilibrium thermodynamics of Alloy 22.

6.9 THEORETICAL CALCULATION OF ALLOY 22 TTT DIAGRAM AND EXTRAPOLATION TO LOWER TEMPERATURES (TBD)

Once the thermodynamics of the ordered phase are established in the case of Ni–Cr and Ni–Cr–Mo alloys, the DICTRA (commercially available Diffusion Control TRANSformation software, version 18, 1998) program, combined with THERMOCALC and the SSOL97 and MOB (commercially available Mobility database, 1998) databases, will be used to calculate TTT diagrams for the growth of the most important phases of Alloy 22 (i.e., the ordered $\text{Ni}_2(\text{Cr},\text{Mo})$ and complex P and μ phases for times as long as 10,000 yr). These curves will be based on diffusional growth of the ordered phase from a fixed number of nuclei; the number of nucleation sites will be estimated from experimental observations for accurate predictions. Short-time experiments performed as a function of temperature will allow careful validation of the databases, and extrapolation to long time (as much as 10,000 yr) will be performed with the most advanced codes available.

6.10 KINETICS OF LRO REACTIONS IN ALLOY 22 (TBD)

Based on the energetics predicted from quantum mechanical-based LMTO calculations, further confirmed by the data contained in the revised version of SSOL97 (see Section 6.9), Monte Carlo simulations will be performed to study kinetics of transformation and microstructure evolution of the ordered phase with time and at various temperatures.

6.11 SOLIDIFICATION PATH OF THE ALLOY 22 (TBD)

From an analysis of the solidification by phase fraction of Alloy 22, which will be performed with THERMOCALC, it will be possible to predict the behavior of the alloy the during the welding process. Simulations of solidification will be conducted over a range of compositions around the nominal alloy composition by developing isopleths (i.e., sections of multicomponent phase diagram) for each of the four major alloying ingredients.

7. CONCLUSIONS

After aging for 16,000 hr at 593°C, P phase was found at Alloy 22 grain boundaries. At higher temperatures (as much as 760°C for the same aging time), both μ and P phase formed on grain boundaries and within the grains. Grain boundary carbides also form at 593°C and higher, but the amount of carbide is small compared to the μ and P phases. A small amount of sigma phase forms in Alloy 22 after 16,000 hr at 704 and 760°C. LRO was seen after aging for 16,000 hr at 593°C and for 40,000 hr at 427°C, but ordering most likely begins at shorter times. More work must be done in phase identification. Samples aged at times less than 16,000 hr must be examined so that the phase evolution during aging can be determined. A procedure being developed for phase extraction and x-ray diffraction should make phase identification and quantification of the relative amounts of each phase easier.

The times at which various stages of intermetallic precipitation occur in Alloy 22 base metal displayed an exponential (Arrhenius-type) temperature dependence. The activation energy was determined to be 290 kJ/mol. A more quantitative model based on precipitate volume fraction measurements that can be integrated over a variable temperature profile must be developed before a reasonable prediction of the phase stability of Alloy 22 base metal under repository conditions can be made. In addition, the effect of intermetallic and carbide precipitation on Alloy 22 properties must be determined. Precipitation kinetics in weld heat-affected zones, as well as in the base metal, must be studied because the thermal pulse given the HAZ during the welding process may alter nucleation of intermetallics and therefore the precipitation kinetics.

Intermetallic and carbide precipitates form in Alloy 22 welds during the welding process. It will be verified that these phases do not have a detrimental effect on the relevant weld properties. The effect of aging on the precipitate volume fraction and average size and on weld properties must also be determined.

Long-range order has been observed in a sample aged at 593°C for 16,000 hr and in samples aged at 427°C for 40,000 hr. These observations are not sufficient to evaluate the possibility of LRO occurring in Alloy 22 under repository conditions. Alloy 22 samples must be aged for various times at temperatures less than approximately 600°C. The volume fraction of ordered domains in these aged samples will be measured and fit to nucleation and growth theory.

The experimental analyses previously discussed assume that the kinetics of formation of the μ and P phases are similar and that the amount of carbide and σ phase present is too small to affect the measured rates of precipitation. This assumption will be verified through the direct measurement of the amounts of each phase forming as a function of aging time and temperature. Should this assumption prove to be invalid, the analyses for intermetallic and carbide precipitation will be modified to account for the different phases precipitating. Minor compositional changes in Alloy 22 are also assumed to have little or no effect on the rate of precipitation. Heat-to-heat variability studies will have to be done to verify this assumption.

The experimental analyses previously discussed also assume that the precipitation mechanism operating at the high temperatures studied also operates at the lower temperatures expected in the potential repository and that the phases seen at the higher temperatures are stable at the lower temperatures. Theoretical modeling, currently in the planning stages, will be done to verify these assumptions and to aid the extrapolation of experimental data to the long times associated with the WP container lifetime.

CHECK COPY

8. REFERENCES

- ASTM. 1994. *Standard Specification for Low-Carbon Nickel-Molybdenum-Chromium, Low-Carbon Nickel-Chromium-Molybdenum-Tungsten Alloy Plate, Sheet, and Strip*. ASTM B 575-94. Philadelphia, Pennsylvania: American Society for Testing and Materials. ACC/TIC: 237683.
- Brandes, E.A., and Brook, G.B., eds., 1992. *Smithells Metals Reference Book*. (Seventh edition) Oxford, United Kingdom: Butterworth-Heinemann.
- Christian, J.W. 1975. "Equilibrium and General Kinetic Theory." *The Theory of Transformations in Metals and Alloys*. (Part I edition) New York, New York: Pergamon Press.
- Cieslak, M.J., Headley, T.J., and Romig, A.D., Jr. 1986. "The welding metallurgy of Hastelloy Alloy C-4, Alloy C-22, and Alloy C-276." *Metall. Mater. Trans. A* 17(11):2035-2047. ACC/TIC: 233952.
- CRWMS M&O. 1998. *Classification of the Preliminary MGDS Repository Design*. B00000000-01717-0200-00134 REV. 01. Las Vegas, Nevada: Civilian Radioactive Waste Management System, Management and Operating Contractor: TRW Environmental Safety Systems, Inc. ACC/TIC: MOL.19981103.0546.
- CRWMS M&O. 1999a. *Model Development for Juvenile Failures in Waste Packages*. Las Vegas, Nevada: Civilian Radioactive Waste Management System Management and Operating Contractor: TRW Environmental Safety Systems, Inc.
- CRWMS M&O. 1999b. *Uncanistered Spent Nuclear Fuel Disposal Container System Description Document*. B00000000-01717-1705-00004 Rev. 01. Las Vegas, Nevada: Civilian Radioactive Waste Management System Management and Operating Contractor: TRW Environmental Safety Systems, Inc.
- DOE. 1998. *Quality Assurance Requirements and Description*. DOE/RW-033P, Rev. 8. Washington, District of Columbia: U.S. Department of Energy. ACC/TIC: MOL.19980601.0022.
- Hodge, F.G. 1973. "Effect of aging on the anodic behavior of Ni-Cr-Mo alloys." *Corrosion* 375-383. ACC/TIC: 240167.
- Leonard, R.B. 1969. "Thermal stability of Hastelloy alloy C-276." *Corrosion* 222-228. ACC/TIC: 240456.
- Matthews, S.J. 1976. "Thermal Stability of Solid Solution Strengthened High-Performance Alloys." Kear, B.H., Muzyka, D.R., Tien, J.K., and Wlodek, S.T., eds. *Superalloys: Metallurgy and Manufacture*. pp. 215-227. Baton Rouge, Louisiana: Claitor's Publishing Division.
- Raghavan, M., Berkowitz, B.J., and Scanlon, J.C. 1982. "Electron microscopic analysis of heterogeneous precipitates in Hastelloy C-276." *Metall. Mater. Trans. A* 13(6):979-984. ACC/TIC: 240058.
- Saunders, N., and Miodownik, A.P. 1998. *CALPHAD, Calculation of Phase Diagrams: A Comprehensive Guide*. New York, New York: Pergamon Press. (ISBN 0-08-0421296)

CHECK COPY

Skriver, H.L. 1984. *The LMTO Method: Muffin-Tin Orbitals and Electronic Structure*. Springer Series in Solid State Sciences 42. New York, New York: Springer-Verlag.

Tawancy, H.M., Herchenroeder, R.B., and Asphahani, A.I. 1983. "High-performance Ni-Cr-Mo-W alloys." *J. Metals* 35(6):37-43.

CHECK COPY

9. ATTACHMENTS

There are no attachments for this report.

